UNIVERSIDADE FEDERAL DE SANTA CATARINA
CENTRO TECNOLÓGICO DE JOINVILLE
PROGRAMA DE PÓS-GRADUAÇÃO EM ENGENHARIA E CIÊNCIAS MECÂNICAS

FREDI CENCI

EXPERIMENTS ON VORTEX-INDUCED VIBRATIONS OF A LONG HORIZONTAL CYLINDER UNDER UNIFORM CURRENT PROFILES

JOINVILLE
2019

FREDI CENCI

EXPERIMENTOS DE VIBRAÇÕES INDUZIDAS POR VÓRTICES EM UM CILINDRO HORIZONTAL LONGO, SOB PERFIS DE CORRENTEZA UNIFORME

Dissertação submetida ao Programa de Pós-Graduação em Engenharia e Ciências Mecânicas da Universidade Federal de Santa Catarina para a obtenção do título de mestre em Engenharia e Ciências Mecânicas.
Orientador: Prof. Dr. André Luís Condino Fujarra.

Joinville
2019

FREDI CENCI

EXPERIMENTS ON VORTEX-INDUCED VIBRATIONS OF A LONG HORIZONTAL CYLINDER UNDER UNIFORM CURRENT PROFILES

Master's Dissertation submitted to the master's program in Engineering and Mechanical Sciences of the Federal University of Santa Catarina for obtaining the master's degree in Engineering and Mechanical Sciences.
Advisor: Prof. Dr. André Luís Condino Fujarra.

Joinville
2019

Ficha de identificação da obra elaborada pelo autor,
através do Programa de Geração Automática da Biblioteca Universitária da UFSC.

Cenci, Fredi
Experiments on Vortex-induced Vibrations of a Long Horizontal Cylinder Under Uniform Current Profiles / Fredi Cenci ; orientador, André Luís Condino Fujarra, 2019.
89 p.

Dissertação (mestrado) - Universidade Federal de Santa Catarina, Campus Joinville, Programa de Pós-Graduação em Engenharia e Ciências Mecânicas, Joinville, 2019.

Inclui referências.

1. Engenharia e Ciências Mecânicas. 2. Flexible cylinders. 3. Vortex-induced vibration. 4. Risers. 5. Experiments. I. Condino Fujarra, André Luís . II. Universidade Federal de Santa Catarina. Programa de Pós Graduação em Engenharia e Ciências Mecânicas. III. Título.

FREDI CENCI

EXPERIMENTS ON VORTEX-INDUCED VIBRATIONS OF A LONG HORIZONTAL CYLINDER UNDER UNIFORM CURRENT PROFILES

O presente trabalho em nível de mestrado foi avaliado e aprovado pela banca examinadora composta pelos seguintes membros:

Prof. Alexandre Mikowski, Dr.
Universidade Federal de Santa Catarina

Rodolfo Trentin Gonçalves, Dr. - Videoconferência
Universidade de Tóquio

Prof. Thiago Antonio Fiorentin, Dr.
Universidade Federal de Santa Catarina

Certificamos que esta é a **versão original e final** do trabalho de conclusão que foi julgado adequado para a obtenção do título de mestre em Engenharia e Ciências Mecânicas.

Prof. Dr. Régis Kovacs Scalice
Coordenador do Programa

Prof. Dr. André Luís Condino Fujarra
Orientador

Joinville, 08 de Agosto de 2019

Dedico este trabalho primeiramente a Deus que me guiou durante esta caminhada. À minha mãe Salete Rogeri Borsatto Cenci, *In Memorian*, e meu pai Erineu Roberto Cenci. Ao meu irmão Francis e minha madrinha Luciana que me apoiaram e estiveram do meu lado nesta jornada. À minha namorada Rayza Yasmin de Oliveira Vicente pela compreensão, amor e solidariedade inefável. Aos meus amigos e familiares, pelo incentivo e apoio constantes.

AGRADECIMENTOS

Agradeço ao meu orientador André Luís Condino Fujarra pelas horas dedicadas na minha orientação e a disposição na composição deste trabalho. Agradeço a Petrobras e a Agência Nacional do Petróleo (ANP) por fomentarem a pesquisa científica que deu subsídio para esta dissertação.

RESUMO

A Vibração Induzida por Vórtices (VIV) é um fenômeno de interação fluido-estrutura que é extremamente importante para a indústria do petróleo. Os *risers* são frequentemente excitados por este fenômeno resultando em oscilações que reduzem a vida útil dos equipamentos. A complexidade deste fenômeno hidro-elástico não-linear ainda não é completamente entendida pela comunidade científica e investigações em modelos flexíveis dão suporte para a descoberta de peculiaridades do VIV. Este trabalho apresenta resultados experimentais de um cilindro flexível longo e horizontal. A resposta dinâmica do modelo é apresentada, relacionada com a amplitude, a frequência, o ângulo de fase e as trajetórias dos movimentos. O cilindro é considerado longo, com razão de aspecto igual a 148, e razão de massa igual a $3,9$. Os experimentos foram conduzidos em um tanque de reboque e o cilindro flexível foi excitado por perfis uniformes de escoamento. Vinte velocidades reduzidas foram testadas, em uma faixa de $1,75 < Vr < 15,79$, correspondendo a números de Reynolds de 1.000 até 10.000. As medições foram realizadas utilizando um sistema de rastreamento óptico subaquático, onde movimentos nas três direções foram monitorados a partir de 18 alvos distribuídos ao longo de aproximadamente metade do comprimento do modelo. Amplitudes transversais r.m.s de até $0,77$ diâmetros e longitudinais de até $0,23$ diâmetros foram observadas, e a dinâmica do modelo mostrou comportamento multimodal. A faixa de sincronização transversal influenciou muito os modos longitudinais excitados. Os resultados alcançados se mostram extremamente relevantes para futuras validações de modelos analíticos e códigos numéricos.

Palavras-chave: Cilindros flexíveis. vibrações induzidas por vórtices. experimentos. projeção modal. transformada de Hilbert-Huang. ângulo de fase.

RESUMO EXPANDIDO

Introdução

A Interação Fluido-Estrutura (FSI), do acrônimo *Fluid-Structure Interaction*, é um tópico relevante em muitos setores da engenharia. Na indústria do petróleo não é diferente. As estruturas como os *risers* e linhas de amarração, sob a ação de correntes marítimas, iniciam vibrações indesejadas conhecidas como Vibrações Induzidas por Vórtices (VIV). Assim, a exploração petrolífera em profundidades cada vez maiores estabelecem um desafio tecnológico para o setor.

O VIV tem sido investigado também pela sua complexidade e características do escoamento. Ele é um fenômeno hidro-elástico e não linear que é de difícil entendimento. Ao longo dos anos, muitos trabalhos simplificaram o problema, como os estudos em cilindros rígidos, forçados, com um/dois graus de liberdade (DOF), do acrônimo *Degree of Freedom*, montados em base elástica. Esses trabalhos mostraram os padrões de emissão de vórtices, coeficientes de arrasto e sustentação, flutuação das forças, frequência e amplitude, bem como ramos de resposta do VIV, trajetórias de movimento e a influência do fator de massa-amortecimento. Algumas revisões importantes são encontradas nos trabalhos de Bearman (1984a), Williamson and Govardhan (2004), Sarpkaya (2004), Bearman (2011), Jauvtis and Williamson (2003) e Jauvtis e Williamson (2004).

No setor *offshore*, as estruturas esbeltas, como cilindros flexiveis, com baixa razão de massa, são mais próximas de estruturas reais como os *risers*. Os cilindros flexíveis apresentam um escoamento complexo com diversos modos de vibrar. Devido à complexidade, a relação entre os cilindros rígidos e flexíveis não é entendida completamente. Vários trabalhos relacionados com cilindros flexíveis foram publicados, como Chaplin et al. (2005), Lie e Kaasen (2006), Huera-Huarte e Bearman (2009a, 2009b), Rateiro et al. (2012), Pereira et al. (2013), Morooka e Tsukada (2013), Malta (2015), Franzini et al. (2015, 2016a, 2016b, 2018),

Este trabalho conduz experimentos para investigar o VIV em um cilindro flexível. O experimento foi feito no tanque de reboque no Instituto de Pesquisas Tecnológicas (IPT) do estado de São Paulo com parceria da Petrobras. O modelo foi rebocado em uma faixa de velocidades, medindo diretamente o deslocamento de 18 localizações ao longo do modelo. As análises buscam características interessantes do VIV, como a resposta multimodal, trocas entre modos naturais, acoplamento entre os movimentos e os ângulos de fase. Desta maneira, o resultado e caracterização deste trabalho é relevante não somente para o entendimento do fenômeno, mas também para futura validação de modelos numéricos e teóricos para previsão do VIV.

Objetivos

De acordo com a complexidade do fenômeno apresentado, o objetivo geral desta dissertação é a investigação da dinâmica de um cilindro flexível longo sob a ação das vibrações induzidas por vórtices.

Esta investigação é experimental, caracterizando o comportamento multimodal de um cilindro flexível usando técnicas sofisticadas de identificação de frequências e amplitudes de resposta.

A contribuição desta dissertação são os resultados experimentais do VIV em cilindro flexíveis usando um método de medição direta, difícil de encontrar na literatura. Além disso, o significante número de velocidades ensaiadas e todas as análises feitas dão um conjunto único de resultados em um mesmo trabalho.

Metodologia

O tanque de reboque utilizado possui $280\ m$ de comprimento, $6,6\ m$ de largura e $4\ m$ de profundidade. A faixa do número de Reynolds no ensaio foi de 1.000 até 10.000, em 20 velocidades de reboque. O cilindro flexível foi acoplado horizontalmente por duas rótulas. Em uma delas foi adicionada uma célula de carga unidirecional para a medição da tração inicial do sistema. Os alvos para medição dos deslocamentos foram distribuídos de 0 a 56% do comprimento do modelo, a partir de uma das extremidades. Estes alvos são rastreados por cinco câmeras subaquáticas que registram seus movimentos ao longo do experimento.

O cilindro flexível foi construído de uma mangueira de silicone de $21\ mm$ de diâmetro externo preenchida com microesferas de aço de $2,3\ mm$. A combinação destes materiais gerou um modelo com baixa rigidez flexional, mas com uma considerável rigidez axial. Neste modelo, as frequências e assim como os amortecimentos nos planos de oscilação vertical e horizontal ficaram próximas. Este modelo é semelhante aos utilizados nos estudos de Pereira et al. (2013b), Pereira et al. (2013a, 2016) e Franzini et al. (2016a, 2016b).

Os valores de amortecimento da estrutura foram obtidos com testes de decaimento no ar, para a obtenção da parcela estrutural, e na água, para o valor total. Em ambos decaimentos, a tração inicial na estrutura é a mesma aplicada nos experimentos de VIV.

Para a caracterização do cilindro flexível, o seguinte procedimento foi adotado. Primeiramente, o modelo é pesado fora da água, onde é também fixado no suporte com as células de carga e as rótulas. Depois, a tração é imposta, e a funcionalidade das células de carga são verificadas. Posteriormente, os alvos são dispostos ao longo do modelo e, então, o conjunto é imerso na água e a tração é novamente medida. Por fim, as câmeras subaquáticas são calibradas para rastrear os alvos.

Depois do procedimento de calibração, o modelo está pronto para os ensaios de

decaimentos e de VIV. Nos ensaios de VIV, o modelo é rebocado por 350 segundos.

Resultados e Discussões

A resposta dinâmica do cilindro flexível mostrou três faixas de sincronização. Na primeira faixa, a máxima amplitude na direção transversal ao escoamento foi de $A_z^{r.m..s} = 0,60D$ e na direção do escoamento de $A_x^{r.m..s} = 0,13D$. Na segunda faixa, $A_z^{r.m..s} = 0,77D$ e $A_x^{r.m..s} = 0,23D$. A terceira faixa foi visualizada apenas em duas velocidades, e não foi possível identificar o pico da sincronização. A razão entre as amplitudes no sentido transversal e longitudinal ao escoamento ficou entre 4 e 6, valores também publicados por Huera-Huarte e Bearman (2009a). A razão entre frequência de oscilação evidenciou também as faixas de sincronização. Destes valores, foram obtidos o número de Strouhal de $0,16$ para a direção transversal e $0,32$ para a direção do escoamento, valores também encontrados por Huera-Huarte e Bearman (2009a).

A projeção modal aplicada neste trabalho mostrou um resposta multimodal do cilindro flexível. A amplitude total geralmente é uma composição de alguns modos naturais sobrepostos, vibrando na frequência do modo dominante. Esta característica foi também encontrada por Chaplin et al. (2005b).

As análises de Hilbert-Huang mostraram resultados similares as análises de Fourier. Em regiões com contribuição unimodal superior, as faixas de oscilação da frequência no tempo foram estreitas. Nestas condições, as frequências obtidas pela análise de Hilbert-Huang e Fourier coincidem. Contudo, em regiões onde existe contribuição de mais modos naturais, uma banda larga de frequências é observada.

As trajetórias mostraram sincronização entre os movimentos na direção longitudinal e transversal ao escoamento. O ângulo de fase relativa mostrou diferentes valores que impactam nas trajetórias de movimento do cilindro flexível. Alguns casos apresentaram dois ângulos preferenciais, geralmente no pico da faixa de sincronização.

Considerações Finais

Os resultados encontrados mostraram valores de oscilação menores que cilindros rígidos e logos, se aproximando de publicações relativas à estruturas flexíveis. A resposta dinâmica é mais próxima a de cabos tensionados do que de cilindros rígidos montados em base elástica devido à sucessiva sincronização de modos naturais e a ausência dos ramos do VIV encontrados na dinâmica dos cilindros rígidos. Ainda, esta dissertação exibe uma série de análises interessantes em um único experimento com medição direta dos movimentos, contribuindo para a literatura relativa ao VIV.

Trabalhos futuros aumentando a tração inicial e variando a massa devem trazer um entendimento ainda melhor do fenômeno. Além disso, a mecânica dos materiais envolvidas com esta variação de tração também podem ser avaliadas, uma vez que o material utilizado pode não trabalhar no regime elástico com a variação da tração.

ABSTRACT

The Vortex-induced Vibrations (VIV) is a phenomenon resulting from the fluid-structure interaction which is extremely important in the oil industry. The risers are frequently excited by this phenomenon resulting in oscillations which reduce the equipment lifetime. The complexity of this non-linear and hydro-elastic phenomenon is still not completely understood by the scientific community and investigations on flexible models support the peculiarities unveil of the VIV. This work presents experimental results of a horizontal long flexible cylinder. The model dynamic response is presented, connected to the amplitude, the frequency, the phase angle, and the trajectories of the movements. The cylinder is considered long, with aspect ratio equal to 148, and mass ratio equal to 3.9. The experiment was carried out in a towing tank, and the flexible cylinder was excited by uniform flow profiles. Twenty reduced velocities were tested, in a range of $1.75 < Vr < 15.79$, corresponding to Reynolds numbers from $1,000$ up to $10,000$. The measurements were performed using a submerged optical motion capture system, where displacements in the three directions were monitored from 18 targets distributed along half of the model's length. Cross-flow r.m.s amplitude responses up to 0.77 diameters and in-line up to 0.23 diameters were observed, and the model dynamics showed a multi-modal response behavior. The cross-flow lock-in highly influenced the in-line excitation modes. The results achieved showed to be extremely relevant for further validation of analytical models and numerical codes.

Keywords: Flexible cylinders. vortex-induced vibration. experiments. modal projection. Hilbert-Huang transform. phase angle

LIST OF FIGURES

LIST OF TABLES

LIST OF ABBREVIATIONS

VIV	Vortex-induced Vibrations
r.m.s	root mean square
HHT	Hilbert-Huang Transform
IMF	Intrinsic Mode Functions
EMD	Empirical Mode Decomposition
PDF	Probability Density Function
FSI	Fluid-structure Interaction
FIV	Flow-induced Vibration

LIST OF SYMBOLS

St	Strouhal number
Vr	Reduced velocity
s_j	Curve-linear position of the model
f_{ni}	Natural frequency of mode i
$\mathcal{M}_i$	Eigenvector of mode i
L	Total elongated length
U	Free-stream velocity
D	External diameter of the flexible cylinder
Am_i	Modal amplitude of mode i
$\psi_{z,x}$	Cyclic relative phase angle
$\theta_{z,x}$	Relative phase angle
μ	Mean value
σ	Standard deviation
D_i	Internal diameter
L_i	Initial length
L_f	Final length
m	Total structural mass
w_s	Wet weight
m^*	Mass ratio
L/D	Aspect ratio
EA	Axial stiffness
EI	Bending stiffness
T	Axial initial tension
ζ_{t2}	Total damping of $\mathcal{M}_2$

ζ_{s2}	Structural damping of $\mathcal{M}_2$
ζ_{s4}	Structural damping of $\mathcal{M}_4$
f_{st}	Vortex shedding frequency
f_{vs}	Vortex emission frequency in movement
S_G	Skop-Griffin parameter
$A^{r.m.s.}$	r.m.s amplitude response
A^{max}	Average of 10% of the highest amplitude responses

CONTENTS

1 INTRODUCTION

In this chapter, the motivation and objectives of the present work are given. The contextualization presents the fluid-structure problem and how this dissertation is related to the topic. On the other hand, the objectives inform the reader of the goals which this work seeks.

1.1 Contextualization

The Fluid-structure Interaction (FSI) is an interesting topic in many engineering sectors because it directly impacts in project designs, costs, and performance. Inside the FSI there are the Flow-induced Vibrations (FIV), which concerns to vibrations and movements caused by the flow incidence. These vibrations are significant for engineering subjects because, if out of control, may result in catastrophic events such as the well known Tacoma Narrows bridge.

In the oil industry, it is not different. There are structures such as risers, umbilicals, and mooring lines under ocean currents which urge unwanted vibrations known as Vortex-induced Vibrations (VIV). The quest for oil exploration at even greater depths establishes a technological challenge regarding the optimization of the structure's design. This technological challenge depends on the fundamental understanding of the fluid-structure interaction making scientific research an essential tool for this sector.

Investigation of VIV in risers can be performed experimentally or numerically. Although the increase of computational capacity during the last years, the solution to this problem by the finite volume method is still a challenge. Even if applied turbulence models, the problem requires a coupling between the structural flexibility and the fluid forces, resulting in simulations unrealistic for real engineering cases. A more simplified method, named Discrete Vortex Method (DVM), has been an alternative for preliminary analyses of offshore projects. However, it is not yet widespread and validated. In the experimental area, there are also barriers. The high rigidity of the lines of operation requires huge towing tanks, which do not exist in Brazil. Even the ones overseas provide limitations in the hydraulic diameter for the experiments in real scales. Scaled models are commonly used. However, the high aspect ratios (ratio between the length and external diameter) of structures require scale distortions.

Investigations into VIV have been a fluid-structure topic also because of its complexity and rich flow features. The complexity comes from the hydro-elastic

interaction and non-linear behavior which make the topic unlikely to be solved quickly. Therefore simplifications of the problem have been made along the years, such as studies of rigid cylinders, forced cylinders and one/two degree of freedom (DOF) rigid cylinders mounted in an elastic base. These studies have shown the flow field vortex emission, drag and lift coefficients, force fluctuations, frequency and amplitude response, branches of VIV, coupled trajectories and observations of mass and damping influence on the phenomenon. Some well known publications and reviews are found in Bearman (1984a), Bearman (2011), Jauvtis and Williamson (2003), Williamson and Govardhan (2004), Sarpkaya (2004) and Jauvtis and Williamson (2004).

Regarding the offshore scenario, flexible cylinders with low mass ratio may represent a real offshore structures, such as flexible risers. The flexible cylinders present a complex flow field, a high number of vibration modes, coexistence and jumps between modes. Due to the complexity of the problem, the correlation between the features of rigid and flexible cylinders are not completely understood by the scientific community. Several recent works have reported experimental investigations of VIV in flexible cylinders, such as Chaplin et al. (2005b), Lie and Kaasen (2006), Huera-Huarte and Bearman (2009a), Huera-Huarte and Bearman (2009b), Rateiro et al. (2012), Pereira et al. (2013a), Morooka and Tsukada (2013), Malta (2015), Franzini et al. (2015), Franzini et al. (2016a), Franzini et al. (2016b) and Franzini et al. (2018).

This work intends to conduct an experimental investigation on VIV of a flexible cylinder. The experiment was carried out in a towing tank at the Institute for Technological Research (IPT) in partnership with Petrobras. The model was towed in a wide range of reduced velocities, directly measuring the displacements of 18 locations of the model. The analysis seeks interesting features of VIV such multi-modal dynamic response, jumps between modes, the coupling between in-line and cross-flow movements, and relative phase angles. Therefore, all these characterization and results are relevant not only for the phenomena understanding but also for validation of mathematical and numerical models for VIV prediction.

1.2 Objectives

1.2.1 General Objective

According to the complexity of the problem presented, the general objective of this dissertation is the *dynamic response investigation of a long horizontal flexible cylinder under the vortex-induced vibration phenomenon due to uniform current profile.*

This investigation is experimentally carried out, evaluating the multi-modal behavior of the flexible cylinder using sophisticated analysis techniques of frequency and amplitude responses.

1.2.2 Specific Objectives

Based on the general objective, the following specific objectives must be achieved.

1. Assemble the flexible cylinder and proceed with the characterization of quantities such as axial rigidity, bending stiffness, natural frequencies, and damping.
2. Plan and execute the experiment in the towing tank;
3. Analyze the amplitude and frequency response of the model searching for the lock-in regions;
4. Compare the response on the frequency domain using the Fourier and the Hilbert Huang Transform;
5. Investigate the multi-modal behavior of the flexible cylinder, identifying the modes excited during the experiment;
6. Analyze the relative phase angle and search for relations between the angle and the trajectory of the flexible cylinder. Also, verify the relative phase angle of each mode excited during the experiment;
7. Verify the overall behavior of the flexible cylinder and compare with similar results in the literature.

1.3 Research Contributions

This dissertation provides VIV results of a flexible cylinder using direct amplitude measurements of many points of the model, which is difficult to find in the literature. Further, the significant number of reduced velocities and all the analysis performed (amplitude responses, frequency analysis using Fourier transform and HHT, modal projection, relative phase angle, and trajectories) gives a unique set of results in a single work. This complete work may be relevant for the validation of mathematical models and numerical codes for the academy and industry.

1.4 Dissertation Outline

The present dissertation is divided into five chapters, the introduction, literature review, methodology, results, and conclusions. Each chapter has the following content.

Chapter 1 is concerned about identifying the problem related to this dissertation and give insights about the VIV in the offshore industry. Also, expose the objectives and the main contribution which this dissertation will provide.

Chapter 2 review the works related to VIV in a rigid and flexible cylinder, identifying important parameters of VIV.

Chapter 3 explains the methodology used. This chapter is mainly divided into the experimental set up and procedures and methodology of analysis. The first explains

how the experiment was constructed and carried, giving insights about equipment and main procedures. The latest expose how the analysis was performed.

Chapter 4 shows the results of all the analysis performed. This chapter is the central chapter of this dissertation, where comparisons with other authors and discussions are made.

Chapter 5 is the conclusion. In this chapter, a summary of the findings and final remarks are made.

2 LITERATURE REVIEW

In this chapter details of flow around circular cylinders are given. Firstly, the Section 2.1 presents the literature in which this dissertation explored for publications of studies on VIV of flexible cylinders. Secondly, the Section 2.2 brings a brief review of the flow around a rigid stationary cylinder and VIV of rigid cylinders supported by an elastic support. Finally, the Section 2.3 compile the results found reviewing the most critical features on VIV of flexible cylinders.

It is important to highlight that, different from other literature reviews, the current work does not present it in chronological order. Essential pieces of information are given when necessary so that the reader understand the phenomenon and the features of VIV. This section intends to inform the reader in order to understand the following chapters rather than provide all insights about the subject.

2.1 Articles Research Method

This section is designed to present the method applied to map the principal scientific researches of VIV of flexible structures.

First, it is necessary to gather information on which this research will be achieved. For that, quick research showed that most of the publications related to VIV in flexible cylinders are found in ScienceDirect and Google Scholar database, the latest cover all Internet content. These two databases cover the main journals related to VIV, such as Journal of Sound and Vibration, Journal of Fluid and Structures, Applied Ocean Research, Ocean Engineering and many conference publications such as the International Conference on Ocean, Offshore and Arctic Engineering (OMAE), Conference on Bluff Body Wakes and Vortex-Induced Vibrations (BBVIV), International Society of Offshore and Polar Engineers (ISOPE), and the International Conference on Flow-Induced Vibration (FIV).

With the database defined, key-words are selected and combined for the search. These key-words are defined from past knowledge. Therefore the following key-words were used: *Vortex-induced Vibration*, *flexible cylinder*, *multi-mode* and *modal analysis*.

The results were filtered reading the abstract. In total, 31 articles were selected. Many of these publications will be used in this work in the bibliographic review and the result section.

2.2 Vortex-induced Vibrations of Circular Cylinders

The study of bluff bodies under uniform flow is a classic fluid mechanics problem. Many engineering applications are under these conditions and VIV is an object of study in various engineering subjects such as mechanical structures, mechanical of material, vibrations and fluid mechanics. The applications vary in many sectors, such as bridge construction, heat exchangers, energy transmission cables, structures related to oil and gas extraction, and ocean structures mooring systems (SARPKAYA, 2004).

Sarpkaya (2004) states that the state-of-the-art of VIV is interested in the study of rigid bodies, in the majority with a circular cross-section, with its degree of freedom reduced from six to one or two translational (in-line and cross-flow).

In order to deeply understand the VIV, firstly we look into the phenomenological aspects present in bluff bodies. Bearman (1984b) defines a bluff body as that which, when under fluid flow, result in that fluid separation on a substantial part of its surface. These bodies form and shed vortices with a similar wake independently the geometry.

The phenomenon of vortices formation and shedding occurs in the following manner. The fluid approaches the cylinder leading edge increasing the pressure and creating a stagnation point. The increasing pressure forces the fluid to move around the body, creating two boundary layers (one in each side). In high Reynolds numbers, the boundary layer separation occurs, and the fluid does not entirely contour the body surface. During this process, because the viscous layer of the shear layer moves slower than the upper layers and the high gradient pressure, the fluid swirls into the wake, generating and shedding vortices. While the vortices are generated and shed periodically, the pressure field on the surface is modified, which makes cylindric structures with DOF vibrate (BLEVINS, 1990). The Figure 1 shows the phenomenon described. The resulting forces of the flow around the cylinder is the drag coefficient, identified in the figure as C_D, and the lift coefficient, C_L. The sum of C_D and C_L is the vector C_F. Looking closer at the Figure 1, C_F changes its direction and magnitude as the time increases from (a) to (d). This happens because the vortex shedding and the modification of the pressure field. This force is cyclic and has the period of the vortex shedding.

Understanding the vortex shedding phenomenon, we infer that the flow regimes modifies the pressure fields, which are related to the resultant forces on the body. Thus, it is clear that the vortex street is depended on the Reynolds number (Re), defined by Equation (2.1) for circular cylinders.

$$Re = \frac{UD_e}{\nu} \tag{2.1}$$

Where $U\ (m/s)$ is the free-stream velocity, $D_e\ (m)$ is the cylinder external diameter and $\nu\ (m^2/s)$ the kinematic fluid viscosity. The Figure 2 shows the flow states of a circular

Figure 1 – Modification of the pressure field around a cylinder at $Re = 112000$ in approximately one third of a vortex cycle.

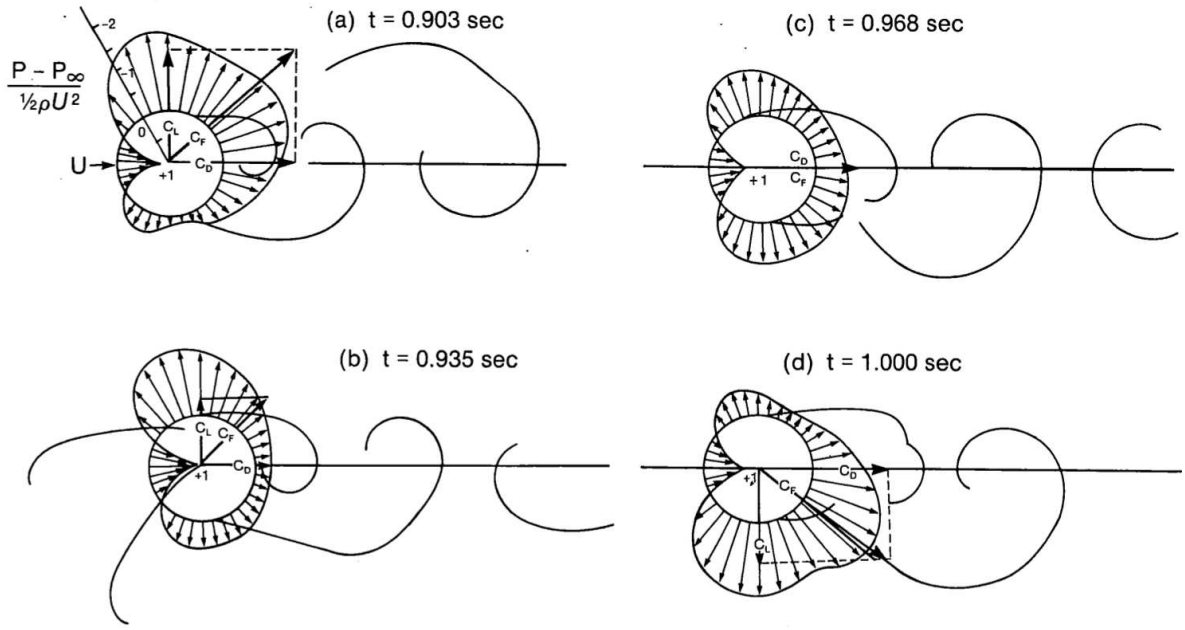

Source: Blevins (1990)

cylinder as function of the Reynolds number.

As shown in Figure 2, for $Re < 5$, the fluid go around the body without separation. With the increase of Re, a pair of symmetrical vortex develop on the wake. These vortices grow linearly with Re. Between $40 < Re < 150$, the periodic wake of laminar vortices are identified. Subsequently, the transition from laminar to turbulent wake takes place between $150 < Re < 300$. After the transition, over a large range of Re, the flow has a fully turbulent vortex street. This is called the sub-critical region, $300 < Re < 3\ 10^5$, where the separation occurs approximately 80 degrees from the leading edge. For values between $3 \times 10^5 < Re < 3.5 \times 10^6$ the boundary layer becomes turbulent, the separation angle changes to 140 degrees, and three-dimensionality strongly affects the vortex wake, becoming disorganized and narrower. Finally, for values greater than $Re = 3.5 \times 10^6$ the turbulent vortex wake is reestablished.

The alternation of vortex shedding is characterized by the Strouhal number (St), shown in Equation (2.2). The Stouhal number associate the vortex emission frequency $f_{st}\ (Hz)$ and the relation between the flow velocity $U\ (m/s)$ and the cylinder diameter $D_e\ (m)$. Naturally, the inverse relation of the frequency is the period $T\ (s)$ of one vortex cycle.

$$St = \frac{f_{st} D_e}{U} \tag{2.2}$$

Furthermore, replacing the Equation (2.1) into Equation (2.2), the Strouhal

Figure 2 – Flow regimes for a smooth circular cylinder.

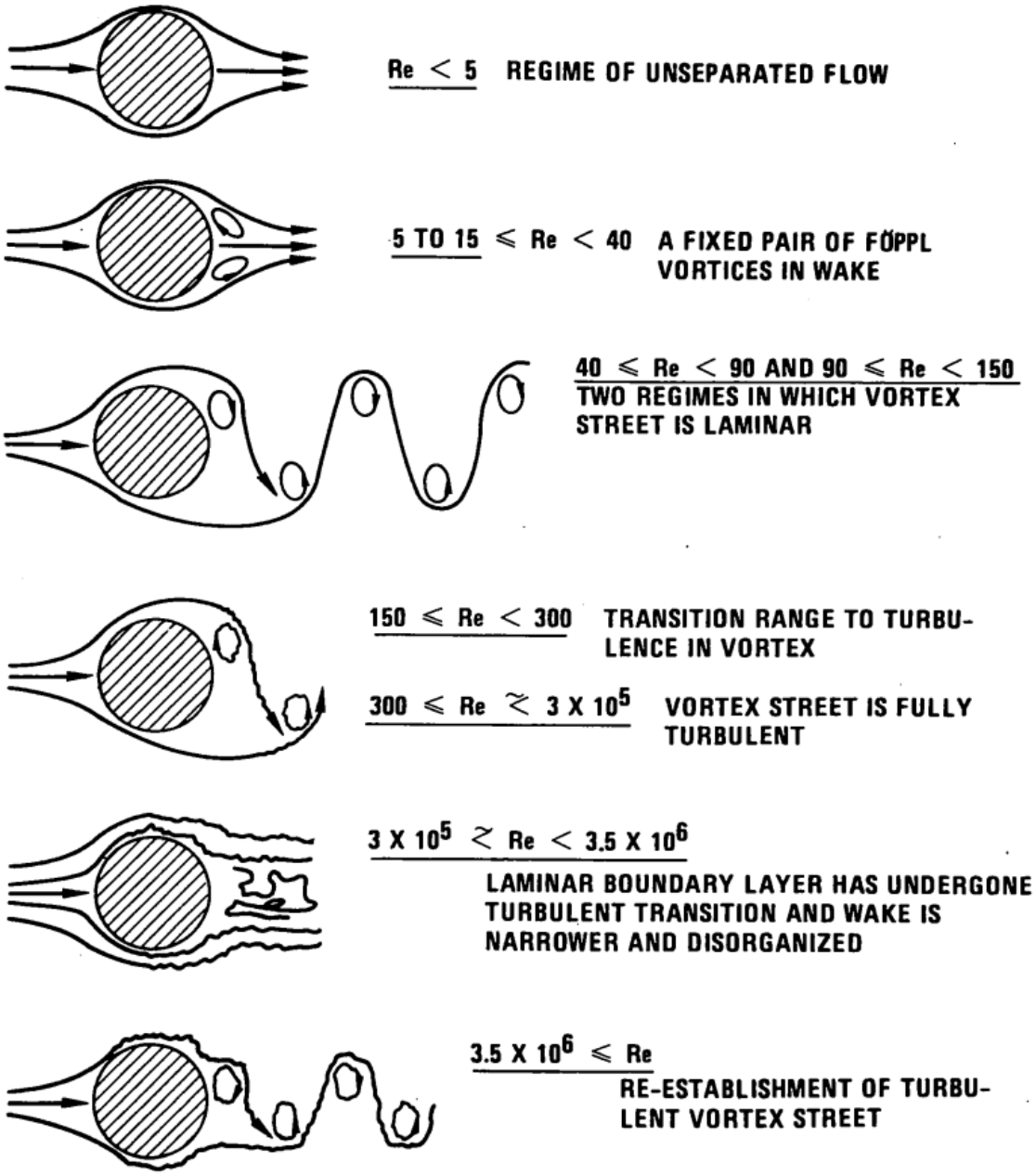

Source: Blevins (1990).

number can be written as function of the Reynolds number, as shown in Equation (2.3).

$$St = \frac{f_{st} Re\nu}{U^2} \tag{2.3}$$

During th sub-critic regime, a typical value of $St = 0.2$ is found, as shown in Figure 3.

Although a circular cylinder gives the present example, the vortex emission is found in any bluff body. The periodic vortex shedding results in a fluid force as shown in

Figure 3 – Strouhal number of a long rigid and fixed circular cylinder for a large range of Re.

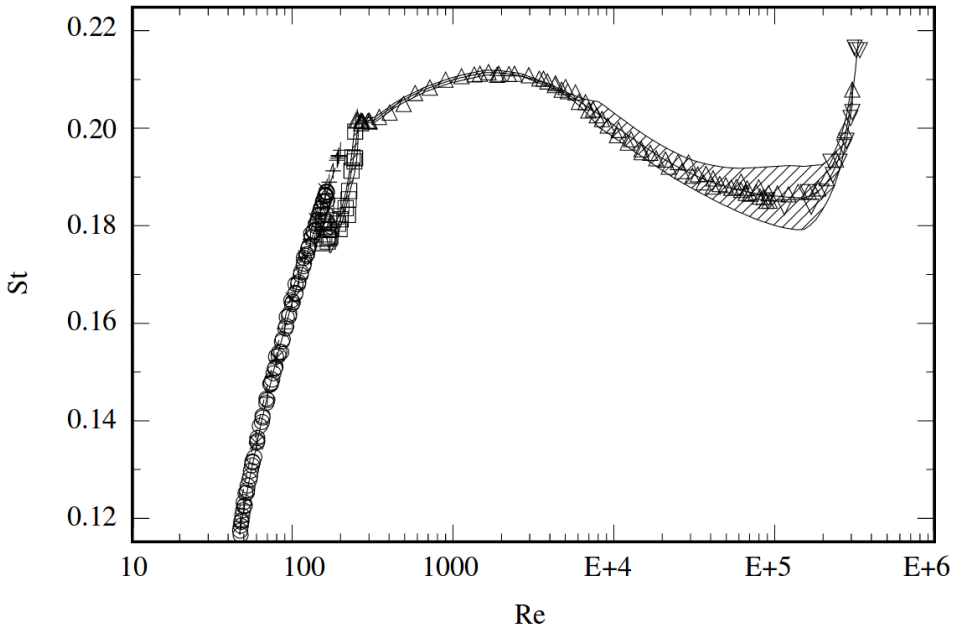

Source: Norberg (2003).

Figures 1 and 2. These forces are the source of VIV of cylinders, and several parameters are related to this phenomenon. For example, the mass ratio, which indicates the weight over the quantity of displaced mass; the damping coefficient that together with the mass ratio plays a vital role in the VIV response; the reduced velocity and the frequency ratio which points out the synchronization regions, and the non-dimensional amplitude which normalize the response amplitude. These main parameters are shown in Table 1. The variable m^* is the mass ratio, where $m\ (kg)$ is the mass, $\rho\ (kg/m^3)$ is the density of the water, $D_e\ (m)$ is the external diameter, $L\ (m)$ is the length of the cylinder. The variable ζ is the damping ratio, where $c\ (kg/s)$ is the structural damping, $2\sqrt{k(m+m_a)}$ is the critical damping in water where $k\ (N/m)$ is the stiffness and $m_a\ (kg)$ is the added mass. Vr is the reduced velocity, where $U\ (m/s)$ is the free-stream velocity, $f_N\ (Hz)$ is the natural frequency. A^* is the non-dimensional amplitude of response. where $A\ (m)$ is the amplitude of response. f^* is the frequency ratio, where f is the fluid excitation frequency. Finally, the Reynolds number (R_e) is defined in Equation (2.1).

The VIV in ocean structures is a resonant phenomenon which has characteristics of self-excitement and self-control. Considering a rigid cylinder mounted in an elastic support, Bearman (1984b) states that the vortex shedding induces oscillations mainly in the transverse to the flow incidence direction. According to Williamson and Govardhan (2004), in this type of systems, when the velocity increases and the vortex emission frequency get closer to the cylinder natural frequency the fluid

Table 1 – Main non-dimensional VIV parameters.

Parameter	Symbol	Equation
Mass Ratio	m^*	$\frac{m}{\pi\rho D_e^2 L/4}$
Damping Coefficient	ζ	$\frac{c}{2\sqrt{k(m+m_a)}}$
Reduced Velocity	V_r	$\frac{U}{f_N D_e}$
Non-dimensional Amplitude	A^*	$\frac{A}{D_e}$
Frequency Ratio	f^*	$\frac{f}{f_N}$
Reynolds Number	R_e	$\frac{UD_e}{\nu}$

Source: The Author (2019).

forces from the pressure field induces the movement of the body. It is important to note that the vortex shedding frequency (f_{st}) and the vortex emission frequency with the cylinder in movement (f_{vs}) are different in the excitation region (SARPKAYA, 2004). Because VIV has self-excitement behavior, the oscillations of the body modify the vortex shedding whereas f_{vs} and the body oscillation frequency are close although the velocity increases. This is known as the synchronization region or lock-in.

The amplitude responses in the lock-in may reach oscillations in the order of the cylinder's diameter. One of the parameters that affect the responses branches is the mass of the system. The Figure 4 shows the amplitude response as function of the reduced velocity.

It is possible to notice that for lower mass ratio values, three branches are present. Also, this system has higher amplitudes on the upper branch. On the other hand, higher values of mass arise only two branches, skipping the upper branch, presenting lower amplitude responses and reducing the lock-in range. The branches

Figure 4 – Transvers amplitude response (1 degree-of-freedom) as function of the reduced velocity for $m^*\zeta = 0.013$. Data from Feng (1968) for $m^* = 248$.

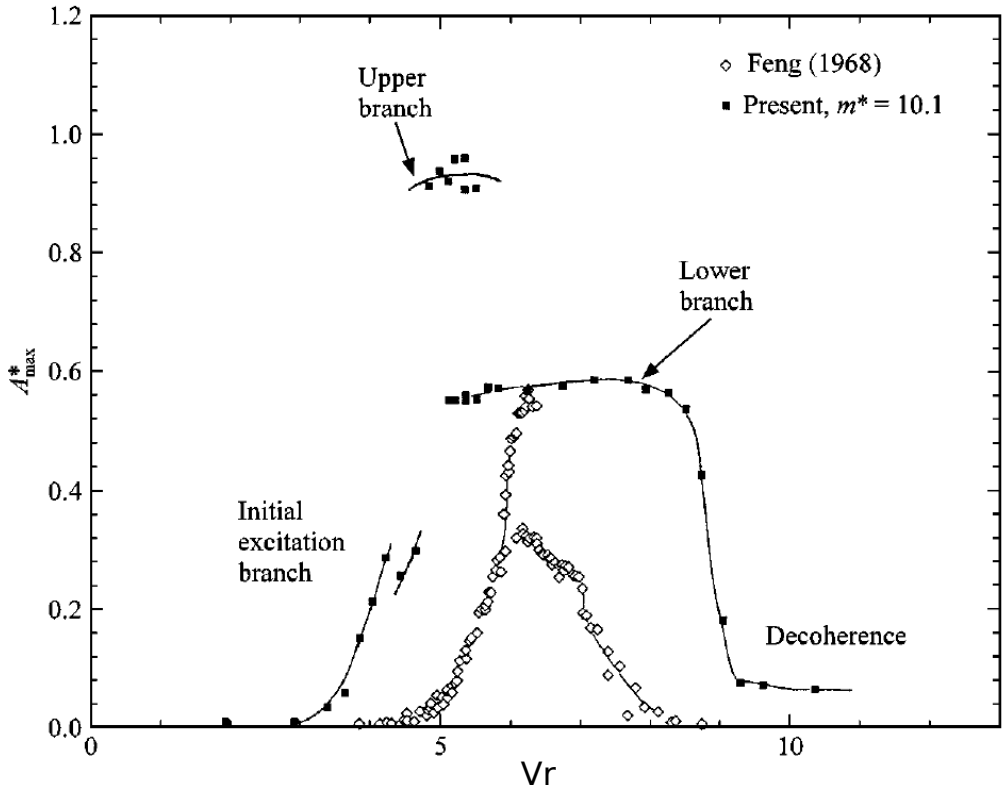

Source: Adapted from Khalak and Williamson (1999).

are associated with the vortex street type, as it is shown in Figure 5. The 2S pattern stands for two single vortices per cycle and appears in the initial branch. The second pattern 2P, two pairs of vortices per cycle, appears in free-vibrating and forced cylinders. Finally, the third pattern P+S stands for 1 pair plus 1 single vortices per cycle.

The frequency ratio for the synchronization region is shown in Figure 6. It appears that the frequency emission is kept near to the cylinder oscillation frequency during the lock-in range.

The influence of the mass on the dynamic response is evident. Therefore, Govardhan and Williamson (2002) studied the critical value in which the system changes its dynamics. The authors suggested a critical value of $m^* = 0.54$ for circular cylinders. In this case, systems with lower mass than the critical value does not present desynchronization.

Furthermore, studies of 1 degree-of-freedom (1dof) are more common in literature, considering the in-line or cross-flow direction. The researches which allow the cylinders to move in both direction are less usual. The vortex shedding frequency in the in-line direction is roughly twice the cross-flow frequency and the dynamics

Figure 5 – Vortex patterns in the wake of free-vibrating circular cylinders.

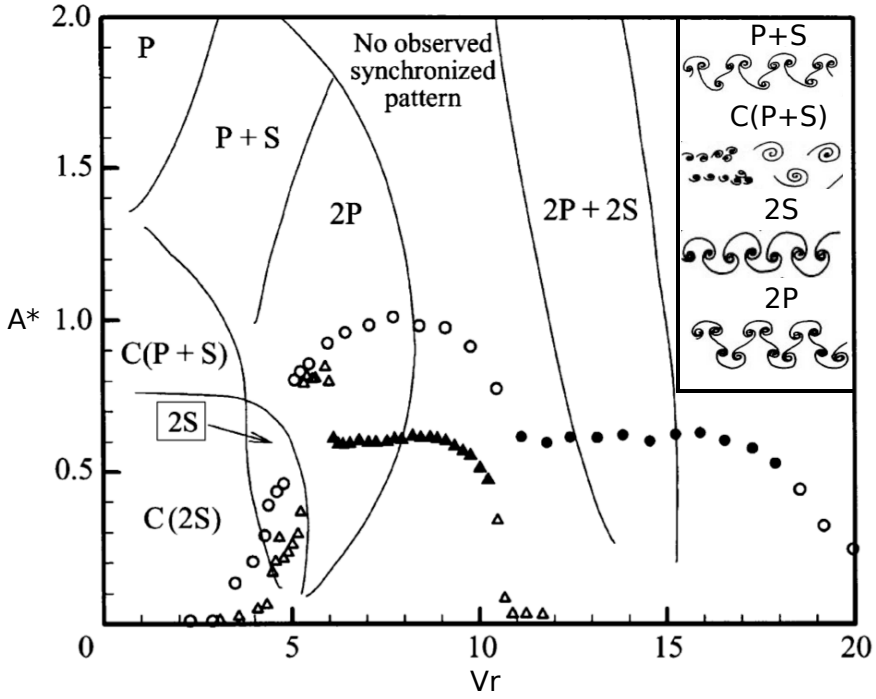

Source: Adapted from Williamson and Govardhan (2004).

allowing 2-degree-of-freedom (2dof) may be different from those with 1dof. Jauvtis and Williamson (2003) carried out experiments with 2dof to investigate the effect of the dof on the cylinder's response. The authors found no modification of the branch responses and wake patterns for a mass ratio greater than 6. However, values lower than 6 higher amplitudes (about 1.5 diameter) are found in a new branch with a wake pattern 2T, which is two triplets of vortex per cycle. This review does not discuss results of VIV of cylinders with two degree-of-freedom. However, the reader is encouraged to read articles related to the topic. Finally, aiming to sum up the types of VIV studies in order of complexity, the Table 2 exposes the main categories found in the literature.

One of the branches of VIV studies is the analytical formulation. Among many works can be highlight the model of Iwan and Blevins (1974) and Skop and Griffin (1973) for rigid cylinders. Also, the extension of these works where the van der Pol equation was modified for flexible cylinders applications, presented in Skop, Griffin et al. (1973) and Skop and Griffin (1975). Figure 7 brings the main contribution of the articles cited before, which is the non-dimensional parameter Skop-Griffin (S_G) as function of the maximum amplitude, where S_t is the Strouhal number, m^* is the mass ratio and $\overline{\zeta}$ is the damping factor (see Table 1).

The parameter S_G is given by Equation (2.4) for systems with constant mass

Figure 6 – Frequency ratio as function of reduced velocity for different mass.

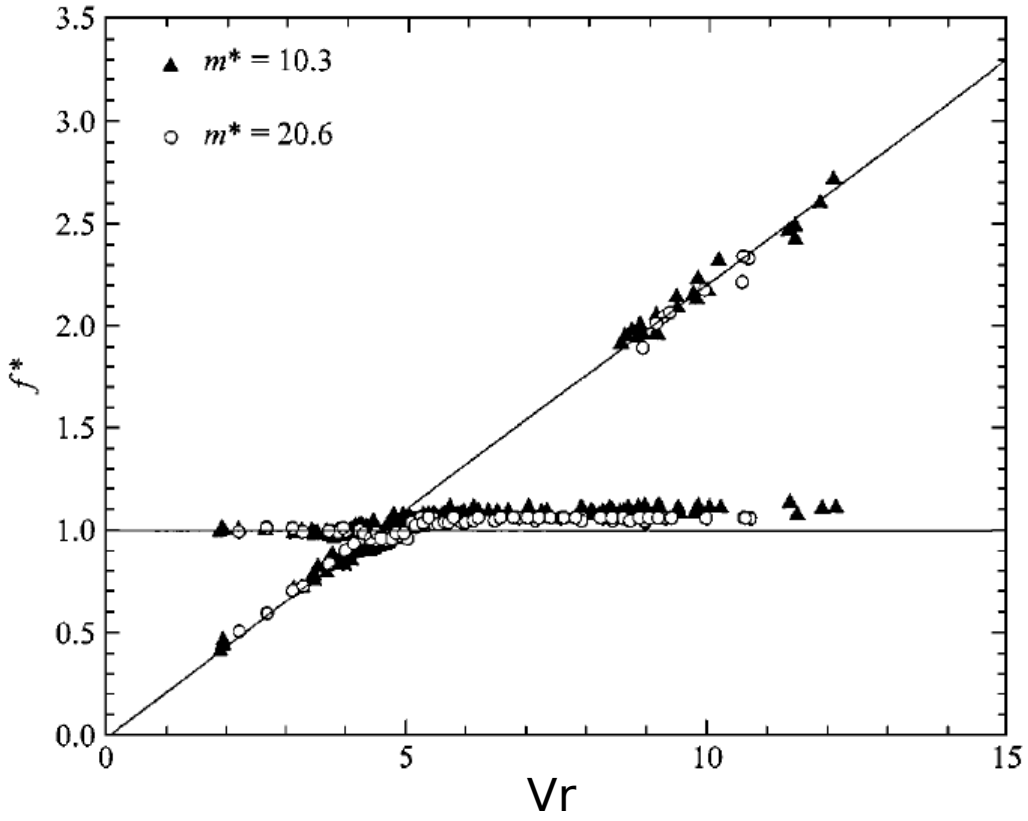

Source: Adapted from Khalak and Williamson (1999).

along the length.

$$S_G = 2\pi^3 S_t^2 m^* \overline{\zeta} \tag{2.4}$$

Furthermore, on the theoretical and experimental field, the research published by Vandiver (1993) brought an interesting interpretation for the added mass, mass ratio, and damping. The authors found that for low mass ratio systems the lock-in is wider and present higher amplitudes. These high amplitudes, self-excitation, and lock-in arise only if the synchronization between the vortex shedding and the movement occurs. This fact reinforces the idea that the wide synchronization is only possible with the increase of the frequency response with the flow velocity, which is associated with the variation of the added mass coefficient C_a along the lock-in. Another contribution of the authors was to rewrite the S_G equation to become independently of the system's mass, becoming a relation between the dissipative forces and the hydrodynamic excitation forces essentially.

The model S_G was revised in Skop and Balasubramanian (1997) and from studies of Khalak and Williamson (1999) the parameter accepted for the amplitude

Table 2 – Empirical and numerical studies of flow around cylinders.

Type of study	Main characteristics
Fixed	Measurement of lift and drag forces; visualization of vortex shedding patterns.
Forced	Imposition of movement in one or more frequencies; visualization of the vortex shedding as function of amplitude and oscillation frequency; observation of fluctuations on the forces.
Rigid with 1 degree of freedom	Simplification of complex cases restricting the movements in one direction; measurements of amplitude and frequency in an isolate direction; influence of parameters such as mass, damping and stiffness; observation of self-excitement and self-control mechanisms.
Rigid with 2 degrees of freedom	Movements in two directions, in-line and transverse to the flow incidence; measurements of coupled movements: trajectories and frequency relations.
Flexible cylinders	A system closer to real applications, with interaction between many vibration modes: shift between modes, effects of geometry, wave propagation; and flow profile.

Source: Vieira (2017).

prediction of VIV is given by Equation (2.5), where S_t is the Strouhal number, m^* the mass ratio, C_a the added mass coefficient and ζ the damping ratio (see Table 1).

$$S_G = 2\pi^3 S_t^2 (m^* + C_a)\zeta \tag{2.5}$$

This section introduced the VIV phenomenon and its main parameters in a concise way. The next subsection will expose characteristics of VIV of flexible cylinders only.

Figure 7 – The maximum amplitude of vortex-excited oscilation, A_{max}, for several flexible cylindrical structures with circular cross-section, as funtion of the response parameter S_G. Legend for the data points: $\times$, King (1977) in water, flexible cantilever, L(in water)/D = 20-33; $\bullet$, Vickery and Watkins (1964) in water, pivoted rod, $L/D = 15$; ▲, Vickery and Watkins (1964) in air, pivoted rod, $L/D = 14.2$; □, Hartlen, Baines and Currie (1968) in air, pivoted rod, $L/D = 13.8$; △, Scruton (1936) in air, flexible cantilever, $L/D = 27.5$; $+$, Dale, Menzel and McCandless (1966) in water, flexible cable of 1800 mm length and 2.5 mm diammeter, fourth through eighth modes; $\ominus$, Dale, Mesnzel and McCandless (1966) in water, flexible cable of 900 mm length and 2.5 mm diameter, second through fourth modes.

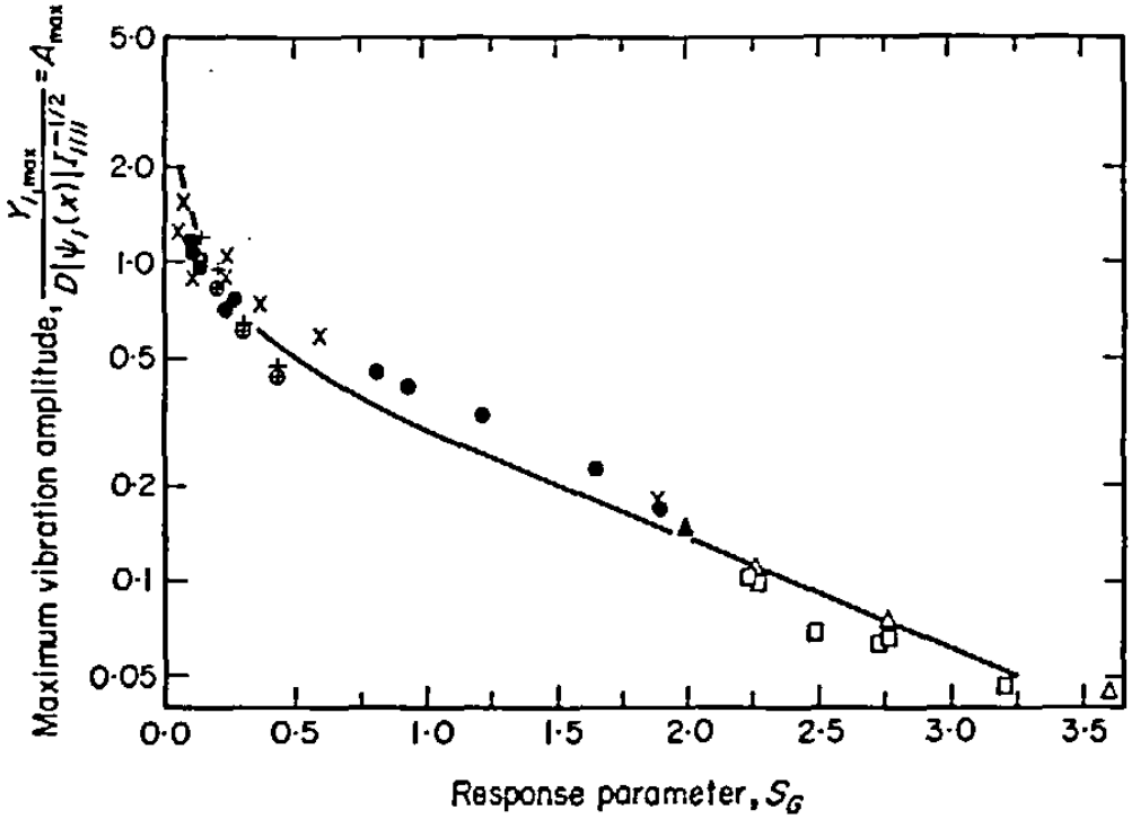

Source: Skop and Griffin (1975).

2.3 VIV of Flexible Cylinders

Although the study of VIV of rigid cylinders is fundamental for the phenomenon understanding, the most interesting case in the technological point of view is the study of flexible models. These models are similar to offshore structures and add complexity to the study because they have infinite vibrations modes with their respective frequencies, which allows the flexible models vibrate in infinite modes increasing the flow velocity and, consequently, the vortex shedding frequency as shown in Equation (2.2).

A vibration mode is defined by a natural frequency and a mode shape. According to Blevins (1979), a modal shape or eigenvector is a function which describes the

displacement of any location on the structure as the structure vibrates in a single mode. The natural frequency or eigenvalue is the frequency that the structure tends to vibrate when in motion. A structure has many natural frequencies and modal shapes. For instance, consider a uniform cable with bending rigidity near to zero presented in the Figure 8, which is similar to the flexible cylinder in this work. Where $T_0\ (N)$ is the mean tension, $p\ (N/m)$ is load per unit of length, $L\ (m)$ the length between connections and d (m) is the sag at the middle of the cable.

Figure 8 – Cable hanging in a shallow parabola.

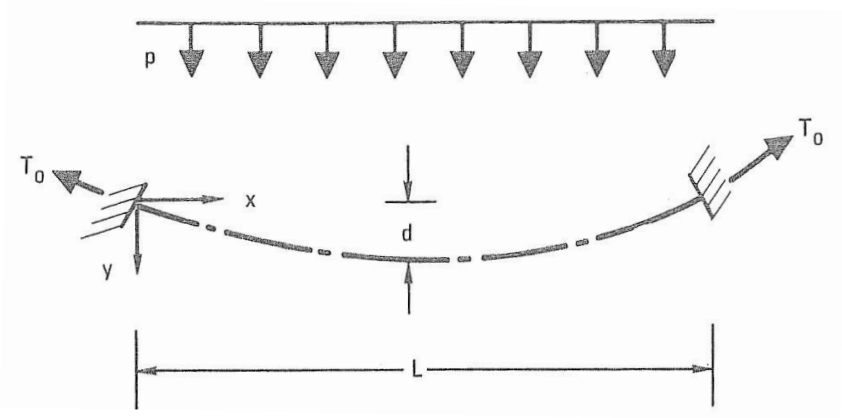

Source: Blevins (1979).

The parabolic function is shown in the Equation (2.6), and the maximum sag at the middle of the cable in the Equation (2.7).

$$\overline{Y} = \frac{pL^2}{2T_0}\left[\frac{x}{L} - \left(\frac{x}{L}\right)^2\right] \tag{2.6}$$

$$d = \frac{pL^2}{8T_0} \tag{2.7}$$

Consider that on this cable is imposed a initial displacement from the static condition. Then, when released, the cable starts to vibrate in the three components, horizontal motion in the catenary plane $X(x,t)$, vertical motion in the catenary plane $Y(x,t)$, and transverse motion out of the catenary plane $Z(x,t)$, as shown in Figure 9. The equations of the free vibration is associated with the mode shapes $\widetilde{x}$, $\widetilde{y}$ and $\widetilde{z}$. The partial equations are shown in Equations (2.8) to (2.10) (BLEVINS, 1979).

$$X(x,t) = \sum_i A_i \widetilde{x}_i(x) cos(\omega_i t + \phi_i) \tag{2.8}$$

$$Y(x,t) = \overline{Y}(x) \sum_i B_i \widetilde{y}_i(x) cos(\omega_i t + \psi_i) \tag{2.9}$$

$$Z(x,t) = \sum_i C_i \widetilde{z}_i(x) cos(\omega_i t + \xi_i) \tag{2.10}$$

Where ω_i (rad/s) is the natural frequency of the mode i, A_i, B_i (m) are constants and ϕ_i, ψ_i and ξ_i (rad) are the phase angles.

Figure 9 – Definition diagram for cable dynamic deflections X,Y, and Z.

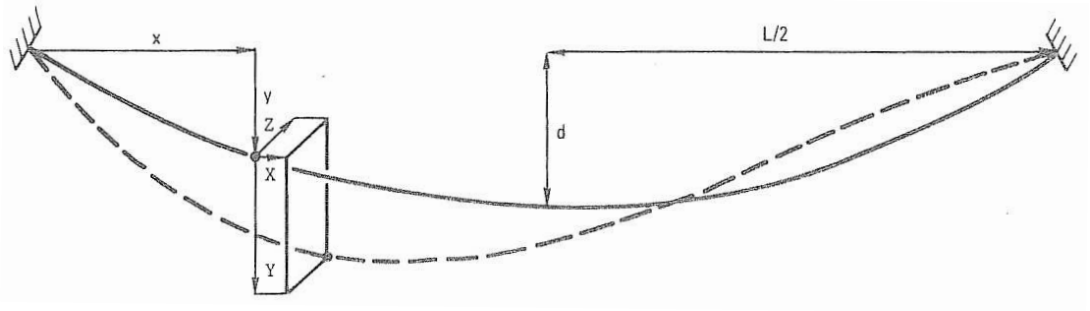

Source: Blevins (1979).

Further, the Figure 10 shows the first symmetric and antisymmetric in-plane cable modes. The equation for the frequency of the mode i out of plane and in-plane antisymetric modes is shown in Equation (2.11), where m is the mass of the cable per unit of length. Also, Equation (2.12) shows the frequency of in-plane symmetric plane, where λ_i is solved by the roots of Equation (2.13). E (Pa) is the cable modulus and A (m^2) the cross-section area (BLEVINS, 1979).

$$\frac{i}{L}\left(\frac{T_0}{m}\right)^{1/2} \; ; \quad i = 1, 2, 3, ... \tag{2.11}$$

$$\frac{\lambda_i}{2L}\left(\frac{T_0}{m}\right)^{1/2} \; ; \quad i = 1, 2, 3, ... \tag{2.12}$$

$$\begin{aligned} &tan\left(\tfrac{\pi\lambda}{2}\right) = \tfrac{\pi\lambda}{2} - \tfrac{4}{\alpha^2}\left(\tfrac{\pi\lambda}{2}\right)^3 \\ &\alpha^2 = \left(\tfrac{8d}{L}\right)^2 \tfrac{EA}{T_0}\tfrac{L}{L_e} \\ &L_e \approx L\left[1 + 8\left(\tfrac{d}{L}\right)^2\right] \end{aligned} \tag{2.13}$$

Finally, the mode shapes are given by Equations (2.14) to (2.16) for the out-of-plane mode, in-plane antisymmetric mode and in-plane antisymmetric mode, respectively (BLEVINS, 1979).

$$\begin{bmatrix} \widetilde{x} \\ \widetilde{y} \\ \widetilde{z} \end{bmatrix}_i = \begin{bmatrix} 0 \\ 0 \\ sin(i\pi x/L) \end{bmatrix} \; ; \quad i = 1, 2, 3, ... \tag{2.14}$$

$$\begin{bmatrix} \widetilde{x} \\ \widetilde{y} \\ \widetilde{z} \end{bmatrix}_i = \begin{bmatrix} -\frac{1}{2}\left(\frac{pL}{T_0}\right)\left[\left(1 - \frac{2x}{L}\right) sin\left(\frac{2i\pi x}{L}\right) + \frac{1}{i\pi}\left(1 - cos\frac{2i\pi x}{L}\right)\right] \\ sin(i\pi x/L) \\ 0 \end{bmatrix} \; ; \quad i = 1, 2, 3, ... \tag{2.15}$$

Figure 10 – First symmetric and antisymmetric in-plane cable modes.

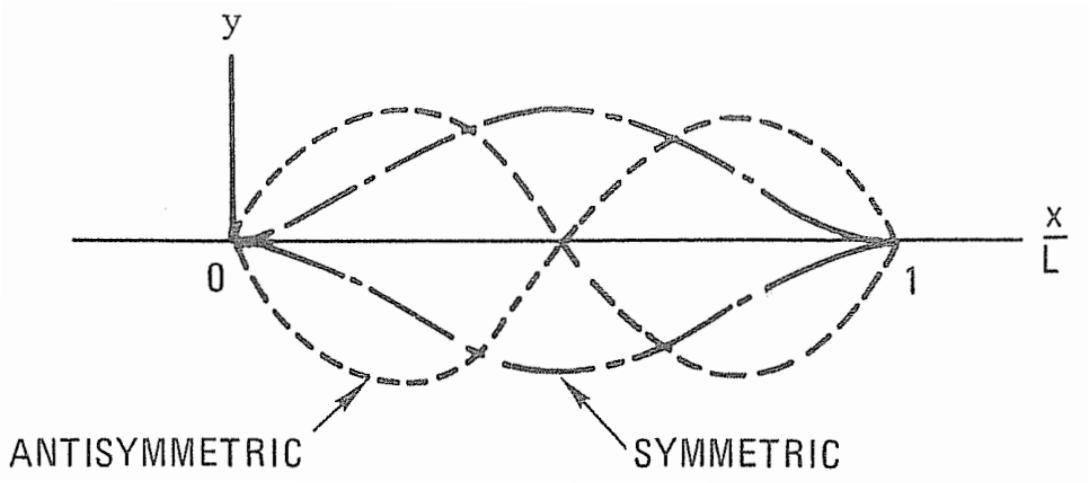

Source: Blevins (1979).

$$\begin{bmatrix}\widetilde{x}\\ \widetilde{y}\\ \widetilde{z}\end{bmatrix}_i = \begin{bmatrix} \frac{pL}{T_0}\left(\frac{(\pi\lambda_i)^2}{\alpha^2}\frac{L_x}{L_e} - \frac{1}{2}\left(1-\frac{2x}{L}\right)\right)\left[1 - tag\left(\frac{\pi\lambda_i}{2}\right)sin\left(\frac{\pi\lambda_i x}{L}\right) - cos\left(\frac{\pi\lambda_i x}{L}\right)\right] \\ -\frac{1}{\pi\lambda_i}\left\{\left(\frac{\pi\lambda_i x}{L}\right) - tan\frac{\pi\lambda_i}{2}\left[1-cos\left(\frac{\pi\lambda_i x}{L}\right)\right] - sin\left(\frac{\pi\lambda_i x}{L}\right)\right\} \\ 1 - tan\left(\frac{\pi\lambda_i}{2}\right)sin\left(\frac{\pi\lambda_i x}{L}\right) - cos\left(\frac{\pi\lambda_i x}{L}\right) \\ 0 \end{bmatrix}; \quad i = 1,2,3,...$$

$$Lx = L\left\{\left(\frac{x}{L}\right) + 24\left(\frac{d}{L}\right)^2\left[\left(\frac{x}{L}\right) - 2\left(\frac{x}{L}\right)^2 + \frac{4}{3}\left(\frac{x}{L}\right)^3\right]\right\} \tag{2.16}$$

In risers, the excitation of high modes affects the fatigue lifetime of real structures because of the higher curvatures. Furthermore, the high aspect ratio (ratio between the length and the external diameter) and the shear flow profile result in responses of different modes on different regions of the structure. Therefore, the study of VIV on flexible cylinders are more complex and closest to the industrial reality, and naturally, many academic investigations are driven to these cases.

The axial stiffness and the axial tension are also essential parameters in flexible structures. It is expected that for uniform flows the structure presents one dominant frequency, excited by the vortex shedding. However, the mechanisms that govern the phenomenon is not precise, and the prediction of VIV in flexible structures is not fully validated yet.

Several recent works have been experimentally studying the multi-modal dynamic response of flexible structures due to fluid excitation. Chaplin et al. (2005b) carried out in a towing tank a flexible cylinder model. The cylinder was $13.12\ m$ long, $28\ mm$ of diameter and $m^* = 3$. The model was totally immersed in water, as shown in Figure 11.

The model was partially excited (45% of the length) in the uniform current up

Figure 11 – Experimental setup of Chaplin et al. (2005b) for a vertical flexible cylinder.

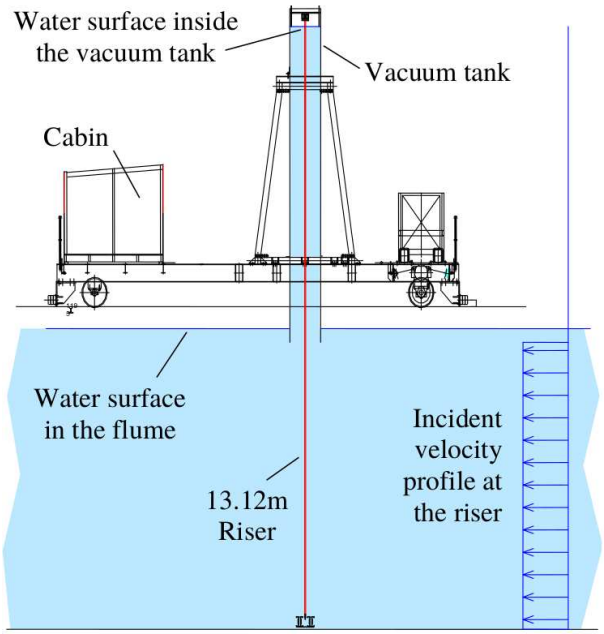

Source: Chaplin et al. (2005b).

to $1\ m/s$. The Figure 12 shows the multi-modal responses found. The series A-E are different values of axial tension and the values $n = 1,\ 2$ ... represent the natural modes of the structure. It is possible to identify the successive excitation of the natural modes and frequently the overlap between them. While the velocity increases, there are shifts of one dominant mode to another. It was observed that the amplitude increases with the velocity until the change of the dominant mode when there is a sudden amplitude drop. The authors state that the maximum amplitude is a combination of two or three fundamental modes, although the structure vibrates in the dominant mode.

Further, Huera-Huarte (2006), Huera-Huarte and Bearman (2009b) and Huera-Huarte and Bearman (2009a) conducted experiments of VIV on a flexible cylinder in a towing tank varying the top tension. The model was $1.5\ m$ long and $16\ mm$ wide with $m^* = 1.8$ in a Re range from 1200 to 12000. The authors found cross-flow amplitudes up to 0.7 diameter and in-line over 0.2 with a dominant frequency of $St = 0.16$. These findings are different from rigid cylinders, where amplitudes up to 1.5 diameters were verified. The variation of the top tension showed that the increase of tension makes the model behave like a cable making the lower branch disappear.

As mentioned before, the relevance of the study of flexible cylinders is mostly related to the offshore industry. The slender, flexible risers are an example, and they are also under VIV action. In this scenario Malta (2015) investigated the VIV on catenary risers with transversal current incidence varying with the depth, and Pereira (2015) with a longitudinal and transversal flow in a towing tank. The catenary risers were also

investigated by Vieira (2017) for varied angles of yaw and azimuth.

Malta (2015) applied the modal projection, also used in the present work, and states that it enabled the analysis of typical features of VIV in catenary risers, which the author says to be similar to long flexible lines, such as the successive modal synchronization gradually overlapping with the increase of the mode order. This was found independently of the velocity profile. Further, the synchronization appears to start around to $Vr = 4$. The author claims that the modal projection is useful in the analysis of multi-modal behavior and a powerful tool for comprehension of VIV mechanisms. However, the modal projection is strongly dependent on the modal characterization of the model (mode shape and frequency).

Pereira (2015) also applied the modal projection procedure and stated that it is essential for the experimental analysis because the phenomenon is highly non-linear with multi-modal behavior. The coexistence of multiple modal contributions is found near to the modal transition. On the other hand, in the peaks of the VIV resonance, only the dominant mode is identified. Some cases, the transition showed the modal contribution of several modes in another frequency and not in their natural mode.

Vieira (2017) found unimodal excitation for the first mode and multi-modal behavior for the others. The author tested the independence principle, which states that the tangential velocity portion does not influence the oscillatory behavior due to VIV, and found it is suitable to predict the cases carried in his work.

In these works, it was observed the successive natural modes synchronization with the increase of the velocity. Also, the coexistence of several modes in the lock-in vibrating in the dominant mode. An example of the modal analysis is shown in Figure 13. The studies clearly indicate the complexity of the system response due to VIV excitation and the application of sophisticated tools for experimental results interpretation. Therefore, the current work also will use these tools for analysis of the experimental results and VIV mechanisms understanding.

This chapter reviewed the essential aspects related to VIV. The phenomenon was exposed for rigidly fixed cylinders, rigid cylinders with dof, and finally for flexible structures. The works presented for flexible structures in catenary risers have shown a non-linear and multi-modal behavior, which is also expected in this work. Many publications have been studying the VIV phenomenon in a flexible cylinder. However, none of them have completed a direct measurement of the displacements. The present work intends to present a flexible cylinder case with directed measurements and a varied set of analysis.

Figure 12 – Measurements of (a) cross-flow response frequencies and (b-h) standard deviations of cross-flow modal weights as functions of reduced velocity. A line in (a) indicates the double Strouhal frequency corresponding to a Strouhal number of 0.17. All plots in (b-h) have identical scales. Data from all series are shown in (b-h); those from series C and D are omitted from (a).

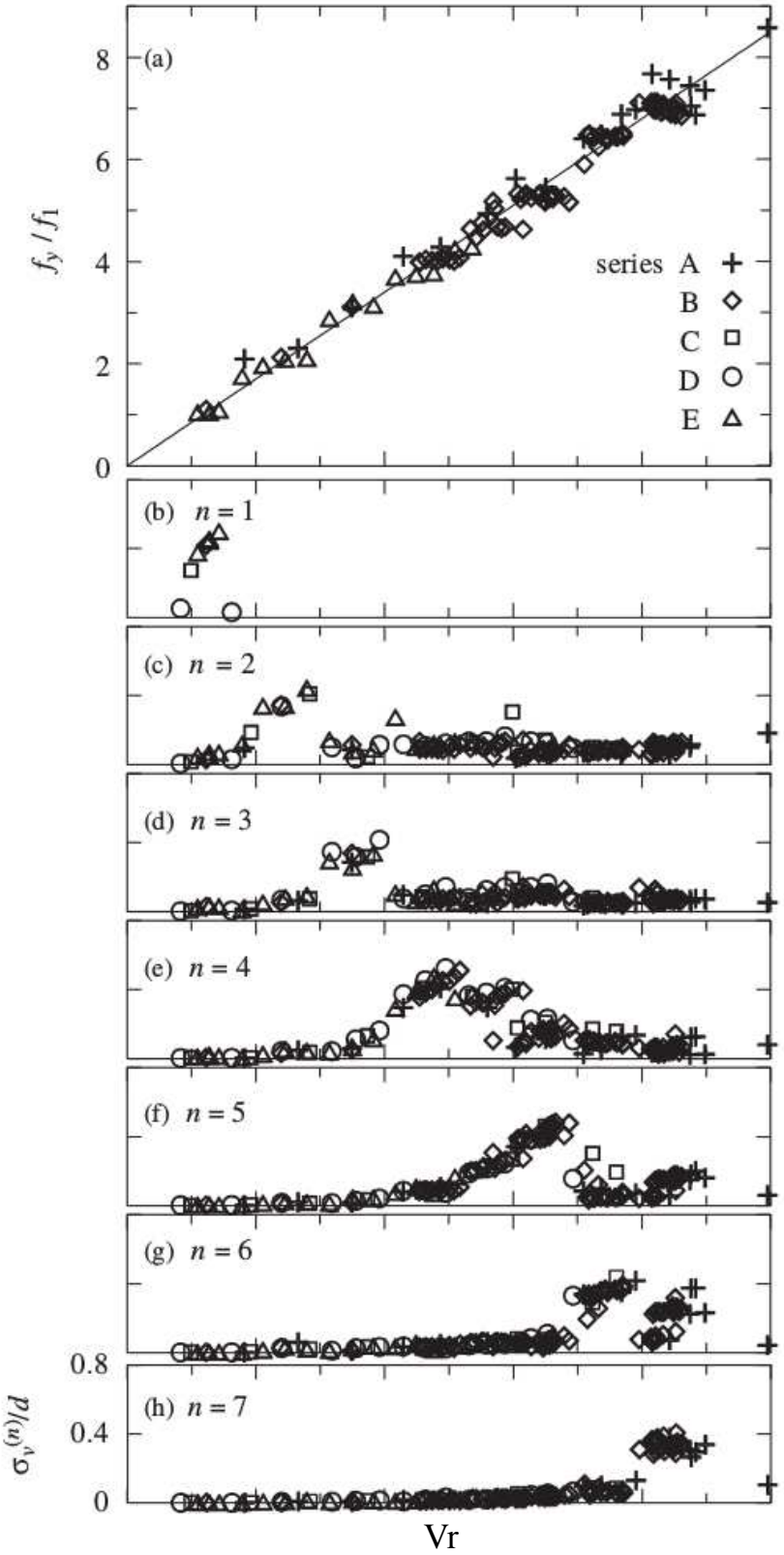

Source: Adapted from Chaplin et al. (2005b).

Figure 13 – Modal amplitudes of VIV of a catenary riser as function of the reduced velocity. Figure on the top: maximum amplitude. Figure on the middle: minimum amplitude. Figure on the bottom: r.m.s. amplitude.

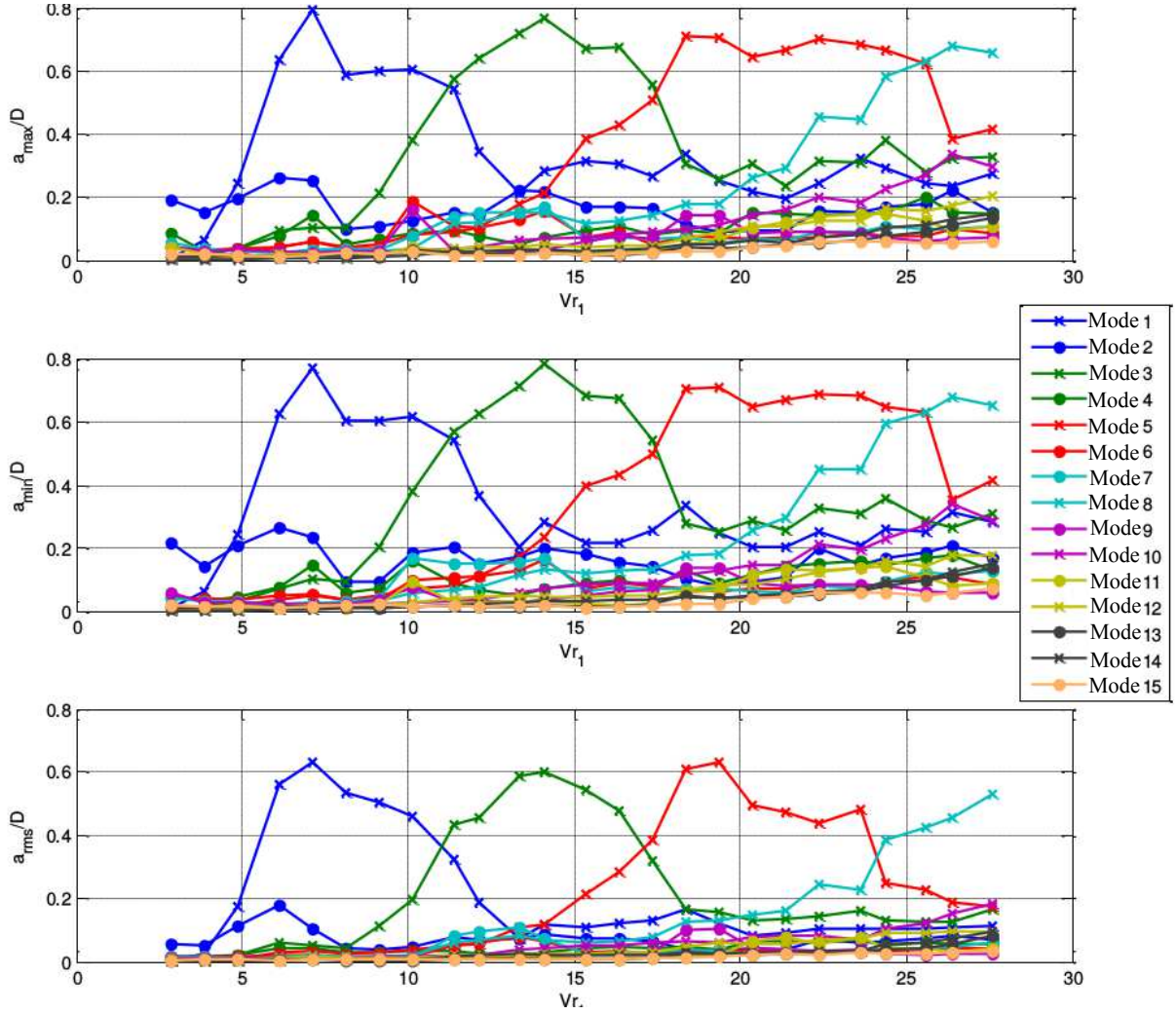

Source: Adapted from Pereira (2015).

3 METHODOLOGY

In this chapter, details are given of the analysis applied to the experimental results. Also, the experimental set up is described in details.

For the sake of understanding, the coordinate system was defined as follows. In-line or x-direction corresponds to the in-flow, the cross-flow to the vertical or z-direction, and the span-wise identified by y-direction. It is important to highlight that frequencies f_{ni} and modes $\mathcal{M}_i$ are referred according to the subscript, i.e. when i is odd they are related to the in-line plane, otherwise to the cross-flow plane. For instance, the Figure 14 shows the first four modes. The lines in red are the same shape, but in different planes according to the subscript, $\mathcal{M}_3$ for the in-flow plane and $\mathcal{M}_4$ for the cross-flow. Furthermore, the subscript is also used for the vibration frequency.

Figure 14 – Notation for the modes and frequencies according to the vibration plane.

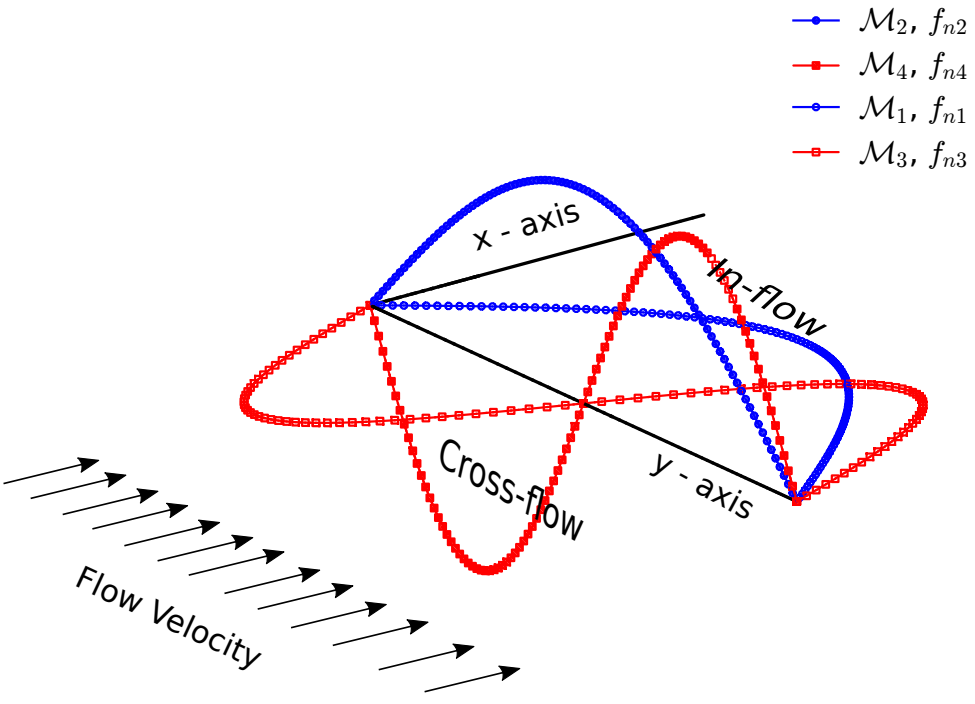

Source: The Author (2019).

3.1 Experimental Set Up and Instrumentation

The experiment was carried out in the Institute for Technological Research towing tank, located at São Paulo State, Brazil. This facility is $280\ m$ long, $6.6\ m$ wide

and $4\ m$ deep. The Reynolds number range tested was from $1,000$ up to $10,000$. The flexible cylinder was towed in 20 reduced velocities motoring displacements of 18 targets points along the model's length.

A structural support was mounted on the towing tank, as shown in Figure 15. The model was placed on the structure so that the distance of the model from the free surface and false bottom was around 52 diameters. This distance is enough to avoid interference of the boundary layer of the false bottom and the interaction between the model and the free surface.

Figure 15 – Layout of the present experiment. Right: Front view. Left: 3D view.

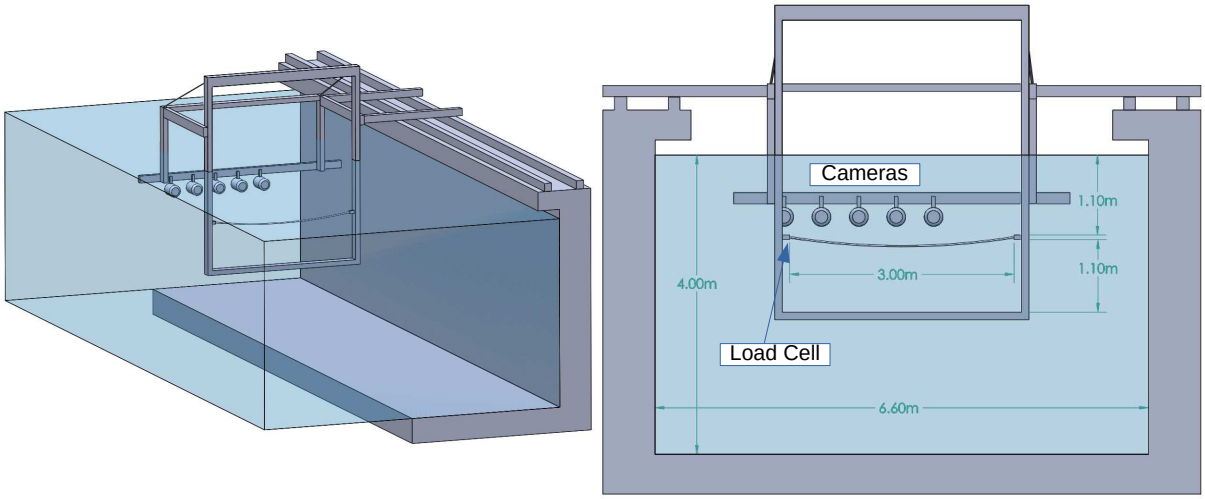

Source: The Author (2019).

The flexible cylinder was horizontally fixed by means of two ball joints, which allows rotations but no translations. Further, in order to access the axial force, an unidirectional load cell was attached in one of the ends. This load cell was important to obtain the initial traction imposed on the flexible cylinder. The load cells is shown in Figure 16.

The movements of the model were directly measured by an optical system of five sub-aquatic cameras, shown in Figure 17, which track targets placed along the model. Further, the length of the model is frequently described by the curve-linear position s divided by the total deformed length L. The curve-linear position of the target j and the total length were calculated according to Equations (3.1) and (3.2), where $i = 0$ represents the target on zero position and N the target located at the middle of

the model.

$$s_j = \sum_{i=1}^{j} \sqrt{(\Delta x_i - \Delta x_{i-1})^2 + (\Delta y_i - \Delta y_{i-1})^2 + (\Delta z_i - \Delta z_{i-1})^2} \tag{3.1}$$

$$L = 2\sum_{i=1}^{N} \sqrt{(\Delta x_i - \Delta x_{i-1})^2 + (\Delta y_i - \Delta y_{i-1})^2 + (\Delta z_i - \Delta z_{i-1})^2} \tag{3.2}$$

In this experiment, eighteen reflective targets were used, from $s/L = 0$ to $s/L = 0.56$, also shown in Figure 17. The tracking of 56% of the model's length was enough to reconstruct the whole position of the system. This is possible because of the vibration modes may be inferred using the frequency response and half of the mode shape (symmetric or antisymmetric).

Figure 16 – Unidirectional load cell used for the traction control.

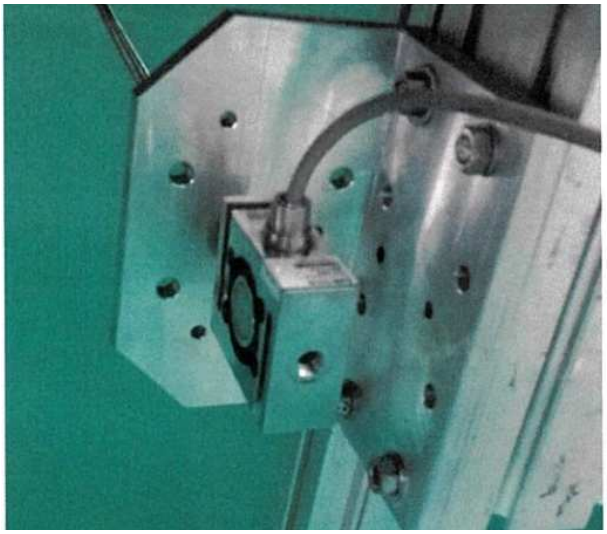

Source: The Author (2019).

Figure 17 – Instrumentation. Left: Sub-aquatic cameras. Right: Flexible cylinder model.

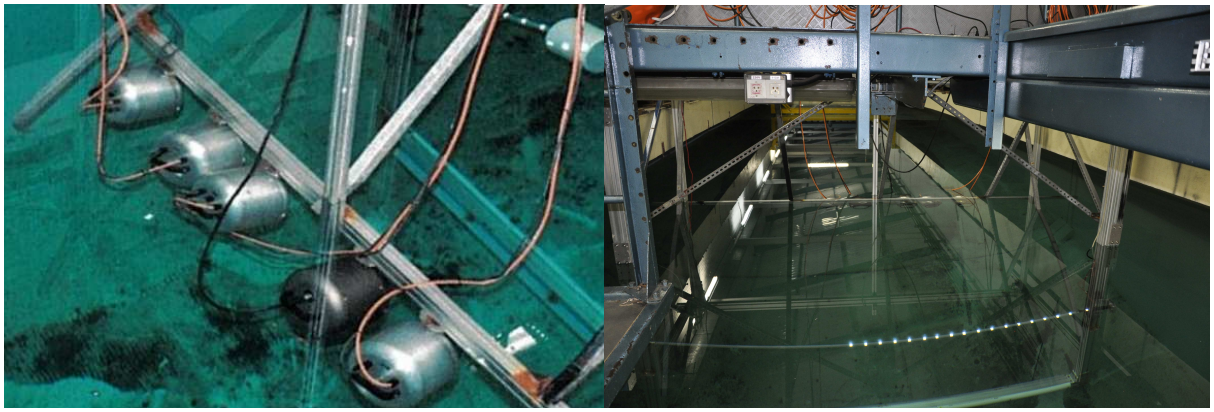

Source: The Author (2019).

The carriage car was towed only in one direction. In this way, the cameras are always far downstream and, consequently, never upstream. This method avoid the interference of the cameras in the experiment. The experiment was carried for 20 velocities, from $Vr = 1.75$ to $Vr = 15.79$. This corresponds to a Reynolds number range from $Re = 1065$ to $Re = 9488$. The reduced velocity (Vr) was calculated according to Equation (3.3), where U stands for the towing velocity and D the model's external diameter. The frequency f_{n2} corresponds to the frequency of $\mathcal{M}_2$, according to the description explained in the Figure 14.

$$Vr = \frac{U}{f_{n2}D} \tag{3.3}$$

The following Figures 18 to 20, show the data acquisition example and trajectory construction of the experiment. For the sake of conciseness, although 18 targets were monitored, only 5 targets were shown from $s/L = 0.1$ to $s/L = 0.5$. It is important to highlight that, although these are somehow results of the present work, they are presented in the methodology section to provide information about the signal quality and inform the reader about the analysis applied in the result section. In this way, the result section is focused on the result of modal projection, frequency, amplitude, and relative phase angle, instead of signal treatment.

In the Figure 18 is shown the mean deflection of the flexible cylinder. Also, the reconstruction of the movements found during the experiment for $Vr = 6.03$ is shown. The black traces are the targets movements from $s/L = 0$ to 0.5, and the gray traces the mirrored targets. The bottom subplots show the trajectory minus its mean values for the same targets.

In the Figures 19 and 20, the first row of graphs, on the left, exhibits a zero condition and a transient part of the experiment until around 100 seconds. These parts of the signal were not taken for the analysis. The second and third column show respectively the zoom in from 150 and 154 seconds and the spectrum from a Fourier Transform of the signal. The last two graphs on the bottom shows, deflection of the flexible cylinder over 4 seconds, the mean deflection of the model and the r.m.s values (Equation (3.4)).

Looking closer the Figure 18 some features may be identified. For instance, the top graph shows the deflection of the flexible cylinder caused by the drag, which is about 4.5 diameters for this reduced velocity. In addition, the weight creates a deflection as well, which is around 4 diameters. The bottom figures provide information about the trajectory in several locations. It is interesting to point out that the amplitude response increases as the location goes towards the middle. In the middle, the trajectory differs from the other points.

The Figures 19 and 20 bring several features of the experiment as well. For instance, the first and the second column of graphs exhibit the quality of the data. The

Figure 18 – Example of coupling motion in $Vr = 6.03$ and $Re = 3670$. Top figure represents the flexible cylinder mean deflection, black trajectories are the monitored targets and gray trajectories are the mirrored targets. Bottom figures are the trajectories minus its mean value from $s/L = 0.1$ to $s/L = 0.5$.

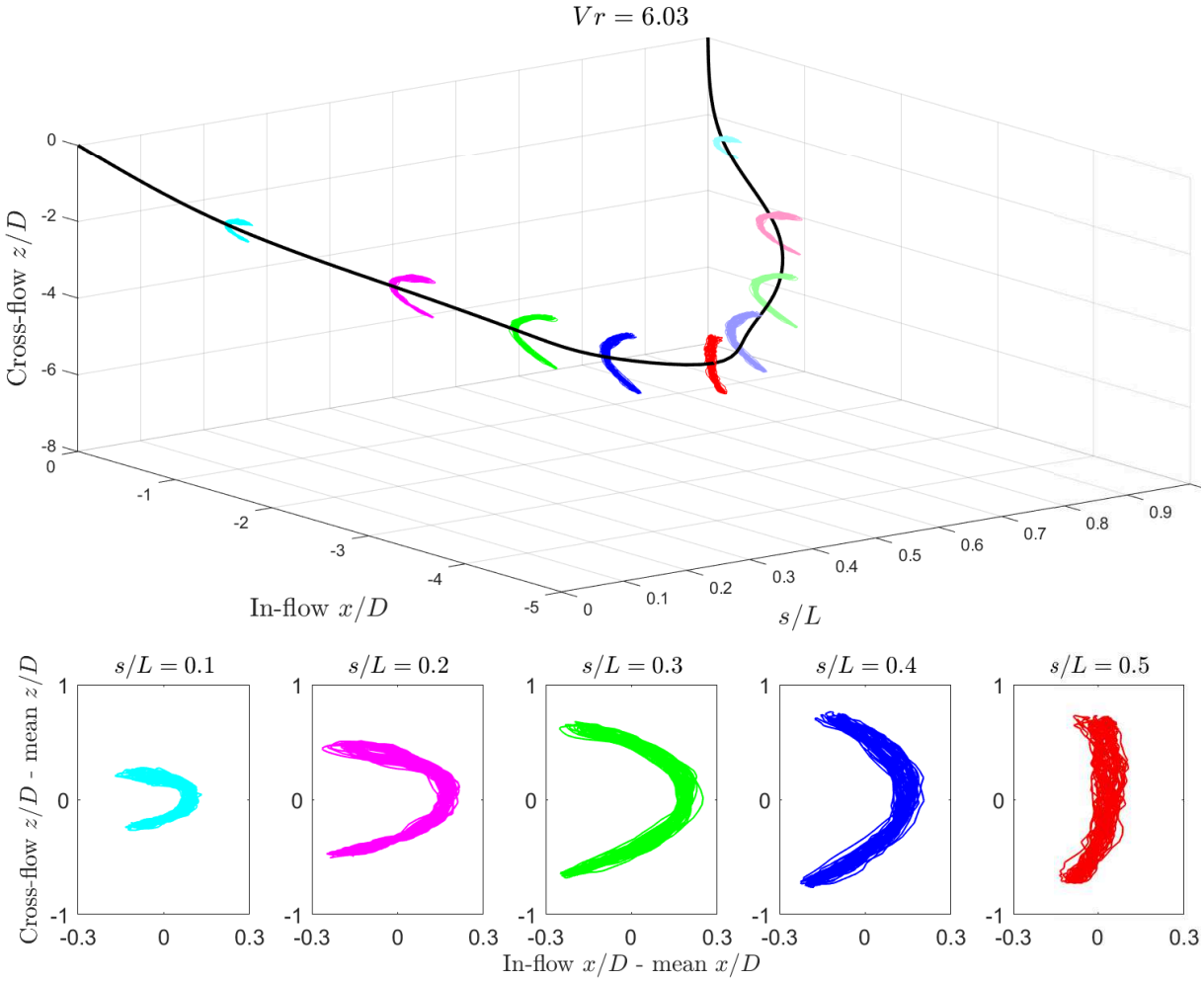

Source: The Author (2019).

acquisition time of 350 seconds is more than enough to achieve the steadiness of the phenomena. Also, the smoothness of the curves is due to the high acquisition frequency of $100\ Hz$. The last column of figures exhibit the sharp peak of the Fourier Transform in its correspondent location, showing the good results also in the frequency domain. Furthermore, the sixth row of Figure 19 indicates the vibration mode shape, in this case, $\mathcal{M}_2$, which was defined as the first transversal mode according to Figure 14. Finally, this mode can be seen as it is in the experiment, with the real deflection of the flexible cylinder, as shown in the last subplot. The same is valid for Figure 20. However, the mode $\mathcal{M}_3$ is shown in the graph on the sixth row. The different mode shape is due to the different excitation frequency in the in-flow direction ($f_z \approx 2f_x$), and consequently,

excitation of a different mode.

Figure 19 – Example of signal acquisition in $Vr = 6.03$ and $Re = 3670$. Graphs (a)-(e) are the cross-flow amplitude $z/D-$mean z/D in 5 targets of all runtime. Graphs (f)-(j) presents a zoom in from 150 to 154 seconds. Graphs (k)-(o) are the power density spectrum of the signal (80 to 330 seconds). Graph (p) is the monitored targets cylinder deflection minus its mean value, solid lines represent $\frac{1}{10}$ of a second during 150 to 154 seconds, dashed line represents the r.m.s. cross-flow amplitude. Graph (q) is the monitored targets cylinder deflection, solid lines represent $\frac{1}{10}$ of a second during 150 to 154 seconds, dashed line represents the mean value, δ is the mean value in the center.

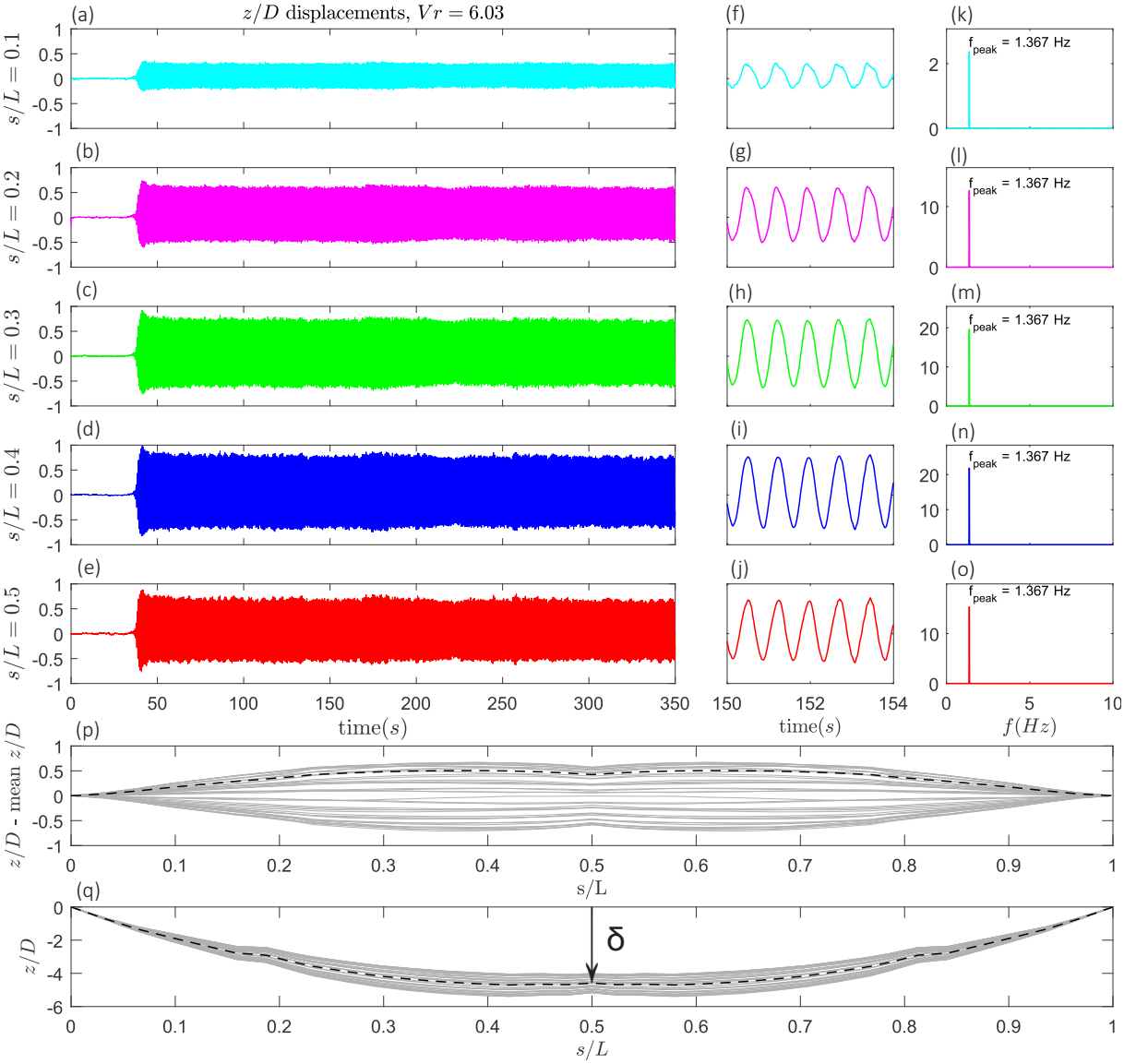

Source: The Author (2019).

Figure 20 – Example of signal acquisition in $Vr = 6.03$ and $Re = 3670$. Graphs (a)-(e) are the in-line amplitude x/D in 5 targets of all runtime. Graphs (f)-(j) presents a zoom in from 150 to 154 seconds. Graphs (k)-(o) are the power density spectrum of the signal (80 to 330 seconds). Graph (p) is the monitored targets cylinder deflection minus its mean value, solid lines represent $\frac{1}{10}$ of a second during 150 to 154 seconds, dashed line represents the r.m.s. in-line amplitude. Graph (q) is the monitored targets cylinder deflection, solid lines represent $\frac{1}{10}$ of a second during 150 to 154 seconds, dashed line represents the mean value.

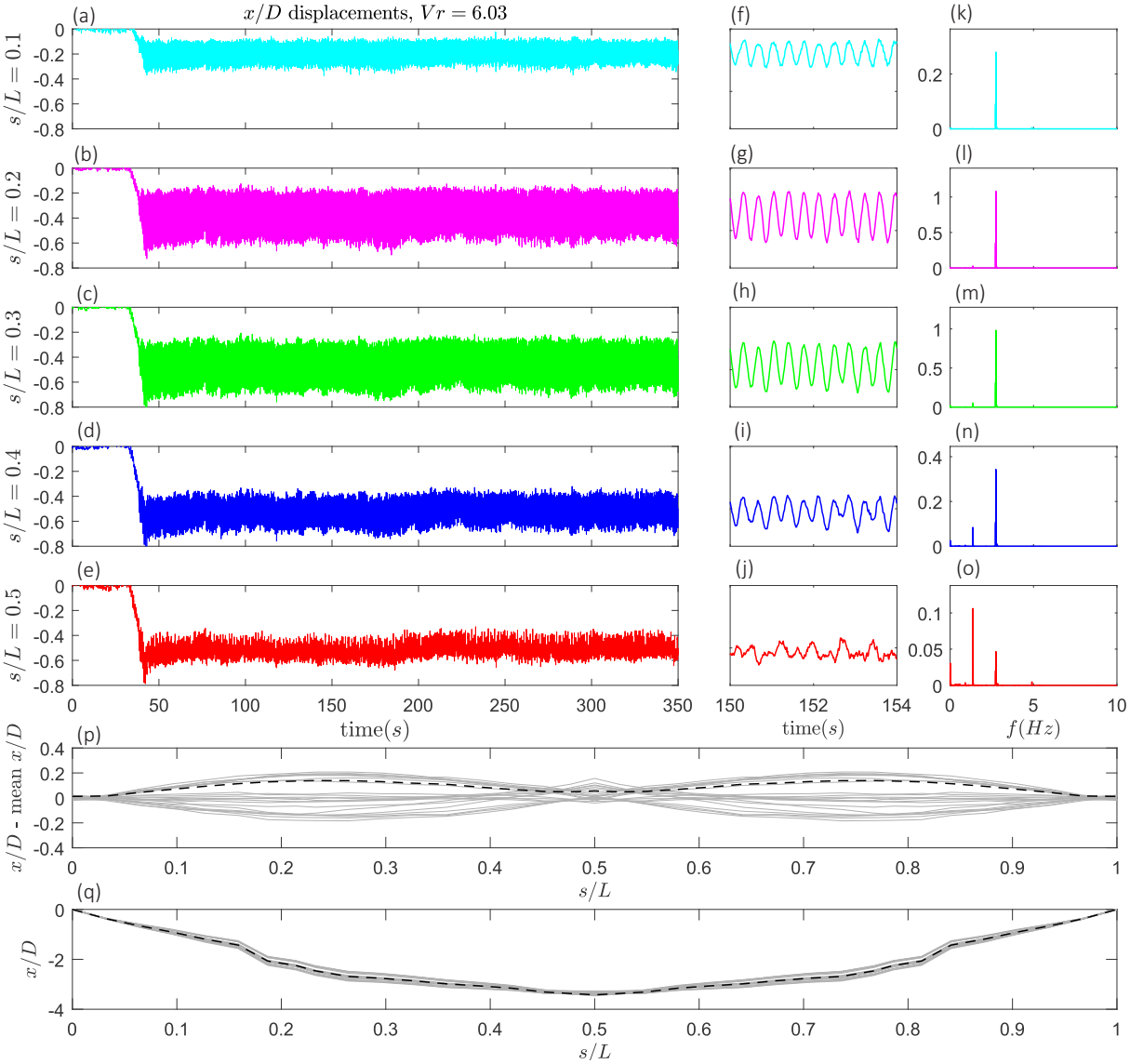

Source: The Author (2019).

Considering the results section, all target signals were treated such the transient part of the signal was removed and only the part where the peaks were steady. As an example, in Figure 19 and Figure 20 only the time series between 80 seconds and 330 seconds were used. Each treated target signal was offset such the mean value was zero and then the r.m.s. the value presented in the amplitude analysis was taken according

to Equation (3.4), where N is the number of elements and g is the displacement vector.

$$r.m.s(g) = \sqrt{\frac{1}{(N-1)}\sum_{i=1}^{N}(g_i)^2} \tag{3.4}$$

In the last section of the result section, a maximum amplitude is presented. This was obtained by taking the mean value of the 10% of the highest peaks.

3.2 Flexible Cylinder Characterization and Experimental Procedure Tests

The long flexible cylinder was build of a silicone hose filled with $2.3\ mm$ stainless micro-spheres. The combination of these materials created a model with low bending stiffness but a considerable axial rigidity. The model is shown in Figure 21. This configuration resulted in similar frequencies and damping for the modes $\mathcal{M}_1$ and $\mathcal{M}_2$. It is important to highlight, once again, that these modes have the same shape, but different vibration planes according to Figure 14. The flexible cylinder model was similar to those used for VIV experiments reported in Pereira et al. (2013b), Franzini et al. (2016a), Franzini et al. (2016b), Pereira et al. (2016), Pereira et al. (2013a). For more details regarding the scaling methodology of this flexible cylinder, the article Rateiro et al. (2012) provides the complete analysis and dynamic similarity. Finally, the data of the flexible model used in the present work is shown in Table 3.

Figure 21 – Flexible cylinder model used in the present work.

Source: The Author (2019).

The damping values were calculated through decay tests in air (structural damping) and water (total damping). Both experiments were carried out imposing the

same tension on the model. The linear damping was obtained using an exponential regression, shown in Equation (3.5). For the structural damping (ζ_{s2}) four consecutive tests were conducted with one excitation point located at $s/L = 0.5$, the mean of the four tests finds the final damping value. The modal nomenclature exposed in Figure 14 is valid for the damping, therefore, the subscript i.e 2 stands for the damping of the mode $\mathcal{M}_2$ and the letter s for structural damping. For ζ_{s4}, two points were excited, at $s/L = 0.25$ and 0.75. Regarding the total damping (ζ_{t2}), also four consecutive tests were carried out, with one excitation point at $s/L = 0.5$. The nomenclature in this case is the same, 2 stands for the mode $\mathcal{M}_2$ and t inform that it is the total damping. The natural frequencies are obtained through a Fourier analysis of the same signal. For more pieces of information see Appendix A.

$$F = Ae^{-\zeta\omega_n t} \tag{3.5}$$

Table 3 – Data of the designed model

Property	Value	Unit
External diameter (D)	21	mm
Internal diameter (D_i)	16	mm
Flexible cylinder initial length (L_i)	2690	mm
Distance between connections (L_f)	3000	mm
Flexible cylinder deformed length (L)	3111	mm
Mass (m)	3.359	kg
Wet weight (w_s)	22.4	N/m
Mass ratio (m^*)	3.9	$-$
Aspect ratio (L/D)	148	$-$
Axial stiffness (EA)	1.3	kN
Bending stiffness (EI)	4×10^{-5}	kNm^2
Axial traction (T)	72	N
Natural frequency of $\mathcal{M}_1$ f_{n1}	1.39	Hz
Natural frequency of $\mathcal{M}_2$ f_{n2}	1.38	Hz
Total Damping ζ_{t2}	9.65	$\%$
Structural Damping $\mathcal{M}_2$ (ζ_{s2})	2.69	$\%$
Structural Damping $\mathcal{M}_4$ (ζ_{s4})	0.25	$\%$

Source: The Author (2019).

Regarding the experimental procedure, the following is described for the decay tests in water and the VIV experiments.

- The model is first weighed outside the water, where it is also fixed on the structural support with the load cells and the ball joints;
- The tension is imposed, and the functionality of the load cells are verified;
- The targets are displayed along the model and then it is positioned on the water where the traction checked again;

- The cameras are calibrated to track the targets.

After these procedures and calibrations, the model is ready for the decay tests and the VIV experiments. During the VIV experiments, the model is towed 350 seconds, and after this time the towing structure stops. When it stops, although the towing structure is stationary, the movements on the flexible cylinder is still present. In order to avoid starting a new run while the flexible cylinder is moving, each run starts only if the tracking system exhibits that the movements of the target locations are within the tracking system uncertainty.

Finally, the Table 4 brings the plan and the execution of the runs.

Table 4 – Experiment's planning and execution.

	Planned		Executed
ID	$U\ (m/s)$	V_r	V_r
01	0.05	1.73	1.75
02	0.07	2.45	2.39
03	0.09	3.17	3.14
04	0.11	3.90	3.90
05	0.13	4.62	4.65
06	0.16	5.35	5.30
07	0.18	6.07	6.03
08	0.20	6.80	6.79
09	0.22	7.52	7.54
10	0.24	8.25	8.30
11	0.26	9.01	8.93
12	0.28	9.73	9.80
13	0.30	10.46	10.56
14	0.32	11.18	11.31
15	0.35	11.90	11.94
16	0.37	12.63	12.70
17	0.39	13.35	13.43
18	0.41	14.08	14.08
19	0.43	14.80	14.83
20	0.45	15.53	15.59

Source: The Author (2019).

In order to sum up the experiment information, Table 5 shows the main characteristics of the experiment described in the section.

Table 5 – Main information of the experiment.

Reynolds (Re)	1065 - 9488 Equation (2.1)
Reduced Velocity (Vr)	1.75 - 15.59 Equation (3.3)
Number Velocities	20
Number of Targets	18
Acquisition Frequency	$100Hz$
Monitoring Time	$350s$
Boundaries Conditions	Pinned-pinned

Source: The Author (2019).

3.3 Analysis

In this subsection, it is shown to the reader insights of the analyses applied in the result section. Once again, few results are shown in this part; however, they are only displayed to help the reader to understand the analysis procedure.

3.3.1 Modal Projection

The modal projection aims to distinguish the amplitude contribution of each natural mode in the total amplitude multi-modal dynamic response. This method implies the vibration modes orthogonality which is assumed for this work.

In a simple way, the modal projection allows writing the experimental dynamic response as an overlap of modal contributions. A modal decomposition based on Galerkin's method was applied. This decomposition enables the frequency and amplitude responses of each mode. Therefore, this work considered up to the 10th vibration mode, 5 on the cross-flow plane and 5 on the in-flow plane.

The modal amplitude response is defined by Equation (3.6).

$$Am_i(t) = \int_0^L \frac{< \mathcal{M}_n(s), q_e(s,t) >}{\parallel \mathcal{M}_n(s) \parallel} \tag{3.6}$$

Where q_e is the experiment amplitude response at time t and $\mathcal{M}_n$ the eigenvectors of mode i. The eigenvectors were computationally obtained using the Anflex[1] software.

An example of the modal decomposition is shown in Figure 22. Several features are exposed. First, the subplot on the left shows the non-dimensional amplitude of $Am_i(t)/D$ for each natural mode. This information indicates what modes are being excited and their contribution to the total amplitude. In this case, it can be visually seen that $\mathcal{M}_2$ and $\mathcal{M}_4$ have the most significant values. This is a powerful analysis,

[1] Anflex is PETROBRAS' in-house software developed for static and dynamic analysis of free vibration on risers and mooring lines. The software was developed by PETROBRAS Research Center (CENPES) and Federal University of Rio de Janeiro (UFRJ). It uses the Finite Element Method (FEM)

once the modal projection could revel shift between modes during the experiment as well modulation on the signal in time. Second, the subplot in the right is the Fourier transform of the non-dimensional amplitudes. The vertical lines are the numerical natural frequencies of the flexible cylinder. This subplot also has essential information. For instance, $Am_2(t)/D$ is vibrating near to the frequency of f_{n2}, and $Am_4(t)/D$ a much lower spectrum peak near to f_{n4}.

The type of analysis showed in Figure 22 revel what frequency the modal contributions are vibrating. It is important to highlight that this figure is for the $Vr = 6.03$. Therefore, each reduced velocity was analyzed by plotting this type of graph, which supported the results in the Chapter 4

Figure 22 – Modal decomposition in $Vr = 6.03$ and $Re = 3670$. The figure on the left shows the non-dimensional amplitude $Am_i(t)/D$. The figure on the right shows the frequency spectrum of $Am_i(t)$ normalized by the maximum spectrum value of all modes. Vertical lines are the numerical frequencies obtained through the Anflex software.

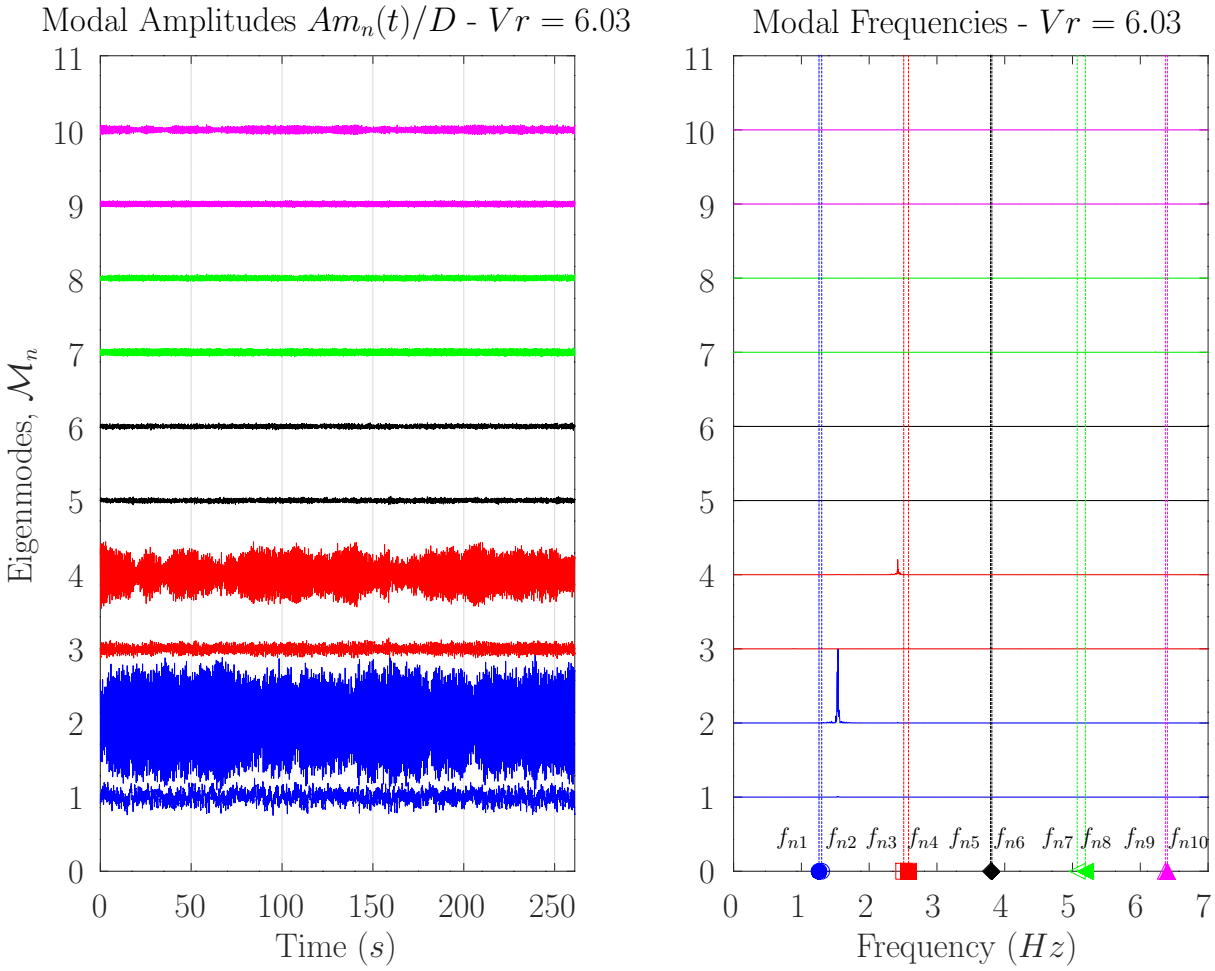

Source: The Author (2019).

Further, another advantage of this method is the reconstruction of the total

amplitude using the Equation (3.7), where N_m is the total number of modes considered.

$$a = \sum_{i=1}^{N_m} Am_i(t)\mathcal{M}_i(s) \tag{3.7}$$

The Figure 23 shows the recomposition after the modal projection for the time $t = 100\ s$. The dashed line is the reconstruction using Equation (3.7), and the black circles are the experimental results. The recomposition has a couple of advantages. First, it is possible to recompose not only the portion of the flexible model monitored, but also the portion not tracked, as shown by the dashed line in the Figure 23. Second, the whole flexible cylinder position may be recomposed for any experiment time.

Figure 23 – Reconstruction of the flexible cylinder position in $Vr = 6.03$, $Re = 3670$ and $t = 100\ s$.

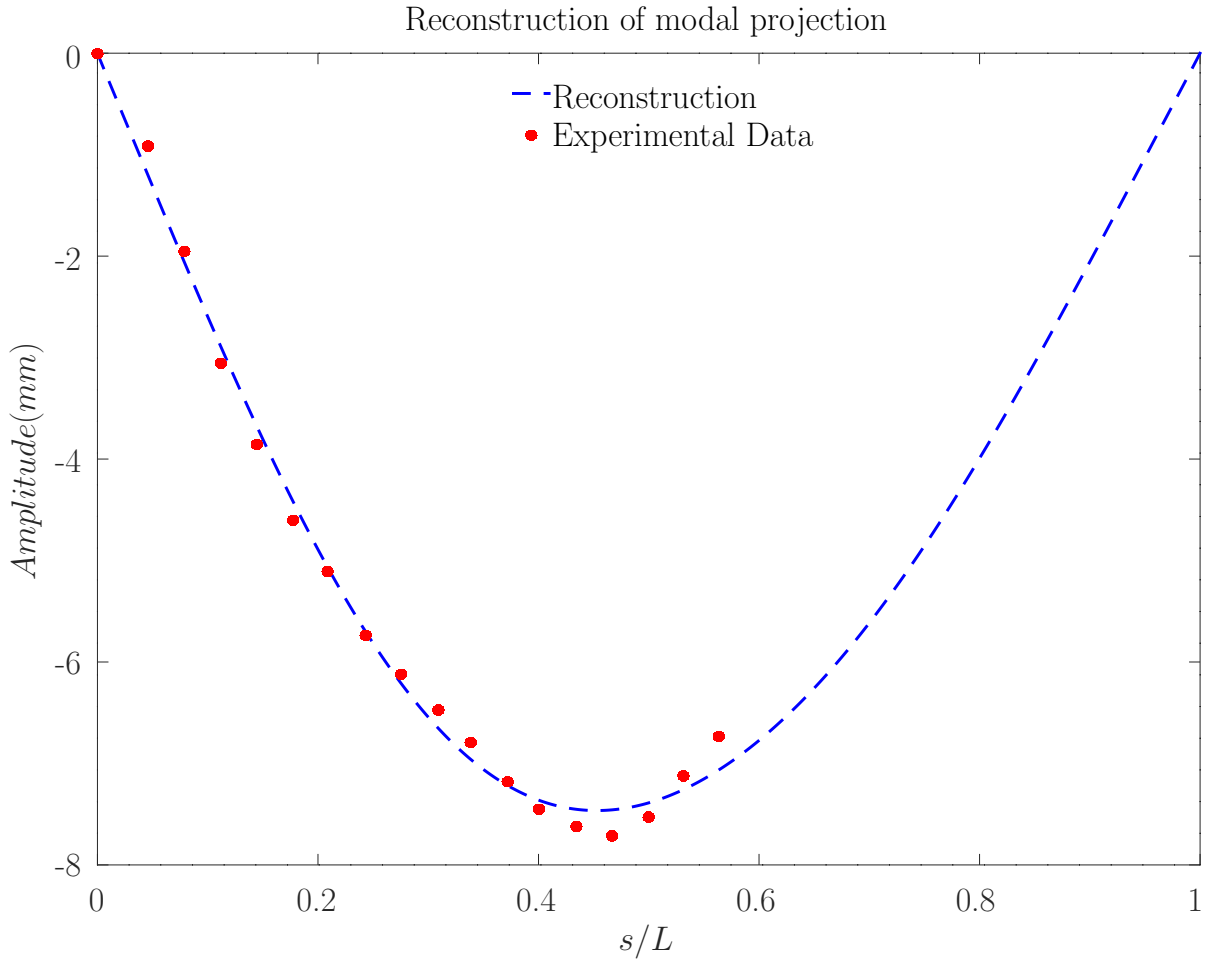

Source: The Author (2019).

3.3.2 Hilbert-Huang Transform

The Hilbert-Huang Transform (HHT) was developed by Huang et al. (1998) and it is a technique for non-stationary signals from non-linear systems, such as the VIV

phenomenon. The technique consists of applying the Empirical Mode Decomposition (EMD) finding a set of Intrinsic Mode Functions (IMF) and proceed with a Hilbert Transform to each IMF. In this work, the code available on Matlab2019a was used.

The EMD recursively decomposes the signal into orthogonal components. Once the IMF is found, the result is subtracted from the original data, and the process restarts until the last IMF. The first IMF has the highest frequency. Therefore, the signal can be written in function of the IMFs, as shown in Equation (3.8).

$$X(t) = \sum_{j=1}^{n} IMF_j(t) + R_n \tag{3.8}$$

Where $X(t)$ is the signal, n is the number of IMF and R_n is the residual value.

The analytical function $Z_j(t)$ is written as Equation (3.9), where $Y_j(t)$ is the Hilbert Transform of $X(t)$, defined in Equation (3.10).

$$Z_j(t) = X_j(t) + iY_j(t) = a_j(t)e^{i\theta_j(t)} \tag{3.9}$$

$$Y_j(t) = \frac{1}{\pi} P \int_{-\infty}^{+\infty} \frac{X_j(\tau)}{t-\tau} d\tau \tag{3.10}$$

Then, a Hilbert Transform is applied to each IMF, and $X(t)$ can be expressed as Equation (3.11), where Re stands for the real part.

$$X(t) = Re\left(\sum_{j=1}^{n} a_j(t)e^{i\int \omega_j(t)dt}\right) \tag{3.11}$$

$$\omega_j(t) = \frac{d}{dt}[\theta_j(t)] \tag{3.12}$$

Therefore, the amplitude a_j and the frequency $\omega_j(t)$ are time dependent for each IMF. The representation of the instantaneous frequency and amplitude in function of time is named the Hilbert Spectrum $H(\omega, t)$. The marginal spectrum, which represents the energy contribution of each frequency is defined in Equation (3.13).

$$h(\omega) = \int_0^T H(\omega, t)dt \tag{3.13}$$

An example of the IMFs obtained is shown in Figure 24. The IMFs have physical meaning. They are frequency components within the original signal with their respective amplitudes. In the example of this work, the IMF2 in close to the original signal, and the other IMFs are not significant. Therefore, it is implied that the VIV is the only source of energy in the system, because the signal is reconstructed mainly with one IMF. However, if other sources inputting an oscillatory force were acting in the experiment, more IMFs would have significant oscillations.

Another view of the method is that the EMD is a dyadic filter, which separates the original signal in multiple components, each with a single frequency sub-band.

Figure 24 – Intrinsic Mode Function for $Vr = 6.03$, $Re = 3670$ at $s/L = 0.25$. First figure is the experimental data for $s/L = 0.25$. Graphs 2 to 11 are the IMFs. The figure in the bottom is the residual value.

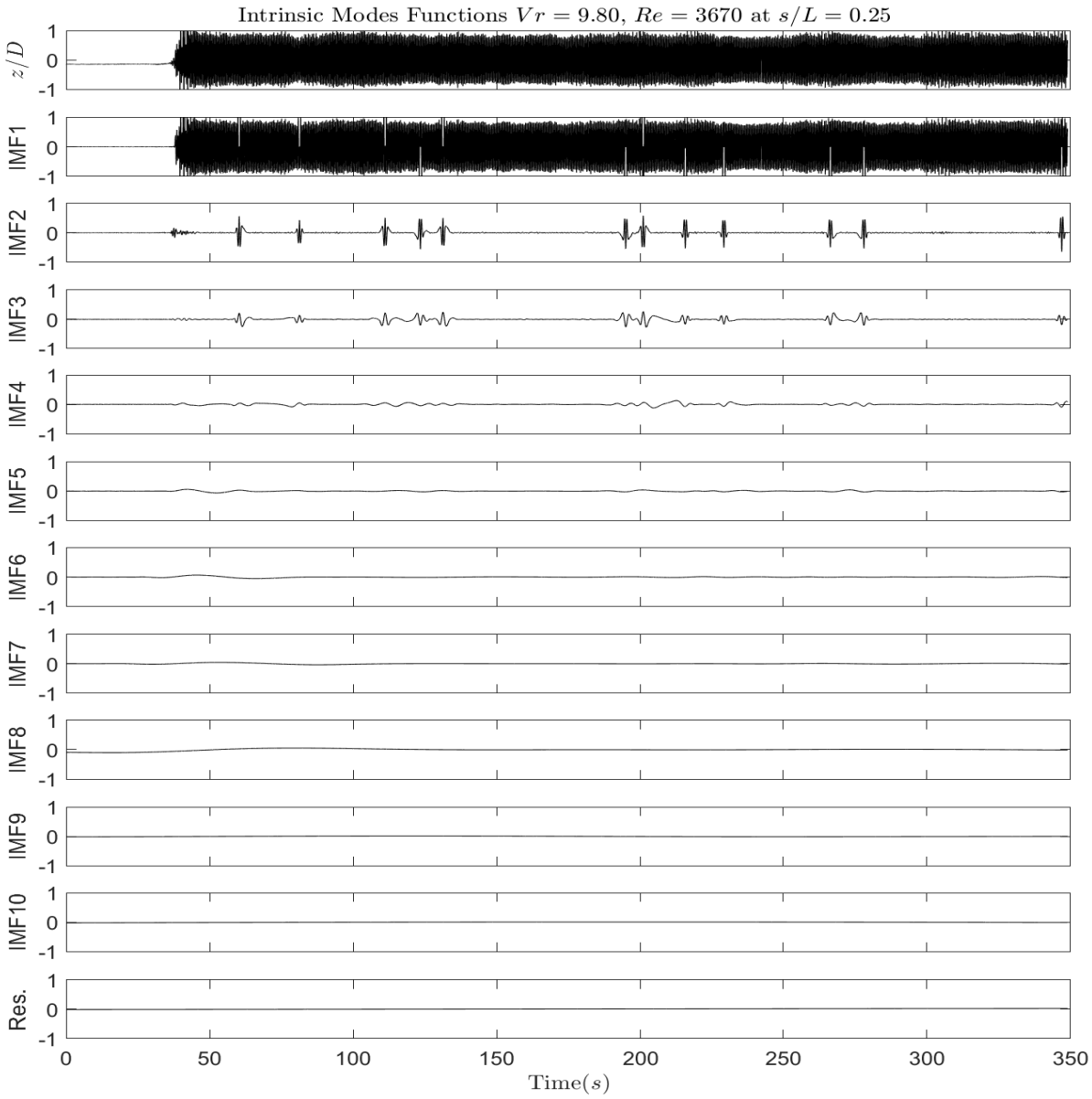

Source: The Author (2019).

3.3.3 Relative Phase Angle and Trajectories

The trajectories and phase angle are essential features of VIV. This type of analysis intends to find trajectories and phase angles of the modes excited during the experiment. In this work, the relative phase angle was calculated according to Pikovsky, Rosenblum and Kurths (2003). The relationship of instantaneous frequency,

as described in Equation (3.12), can be defined for in-line and cross-flow direction. In addition, the relative phase angle is found by Equation (3.14). The constants n and m are defined by the frequency relation in Equation (3.15). Therefore, according to Equation (3.14) the relative phase angle is the phase angle of the cross-flow oscillation minus the phase angle of the in-line oscillations.

$$\phi_{z,x}(s/L_i, t) = m\phi_z(s/L_i, t) - n\phi_x(s/L_i, t) \tag{3.14}$$

$$\frac{\omega_x(s/L_i, t)}{\omega_z(s/L_i, t)} = \frac{n}{m} \tag{3.15}$$

This method stands when $\phi_{z,x}$ is constant in time there is coherence between motions (in-line and cross-flow). However, due to high scatter on the data, a statistical analysis is more reliable. In this work, the statistical analysis applied was based on a cyclic phase difference, according to Equation (3.16), which exposes the angle from 0 to $360°$.

$$\psi_{z,x}(s/L_i, t) = \frac{180}{\pi}[\phi_{z,x} mod(2\pi)] \tag{3.16}$$

Because the values of $\psi_{z,x}$ brings the relative phase angle values as a function of time, a histogram with the Probability Density Function (PDF) was built. These PDF plots frequently exhibited a normal type of distribution. In these cases, a normal distribution was fitted on the data, according to the Equation (3.17). Roughly, the data which have shown a normal distribution type means that there is coherence between motions (in-line and cross-flow).

$$\theta_{z,x}(s/L_i, t) = \frac{1}{\sigma\sqrt{2\pi}} e^{\frac{1}{2\sigma^2} - (\psi(s/L_i, t) - \mu)^2} \tag{3.17}$$

The variable μ is the mean value and σ the standard deviation.

An example of the analysis is found in Figure 25. The analysis shows coherence of the model and a typical trajectory motion. A unique relative phase relative angle for the targets $s/L < 0.5$ was found, only for $s/L = 0.5$ the relative phase angle jumps between $287°$ and $72°$, which are the same angle but different direction ($\pm 72°$). In this case, two normal distribution was fitted. The values of σ have an essential meaning on the results. For instance, it indicates how much spread the normal distribution is and, consequently, if the angle is varying too much in time. The targets $s/L < 0.5$ have a small σ compared to the value found for $s/L = 0.5$, which means the angle is sharp and stable in this points. On the other hand, the high σ value for $s/L = 0.5$ is due to the less stable condition because of the alternation between the two angles $\pm 72°$.

Figure 25 – Relative phase angle for $Vr = 6.03$ and $Re = 3670$. First row represents the trajectory from 252 to 272 seconds. Second row are the Relative Phase Angle ψ_{zx} from 110 to 310 seconds. Third row are the Probability Density Function of the relative phase angle. The bottom row represents the medium relative phase angle (μ) and the standard deviation in each target. Gray values are mirrored targets symmetric-assumed.

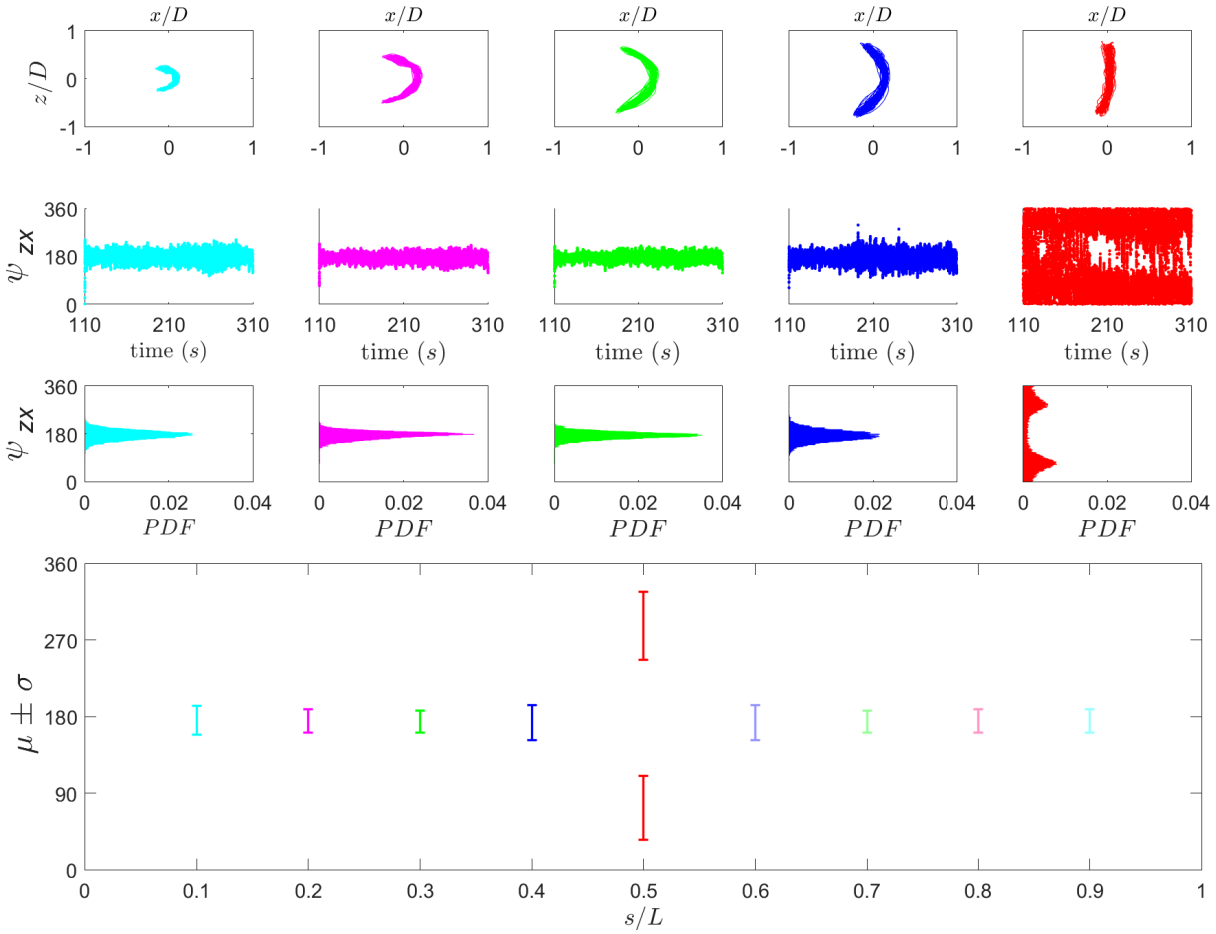

Source: The Author (2019).

In order to sum up the analysis planned, Table 6 shows the main results expected of each analysis.

Table 6 – Main information of each analysis planned.

Type	Characteristic	Objective
Dynamic response	Traditional analysis of amplitude response and frequency using the Fourier transform as a function of Vr.	Visualization of lock-in ranges and comparisons with other works.
Modal Projection	Decomposition of the response in contributions of vibration modes using the Galerkin's method.	Verify the multi-modal behavior of the structure and map the modes present in the total response.
Hilbert-Huang Transform	Empirical method valid for non-stationary signals from non-linear systems.	Compare with the results of the Fourier transform and search for jumps between modes in the frequency domain.
Relative phase angle and trajectories	Calculate the relative phase angle (phase of cross-flow response minus the in-line response).	Verify the relation between the relative phase angle, trajectory type and the mode excited.

Source: The Author (2019).

4 RESULTS

The results presented in this section are amplitude, frequency, relative phase angle, and trajectory analysis of the VIV dynamic response. Each analysis followed the procedure exposed in the Sections 3.3.1 to 3.3.3. The last section of this chapter compares the main results of this work with the literature.

4.1 Dynamic Response

The first analysis is the r.m.s amplitude ($A^{r.m.s.}$) and frequency f/f_{n2} response in each reduced velocity.

First, Figure 26 shows the results for the cross-flow direction ($z-direction$). In this figure, three graphs are available. The graph on the top shows the non-dimensional r.m.s amplitude response (see Equation (3.4)) as a function of the Reduced Velocity (Vr), in which the colors mark the lock-in of the mode ($\mathcal{M}$). The graph on the middle presents the frequency ratio of the dominant excitation frequency f_z^d and the natural frequency of $\mathcal{M}_2$, nominated f_{n2}. The dashed line corresponds to a Strouhal number of 0.16. The graph on the bottom shows a color map where the color is the ($A_z^{r.m.s.}/D$), the $y-axis$ is the curvilinear position of the flexible cylinder ($s/L = 0$ and 1 are the ends) and $x-axis$ is the Vr.

Analyzing the cross-flow response, Figure 26, it is observed four distinct regions. The first, until $1.75 < Vr < 4.65$ (gray squares), it is not observed significant amplitude, and the frequency ratio relies on the line of $St = 0.16$. The second, between $4.65 < Vr < 8.30$ (blue squares), presents significant amplitude. The frequency ratio differs more from the line $St = 0.16$, and the value is around one in all range. On the colormap, it is possible to see the shape of $\mathcal{M}_2$ with one peak in the middle of the flexible cylinder, $s/L = 0.5$. The third region, between $8.30 < Vr < 14.30$ (red squares), the amplitude increase, and the frequency ratio jump to around 1.6. The colormap shows evidence of the mode shape $\mathcal{M}_4$, with two peaks and three nodes. Finally, the fourth region, between $14.30 < Vr < 15.60$ (black squares), shows a frequency ratio around 2.5 and the color map shows the mode shape $\mathcal{M}_6$ with three peaks and four nodes.

The same type of result is presented for the in-line direction ($x-direction$), as shown in Figure 27. Until $Vr \approx 4.65$ three modes are successively locked, they are $\mathcal{M}_1$, $\mathcal{M}_3$ and $\mathcal{M}_5$. Although the small amplitude response, it is possible to see distinctive steps in the frequency ratio graph and the mode shapes on the colormap. However,

Figure 26 – Cross-flow amplitude (r.m.s) and frequency responses due to vortex-shedding excitation versus the reduced velocity.

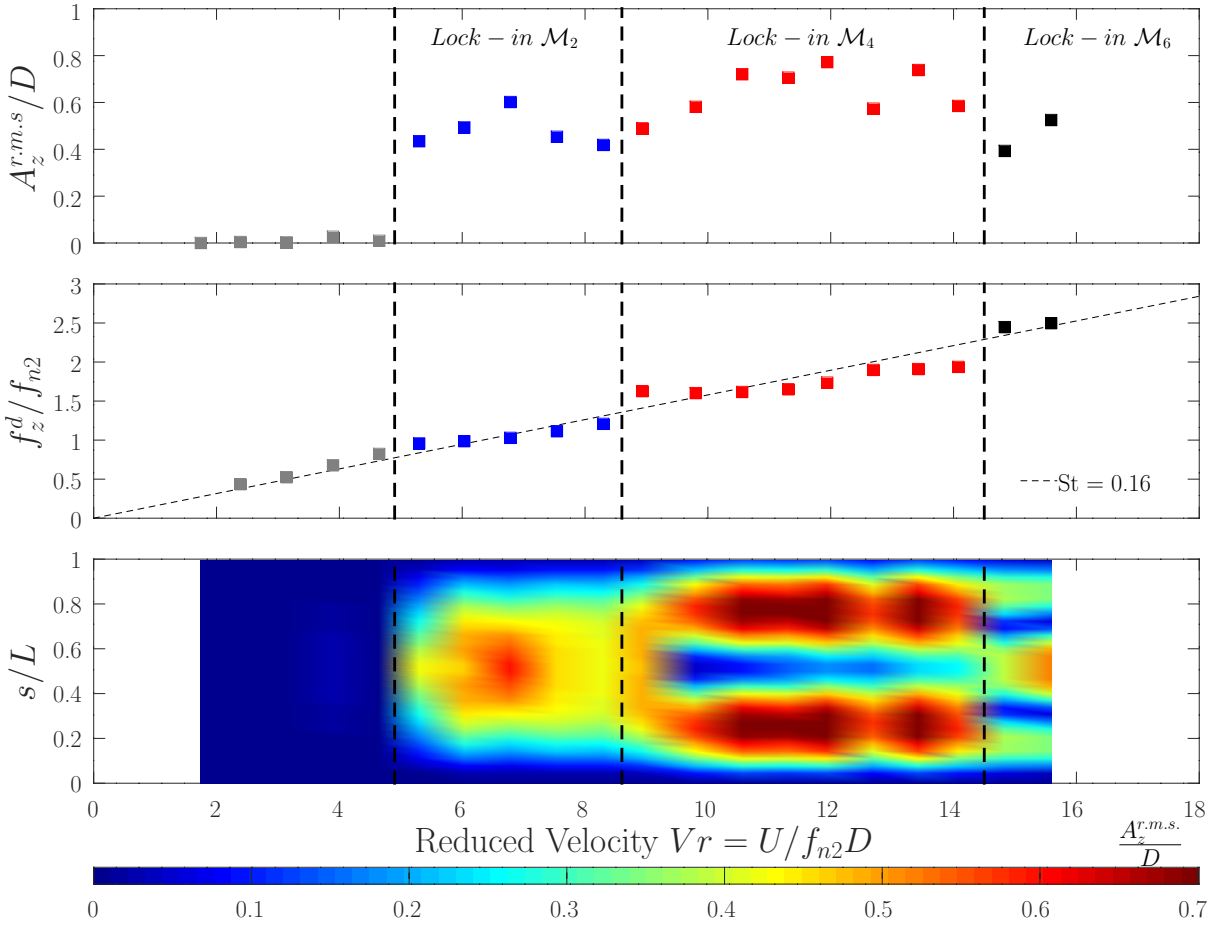

Source: The Author (2019).

instead of the next lock-in be the $\mathcal{M}_7$, the mode excited is $\mathcal{M}_3$, and the frequency ratio stays around 2. This happens because of the lock-in of the cross-flow mode $\mathcal{M}_2$, which changes the in-line dynamics breaking the ascending order. During the transition between the cross-flow modes from $\mathcal{M}_2$ to $\mathcal{M}_4$, which is around $7.5 < Vr < 8.5$, the in-line frequency jumps to around 5. When the cross-flow mode $\mathcal{M}_4$ is well established, the in-line frequency ratio returns to 3, and the mode $\mathcal{M}_5$ is locked. For velocities higher than that, the modes $\mathcal{M}_7$ and $\mathcal{M}_9$ are synchronized, with distinctive steps in the frequency and amplitude response. This feature demonstrates the impact of modal response between vibration planes, where the lock-in of cross-flow modes impact the in-flow dynamics. Overall, the in-line frequency relies near to $St = 0.32$ when the cross-flow modes are locked. These values of Strouhal number, $St = 0.16$ for cross-flow and 0.32 for in-line were also reported by Huera-Huarte and Bearman (2009a).

The $\mathcal{M}_2$ lock-in present a maximum r.m.s amplitude value of $A_z^{r.m.s.}/D = 0.60$ at $Vr = 6.79$. In the same range but for the in-line response, the maximum amplitude

Figure 27 – In-line amplitude (r.m.s) and frequency responses due to vortex-shedding excitation versus the reduced velocity.

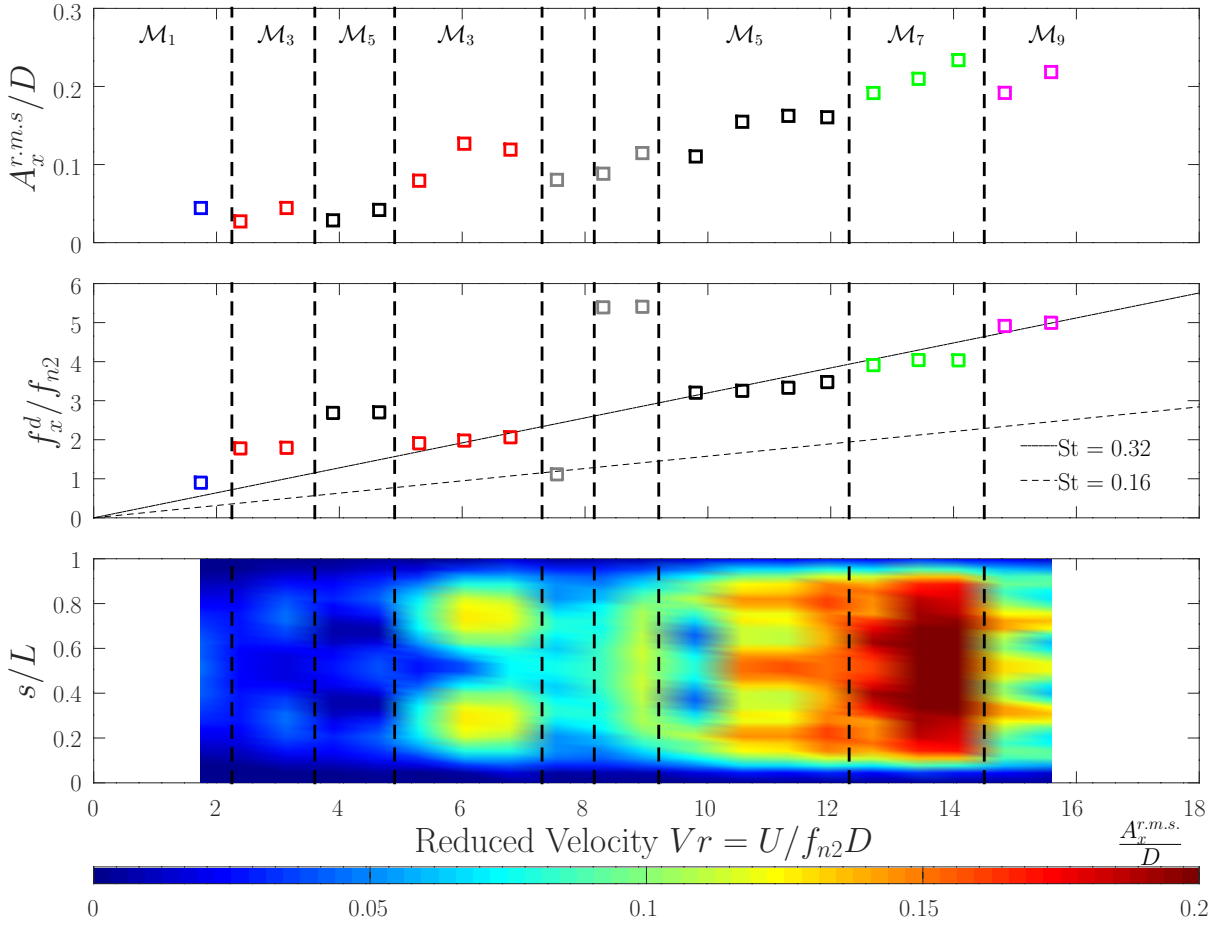

Source: The Author (2019).

is $A_x^{r.m.s.}/D = 0.13$ at $Vr = 6.03$. The $\mathcal{M}_4$ lock-in, $A_z^{r.m.s.}/D = 0.77$ at $Vr = 11.94$, and $A_x^{r.m.s.}/D = 0.23$ at $Vr = 14.08$. Unfortunately, only two reduced velocities are inside the $\mathcal{M}_6$ lock-in, and the maximum peak cannot be identified. The ratio between cross-flow and in-flow amplitudes are found to be between 4 and 6 in the most of the cases. The same value was reported by Huera-Huarte and Bearman (2009a).

Furthermore, the results have not shown the lower branch and the desynchronization as rigid cylinders (see Section 2.2). Instead, a successive mode synchronization is present.

4.2 Modal Projection

The amplitudes and lock-in range observed in Figures 26 and 27 have shown lack of visual desynchronization between modes. This differs from rigid cylinders, where a successive mode excitation is visually identified with synchronization followed by desynchronization. However, as exposed in Section 2.3, flexible cylinders may exhibit

overlap between modes and a multi-modal behavior. In addition, the high mass-damping factor may be important for the modal response as it is for rigid cylinders, due to the impact on the inertia of the system. Therefore, it is important to know the modes present in the response and associate their correct damping, instead a unique value of damping. Further, because of the reports of multi-modal behavior on flexible structures, the modal projection may unveil an unusual behavior of the system response.

In order to investigate the modal contribution on the total amplitude, a modal projection using the 10 first eigenmodes was applied, 5 in-line and 5 cross-flow. The modal base, shown in Figure 28, is obtained using the finite element code of the Anflex software, as exposed in Section 3.3.1. The results are shown in Figures 29 and 30, for amplitude and frequency respectively.

Figure 28 – Eigenmode base used for the modal projection analysis.

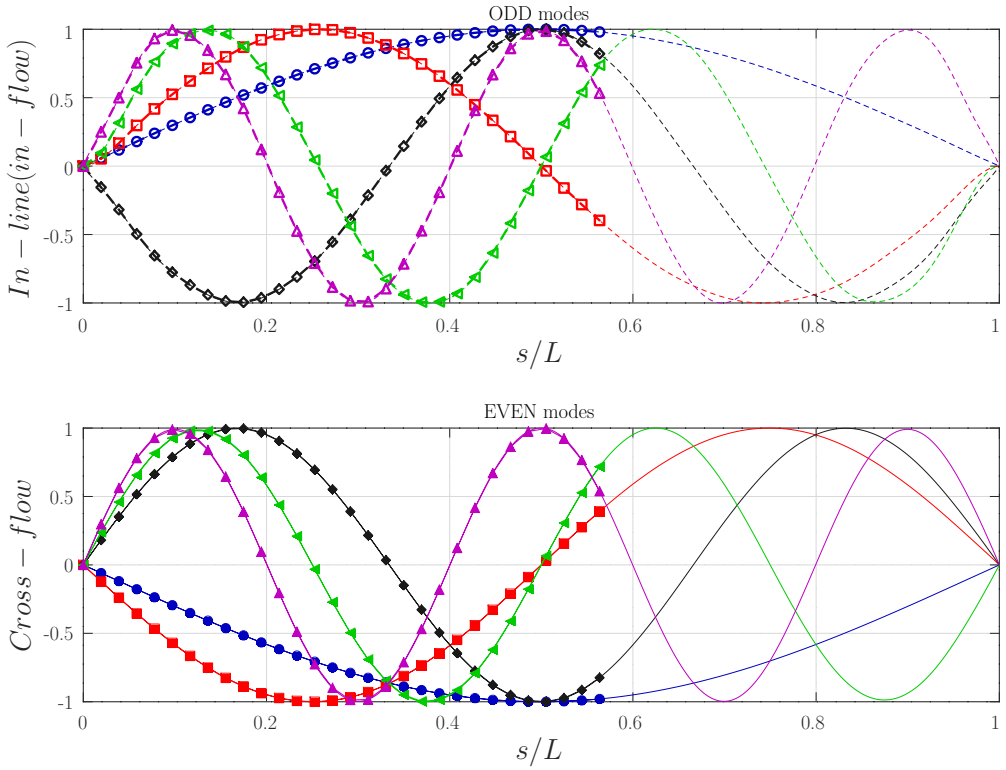

Source: The Author (2019).

The modal projection amplitude, in Figure 29, confirm a modal contribution up to the 8th mode on the total response. The $\mathcal{M}_2$ lock-in has a higher value for $\mathcal{M}_2$, however near to the desynchronization zone $\mathcal{M}_4$ increases in amplitude. The $\mathcal{M}_4$ lock-in is identified by a sudden drop of modal amplitude $\mathcal{M}_2$ and growth of $\mathcal{M}_4$. This region have modal contribution of $\mathcal{M}_2$, $\mathcal{M}_4$ and $\mathcal{M}_6$. Finally, on the last two reduced velocities, $\mathcal{M}_6$ and $\mathcal{M}_8$ have more significant contributions of the total amplitude, however, as the $\mathcal{M}_6$ lock-in is not completely established, the modal contribution of $\mathcal{M}_6$ is not the

highest. If more velocities were carried out, probably the modal contribution of $\mathcal{M}_6$ would increase.

Figure 29 – Modal r.m.s amplitude responses. The figures present respectively the cross-flow and in-line direction.

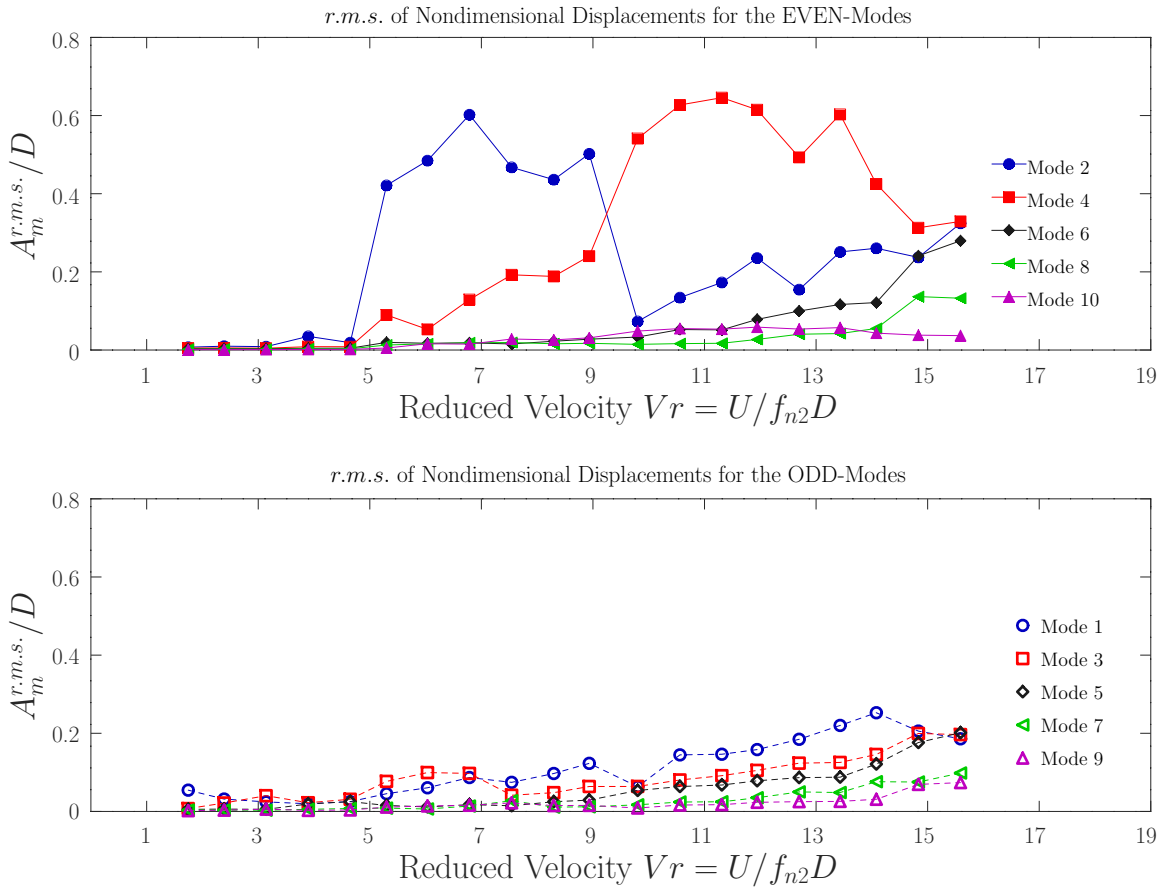

Source: The Author (2019).

Further, in Figure 29, the amplitude response overlaps between modes and the total response is multi-modal. Inside a lock-in region, the amplitude increases steadily, with a drop when the next mode is becoming dominant. This behavior was found by Chaplin et al. (2005b), where the overall response is a combination of two or more modes.

The same analysis may be conducted for the in-line motions. However, the modal contributions are less precise because of lower amplitudes, although the trend should be reproduced.

Figure 30 shows the frequency ratio of the modal response. It illustrates that, as the reduced velocity increases, the frequency ratio advance in distinct steps when the modes are locked. Another interesting information is observed analyzing the modal frequency response, see Figure 30. Although there is the modal contribution of many modes on the total amplitude, the dominant mode frequency is established. For example, inside the first lock-in of the cross-flow plane, there are contributions of $\mathcal{M}_2$ and $\mathcal{M}_4$, and

both modal frequencies are equal $f_{n4} = f_{n2}$. The same happens, inside the lock-in of $\mathcal{M}_4$. There are contributions of $\mathcal{M}_2$, $\mathcal{M}_4$ and $\mathcal{M}_6$, however, they vibrate in the dominant frequency of $\mathcal{M}_4$, $f_{n6} = f_{n2} = f_{n4}$.

Figure 30 – Modal r.m.s frequency ratios. The figures present respectively the cross-flow and in-line direction.

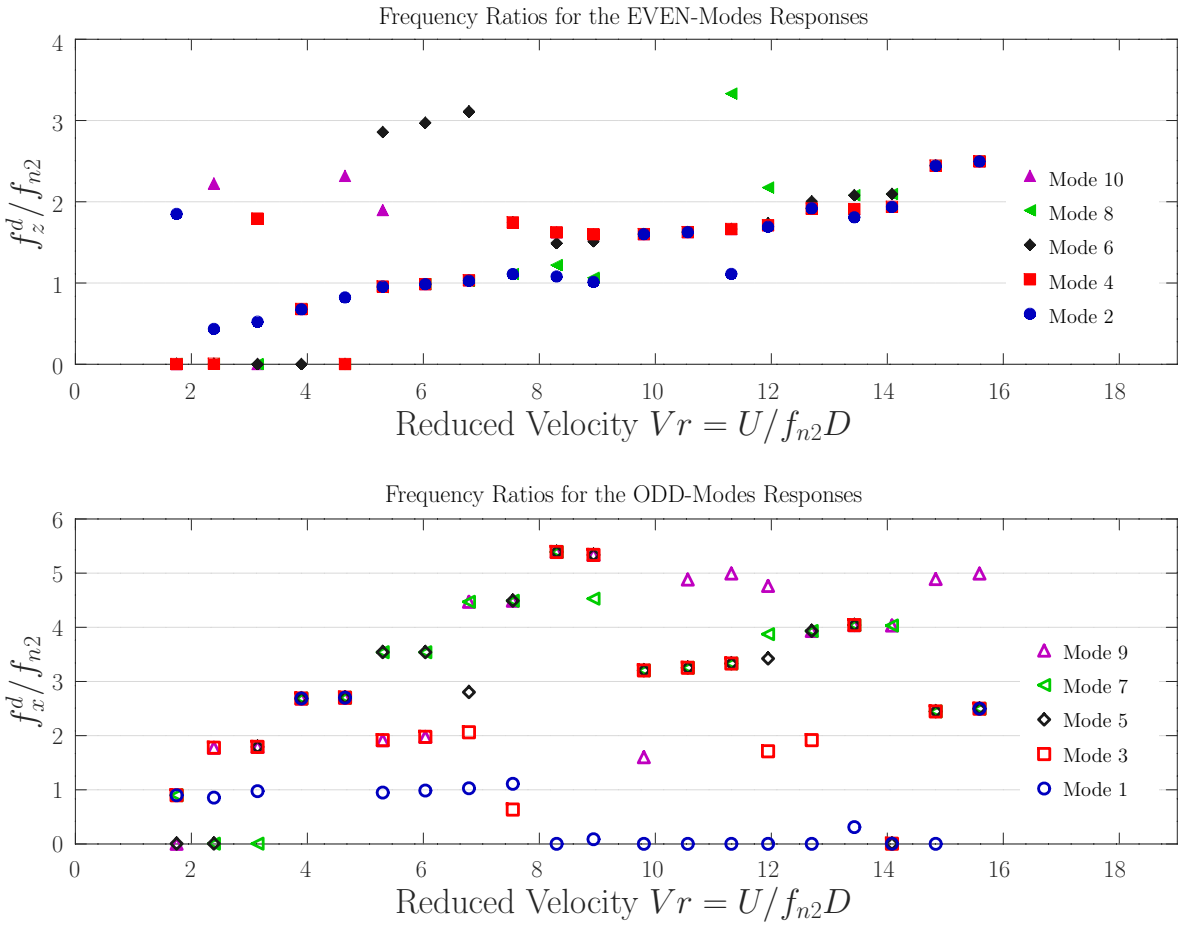

Source: The Author (2019).

4.3 Hilbert-Huang Transform

It is known that the VIV is non-linear and the Fourier analysis may not identify all features regarding the phenomenon. In this context, the Hilbert-Huang transform, which is a non-stationary technique for non-linear systems, is applied for complementary analysis and comparison with the Fourier transform. Figure 31 present the analysis for the Hilbert-Huang transform and Figure 32 for the Fourier transform of the cross-flow vibration plane. The Hilbert-Huang transform and Fourier transform are shown, respectively, in Figure 31 and Figure 32 for cross-flow, and Figure 33 and Figure 34 for in-line vibration plane.

Firstly, the HHT is analyzed for the cross-flow responses. Figure 31 presents the HHT spectrum for several reduced velocities. The Fourier transform is shown in

Figure 31 – Cross-flow Hilbert-Huang Spectrum at $s/L = 0.25$ for $Vr = 6.03$, 7.54, 9.05 and 9.80.

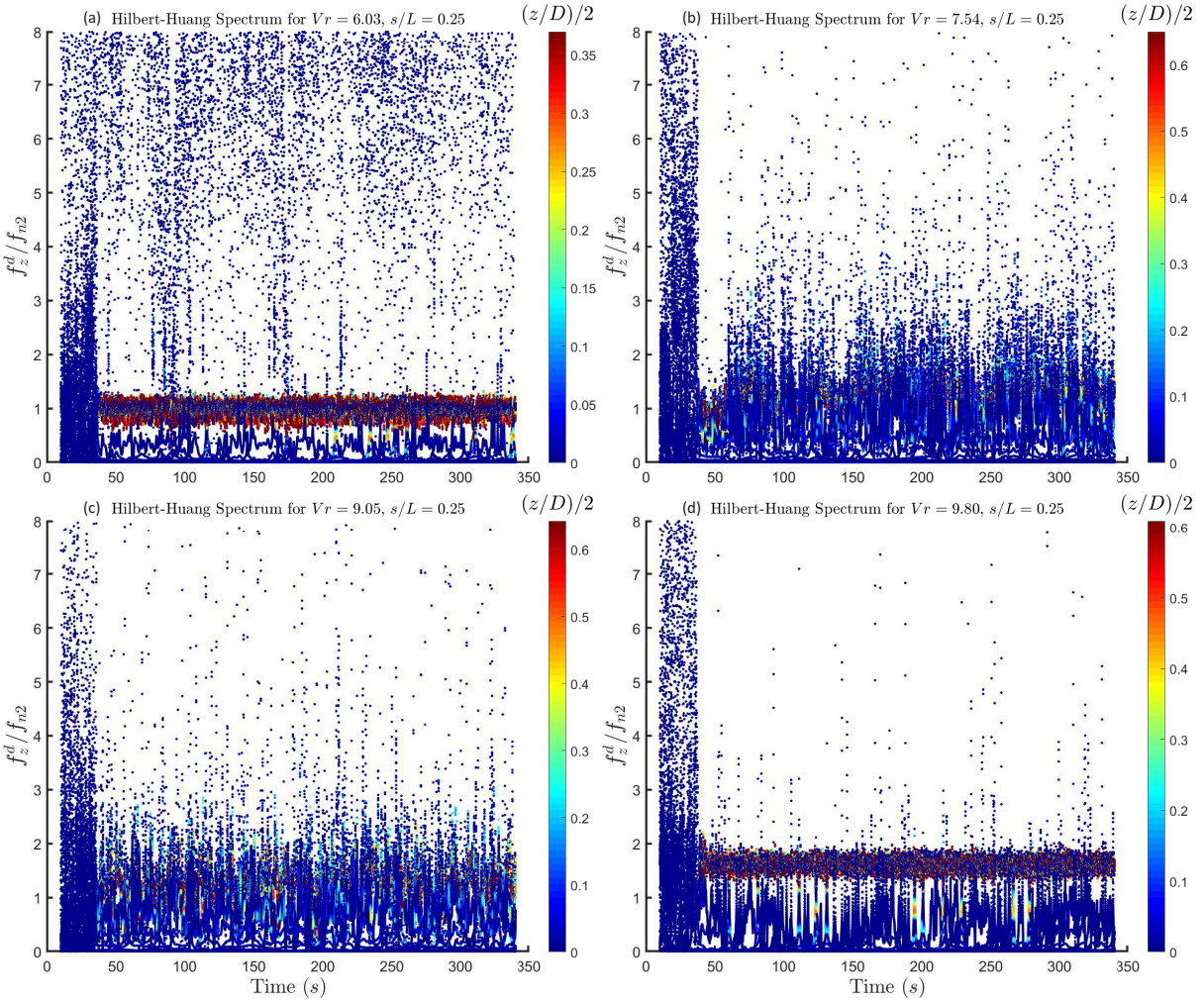

Source: The Author (2019).

Figure 32 for the same point and velocities.

The $Vr = 6.03$, Figure 31 (a), is inside the first lock-in and present modal contribution is mainly of $\mathcal{M}_2$, see Figure 29, however, the spectrum presents a frequency ratio oscillation in time around 1, from 0.7 to 1.3, with several peaks down to 0.3. The mean value corresponds to the Fourier analysis, as shown in Figure 32 (a), which has shown a frequency ratio peak around one.

Increasing the velocity to $Vr = 7.54$ and $Vr = 9.05$, respectively Figure 31 (b) and (c), larger bands of frequency are found. The first ($Vr = 7.54$) is still inside the $\mathcal{M}_2$ lock-in and presents contributions of $\mathcal{M}_2$ and $\mathcal{M}_4$. The HHT reveals a jump around 50 seconds. It seems like the initial part of the run tries to lock on $\mathcal{M}_2$ and jumps into a transition region, where it is hard to find a well define vibration band. At the same point, Figure 32 (b) present the Fourier transform. It is possible to identify two characteristic

Figure 32 – Cross-flow Fourier Transform Spectrum at $s/L = 0.25$ for $Vr = 6.03$, 7.54, 9.05 and 9.80.

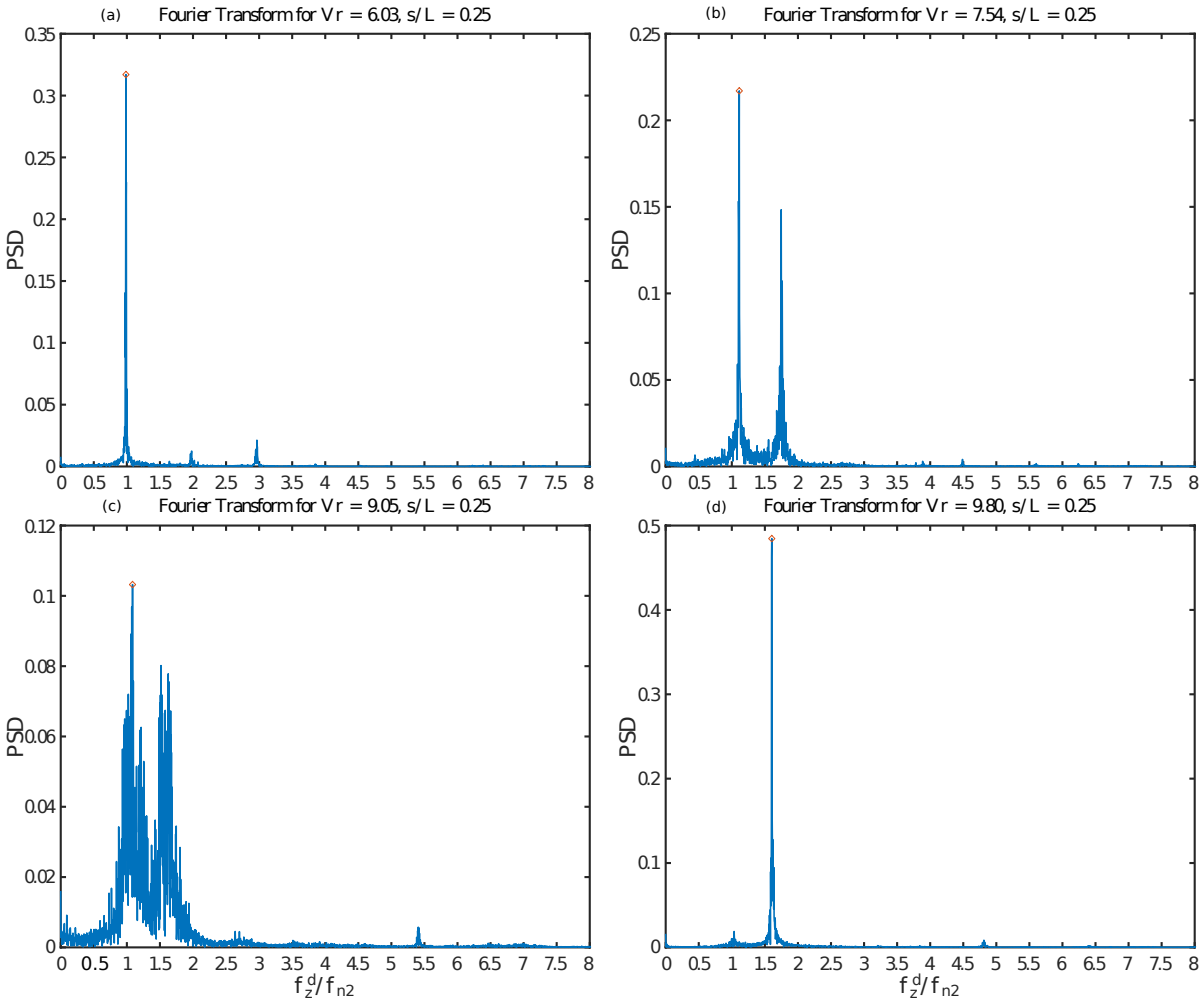

Source: The Author (2019).

frequencies, one around 1.1 and another 1.7. At this point, the Fourier transform seems easier to identify the frequencies in the signal.

The $Vr = 9.05$, Figure 31 (c), presents a little more concentrate energy distribution, and it is on edge between the lock-in change. On the other hand, the Fourier transform, Figure 32 (c), present a spread energy distribution which agrees with the Hilbert-Huang analysis.

After that, $Vr = 9.80$ (Figure 31 (d)) is fully the second mode, as shown in Figure 29, and a similar pattern found for $Vr = 6.03$ is reproduced. A narrower band frequency with high energy oscillating around a frequency ratio of 1.6, from 1.3 to 1.9, with several frequency drops. The same velocity but for the Fourier analysis is shown in Figure 32 (d). The result agrees with the Hilbert-Huang transform and shows a unique peak with a frequency ratio of 1.6.

The Hilber-Huang transform in the cross-flow confirms the Fourier analysis and

brings an idea of band frequency rather than a single value. There were not jumps between modes or more than one response frequency during the analysis.

The Figure 33 and Figure 34 present similar analysis for the in-line motion. Looking at $Vr = 6.03$, Figure 33(a) , there is a range around the frequency ratio of 2 where the energy is concentrated and a lower value around one. Looking at Figure 34 (a), the same peaks are identified. When the velocity increases to 7.54 and 9.05, the Hilbert-Huang analysis turns difficult to read because of the widespread energy. This may be seen in Figure 34 (b)-(c), where a wider band is identified for the Fourier transform. However, the latest is more convenient to identify the peaks of the vibration modes. Finally, at 9.80, the Hilbert Huang, Figure 34 (d), and the Fourier transform, Figure 34 (d), shows the same frequency ratios, around 1.6 and 3.1.

Figure 33 – In-line Hilbert-Huang Spectrum at $s/L = 0.25$ for $Vr = 6.03$, 7.54, 9.05 and 9.80.

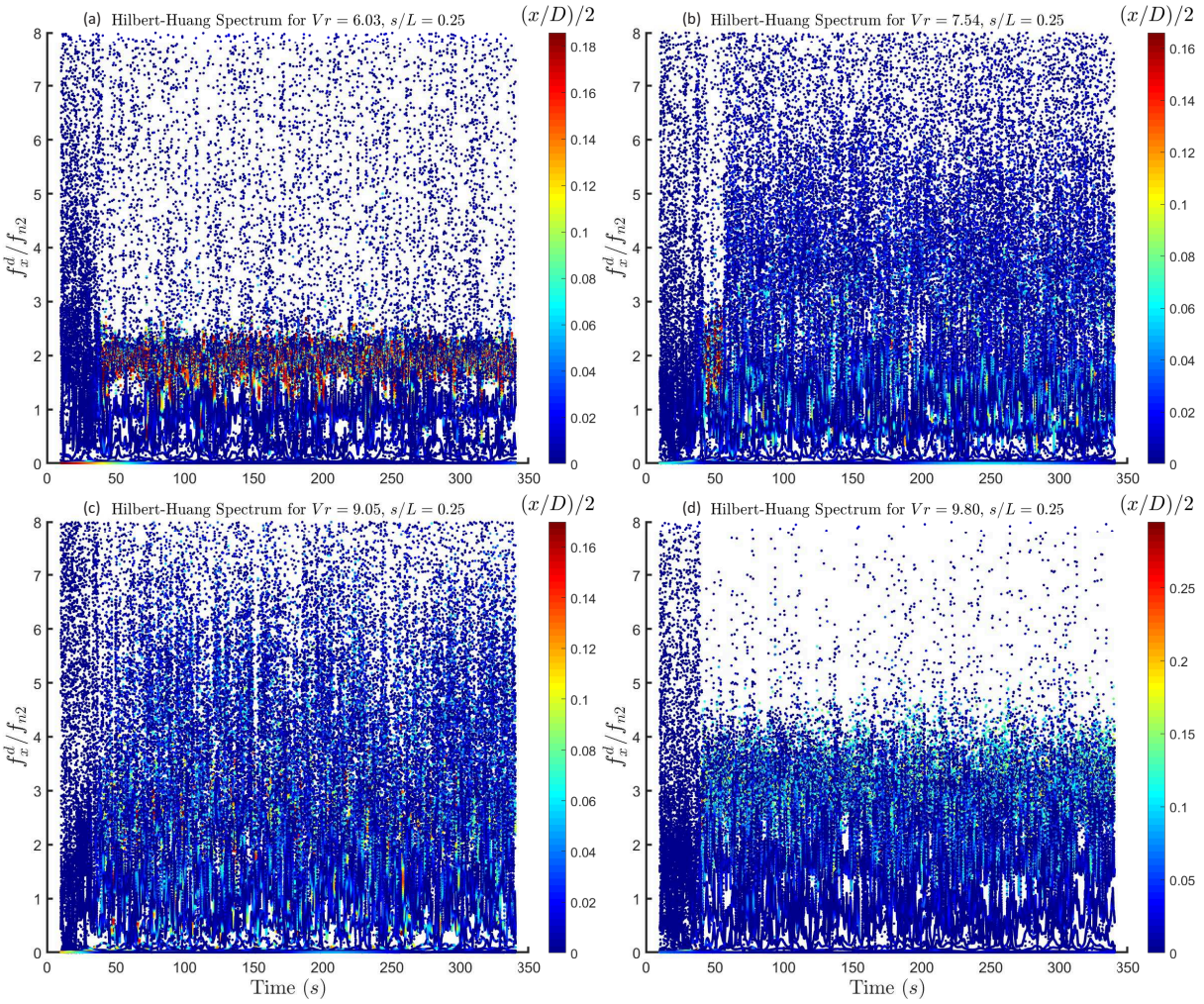

Source: The Author (2019).

The Hilbert-Huang transform showed similar results to the Fourier analysis when, according to the modal projection, one mode is mainly present. On the other hand, for multi-modal responses, the two analysis differ. Furthermore, the advantage of

Figure 34 – Cross-flow Fourier Transform Spectrum at $s/L = 0.25$ for $Vr = 6.03$, 7.54, 9.05 and 9.80.

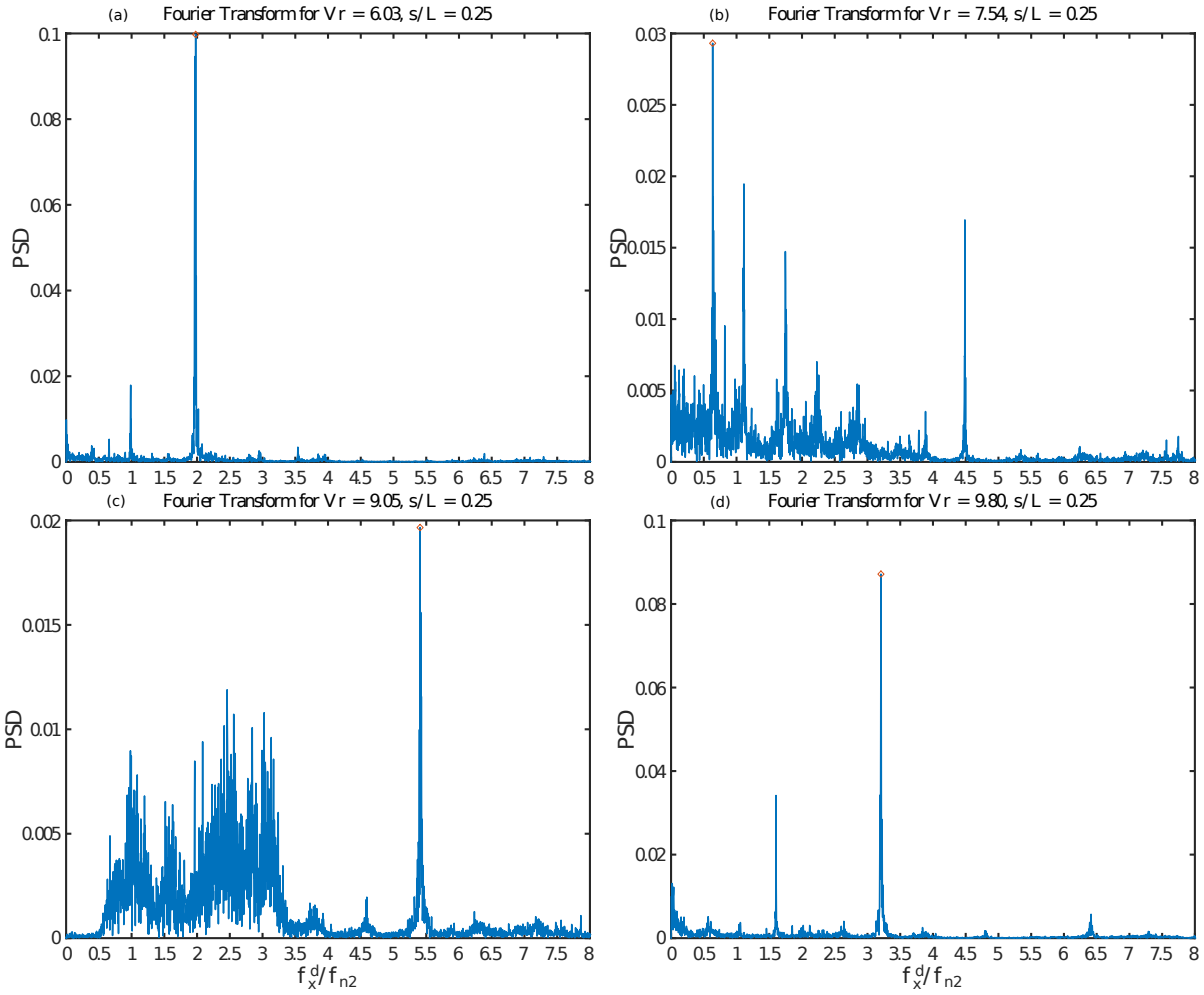

Source: The Author (2019).

using the Hilbert-Huang transform is to obtain the frequency as a function of time. This may be useful if there are modifications of the frequency domain for any reason.

4.4 Trajectory Responses and Relative Phase Angle

The trajectory and relative phase angle evaluate the characteristics of the coupled motions. In this case, the relative phase angle (Equation (3.14)) is the phase angle of the cross-flow motions minus the phase angle of the in-line motions. As explained in Section 3.3.3, the angle is displayed as a Portability Density Function (PDF) where the best normal distribution was fitted in all velocities that have showed a normal distribution type, and the mean angle value μ and the standard deviation σ were taken. Some cases have presented a constant distribution (all angles), and therefore the result was considered. In order to review the analysis, see Section 3.3.3.

Figure 35 compiles the results found for the mean relative phase angle (μ) and the standard deviation (σ) for the cases considered.

Several features can be identified using Figure 35. Looking at $Vr = 5.30$, an eight shape is identified curved to the opposite in-line orientation and θ_{zx} around $338°$. When the reduced velocity increases to $Vr = 6.03$, the shape changes to the in-flow orientation and θ_{zx} also changes to about $174°$. An interesting event happens at $s/L = 0.5$, which corresponds to the higher amplitudes. Two angles are present, $\theta = 73°$ and $286°$ and the trajectory shape less curved. The θ_{zx} in time do not present two branches, see Figure 25, instead of the angle constantly change between these two angles.

Increasing the velocity to $Vr = 6.79$, 7.54, 8.30 and 9.05, the high angle θ_{zx} occurs. The trajectory is present as almost straight and sometimes curved. As presented in $Vr = 6.03$, the first target in $Vr = 9.05$ have a low relative angle.

The first target for $Vr = 9.05$ have a low angle as present in $Vr = 6.03$. Further, looking at Figure 35, velocities higher than 9.05 are related to $\mathcal{M}_4$. Suddenly, when this mode occurs, the angle also changes to lower values. Interesting, near to the higher amplitude targets two angles are established, around $\theta_{zx} = 100°$ and $261°$ for $Vr = 9.80$, and 10.56. Higher values of angles are placed and the low values disappear when the velocity increases to $Vr = 11.31$, which corresponds to the highest amplitude values found. After that, the high angles values are step by step established for the other targets until $Vr = 12.70$. This step by step angle change may happen because the curvature of the line, where the real reduced velocity is lower near to the connection point.

Jumping to $\mathcal{M}_6$, the reduced velocities 14.83 present angles about $\theta_{zx} = 27°$ but with high standard deviation. For $Vr = 15.59$, the relative angles increases and the standard deviation decreases, mainly near the peaks. These trajectory shapes are a well defined eight shape.

Recovering the maps of θ_{zx} during the experiment, a jump between two different angles was found, as shown in Figure 36. During the time 140 to $190s$ and in the final of experiment a different angle is established for $s/L = 0.1$, 0.2, 0.3, and 0.4. The difference between the two angles is clearly shown on the trajectory response, in the last three graphs of the sixth column in Figure 36. When the angle is around $180°$, the tips of the trajectory is curved to the in-flow orientation, otherwise, contrary to the in-flow orientation. This feature was found only on this reduced velocity.

The results found in this analysis shows a high relative angle when the lock-in happens. Some targets have shown lower angle values which may be associated with the deflection of the model. The results found by Huera-Huarte and Bearman (2009a) in the initial branch, considering the middle of the model, was $90°$ increasing to $135°$ and decreasing to $45°$ in the desynchronization range.

Figure 35 – Map of the trajectories for $s/L = 0.1,\ 0.2,\ 0.3,\ 0.4$, and 0.5 according to the reduced velocity from 240 to 250 seconds. Each trajectory corresponds to a mean relative phase angle μ and the standard deviation σ of the normal distribution on its left side. Dashed lines represent the lock-in range if in-line modes and the background colors the cross-flow lock-in ranges.

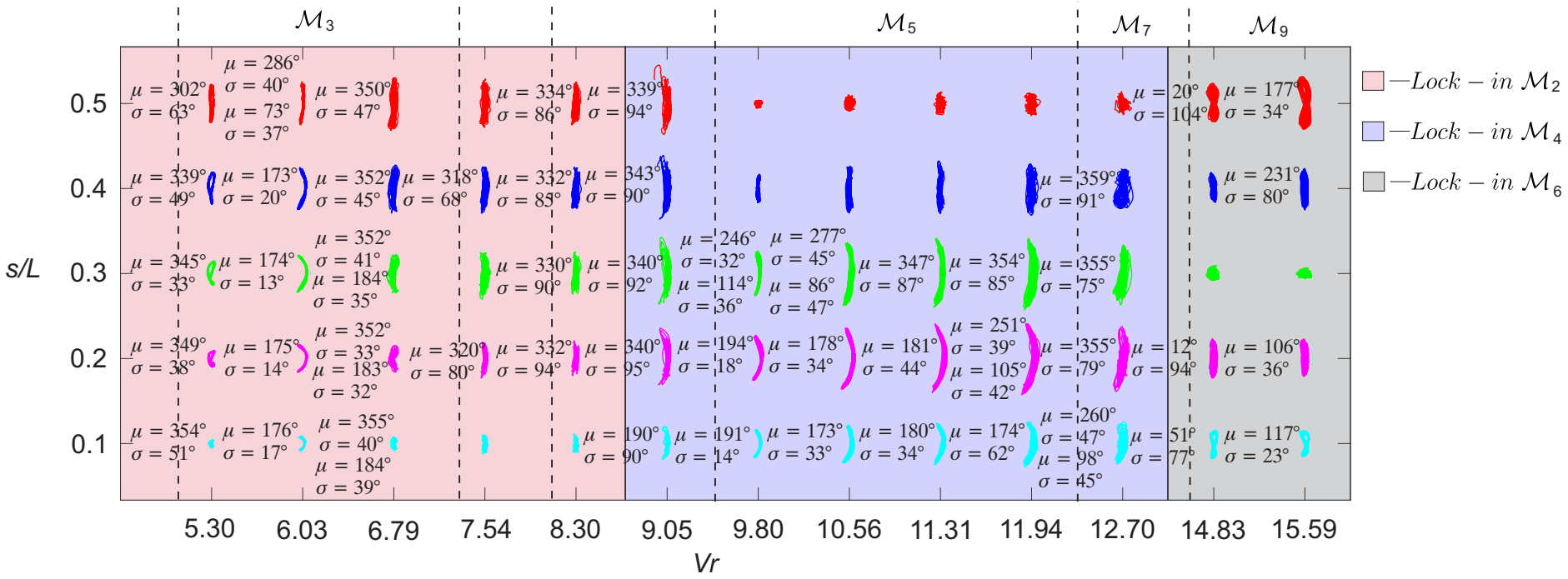

Source: The Author (2019).

Figure 36 – Relative phase angle θ_{zx} for $Vr = 6.79$ and $Re = 4132$. First 4 column represents the model length s/L. First line are the θ_{zx} from 110 to 310 seconds. Third, fourth and fifth line are the PDF of the respectively time 110 to 330, 140 to 190, 190 to 290 seconds. Last column are time range correspondent trajectories for $s/L = 0.2$.

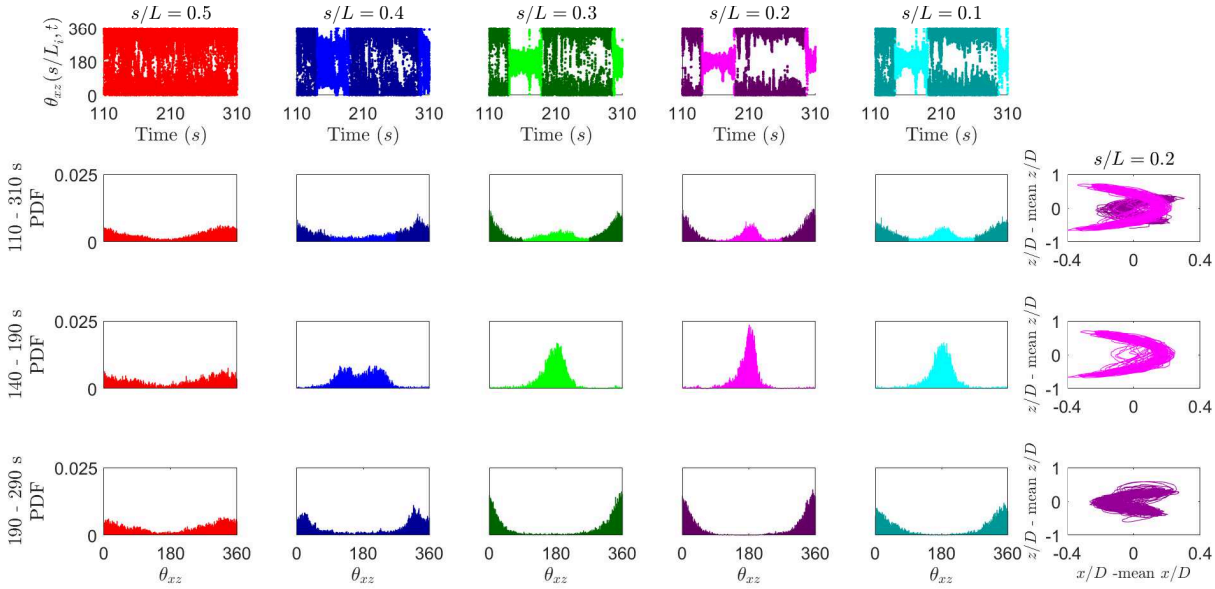

Source: The Author (2019).

4.5 Final Remarks

The amplitude response is compared to data found in literature, trying to understand the behavior of flexible cylinders and the relation with rigid cylinders. The amplitude comparison is shown in Figure 37.

The flexible cylinder experiments are closer to the present experiment, such Huera-Huarte (2006), also present on Chaplin et al. (2005a), where a multi-modal response was investigated in a long flexible cylinder with $m^* = 3$ and $L/D = 468$ under stepped current. Another close experiment is present in Huera-Huarte and Bearman (2009a) for a flexible cylinder with $m^* = 1.8$ and $L/D = 94$ for several top tensions.

The results for 2 degree-of-freedom rigid cylinders are from Jauvtis and Williamson (2004) for $m^* = 2.6$. The data from Fujarra et al. (2001) are from a cantilever cylinder only with transverse motion, for $m^* = 2.36$ and $L/D = 94$.

The cross-flow amplitudes of Huera-Huarte (2006) and the present work reached the upper branch. Results from Jauvtis and Williamson (2004), for $m^* = 2.6$ appears on the supper upper branch. Although the amplitudes from Fujarra et al. (2001) are closer to the supper upper branch, the authors understand as an extension of the initial branch. As reported in Huera-Huarte and Bearman (2009a), the response amplitudes is half of the values found in Jauvtis and Williamson (2004), for $m^* = 2.6$.

The authors suggest that the mass-damping and modal characteristics are important for the response of flexible structures, the latest controlled by the tension applied to the model. Further, if the tension is high and dominant, a multi-modal response such cables are predominant, otherwise a high aspect ratio cylinder behavior is established with amplitudes limited due to the restrains applied.

The response amplitudes found in this work is closer to the data found in Huera-Huarte (2006). Comparing the initial branch in both data, this work presents an amplitude jump to 0.65, while a smooth amplitude growth is found for Huera-Huarte (2006) data. The upper branch is very similar between them. The present work total amplitude does not show the desynchronization, however looking at the modal projection values the desynchronization region is identified and the amplitude response for the second lock-in are closer to Huera-Huarte (2006). Regarding the in-line motions, for the first lock-in region, the data values are also close.

Comparing the present result with Huera-Huarte and Bearman (2009a), the amplitudes found in this work are higher. The initial tension applied is similar ($60 - 72\ N$), however the present work is completely submerged and totally under the current profile, different from Huera-Huarte and Bearman (2009a) that is vertically mounted and partially submerged.

As an attempt to predict the VIV amplitudes responses as function of the mass-damping of the model, a compile data from Huera-Huarte and Bearman (2009a) is completed with the current work and data from Fujarra et al. (2001). This plot is known as the Griffin plot, Griffin, Skop and Ramberg (1975), and is shown in Figure 38, where Ca is 1 and ζ is the structural damping.

The results of this works are plotted considering the total amplitude of the first lock-in and the damping value of ζ_{s2}, the total amplitude of the second lock-in and the damping ζ_{s4}.

Figure 37 – Cross-flow amplitude (A_z^{max}/D) response and in-line amplitudes (A_x^{max}/D). ▼ — Fujarra et al. (2001), $m^* = 2.36$. ▲ — Jauvtis and Williamson (2004), $m^* = 2.6$. ◆ — Huera-Huarte and Bearman (2009a), $m^* = 1.8$. ● — Data from Huera-Huarte (2006) and Chaplin et al. (2005a), $m^* = 3$. ● — Present work total amplitude, $m^* = 3.9$.

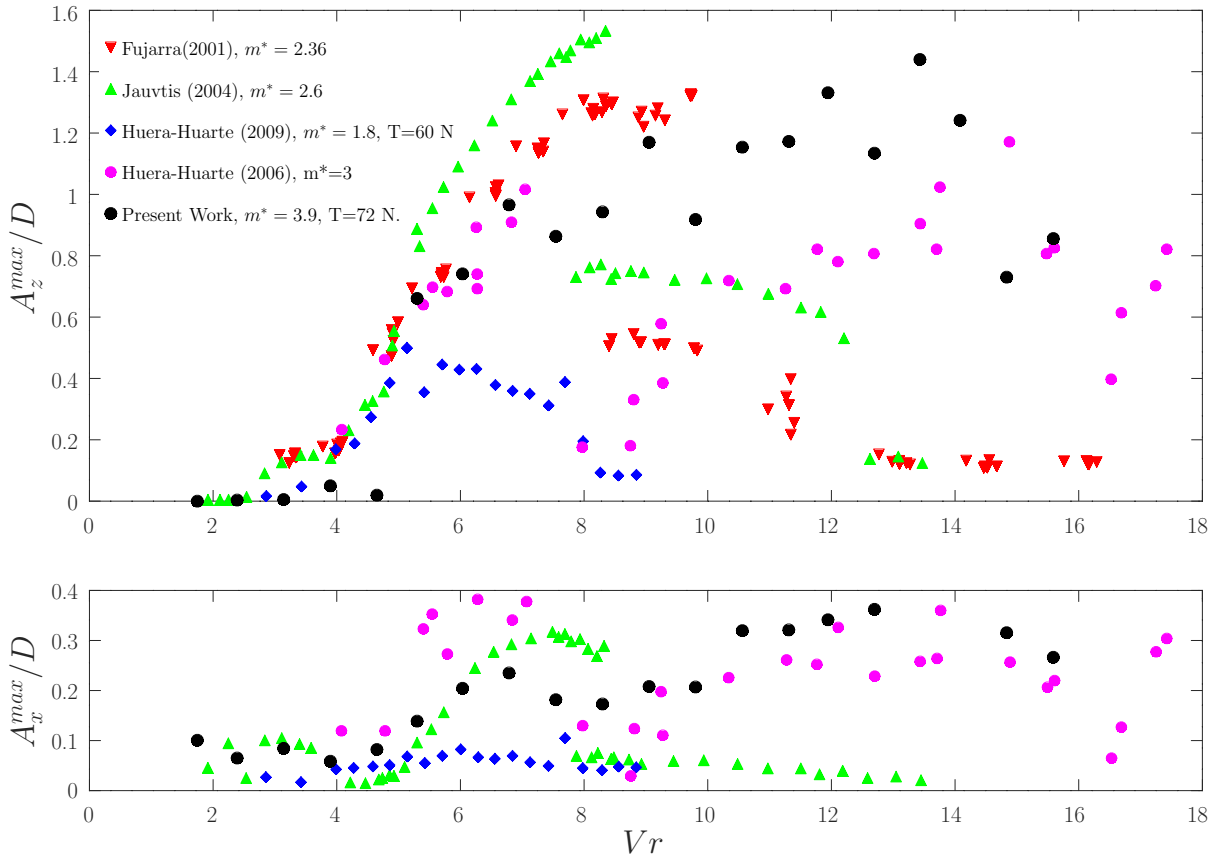

Source: The Author (2019).

Figure 38 – Cross-flow amplitude (A_z^{max}/D) as function of $\alpha = (m^* + Ca)\zeta$. ▲ — Jauvtis and Williamson (2004), $m^* = 2.54$. × — Govardhan and Williamson (2006). ⋆ — Hover, Techet and Triantafyllou (1998). □ — Owen, Bearman and Szewczyk (2001). ● — modes 1-8 from Huera-Huarte (2006). ◆ — Huera-Huarte and Bearman (2009a). ▼ — Fujarra et al. (2001). (●,■) — Present work first and second lock-in. —— Solid lines given by $(1 - 1.12\alpha + 0.3\alpha^2)log(0.41Re^{0.36})$ from Govardhan and Williamson (2006), Reynolds number steps of 4000.

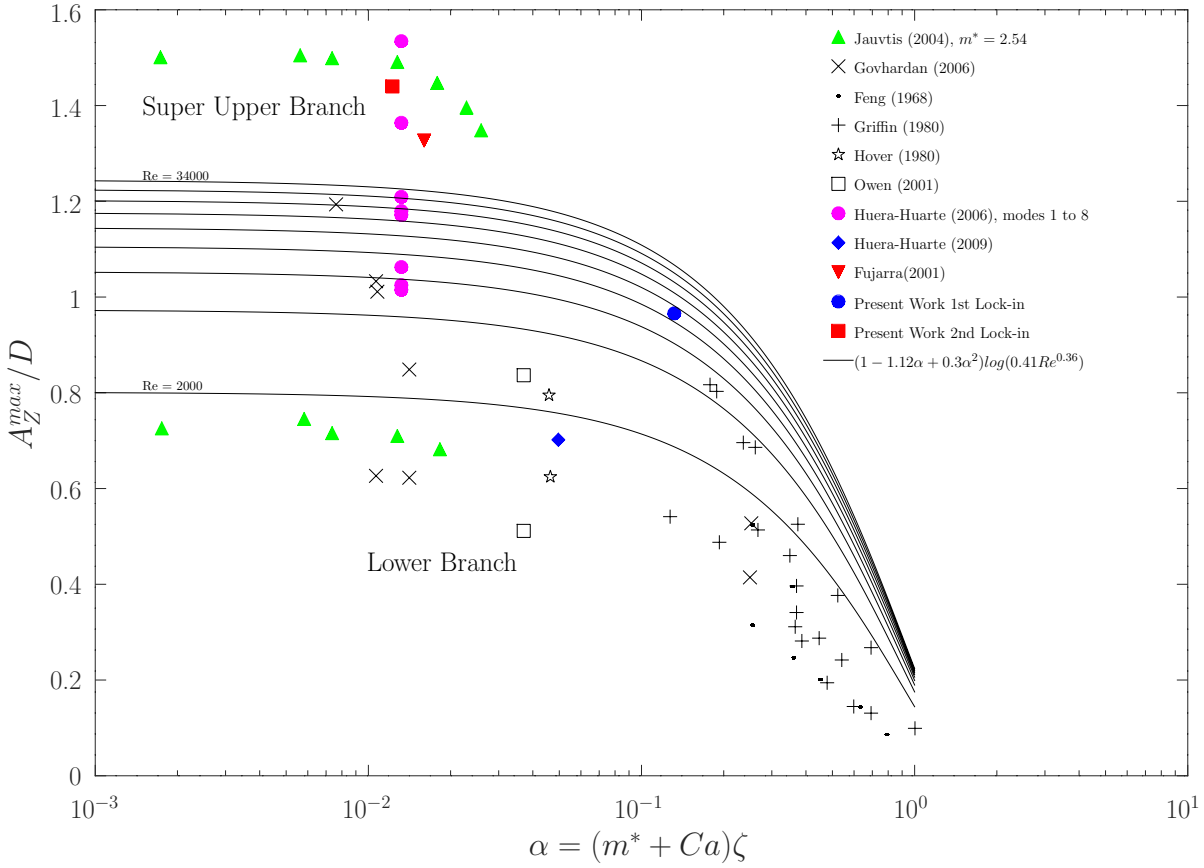

Source: The Author (2019).

5 CONCLUSION

This work has presented the dynamic response of vortex-induced vibrations on a long flexible cylinder fixed in both ends with ball joints. Analysis of the amplitude, frequency, and relative phase angle have been conducted.

First, the r.m.s. amplitudes up to 0.77 diameters for the cross-flow and 0.23 for in-line direction were observed, and the ratio between the cross-flow and in-line amplitudes are between 4 and 6. These values are lower than low mass rigid circular cylinders and agree with flexible structures reported in the literature, such as Huera-Huarte and Bearman (2009a) and Chaplin et al. (2005a). The overall response appears closer to tensioned structures or cables rather than rigid cylinder mounted in an elastic base because the successive synchronization of modes and the lack of VIV branches responses. Probably, the mass-damping factor and the tension applied to the model plays a role in the system making it closer to cables. The desynchronization was observed applying the modal projection analysis and the response proved to be multi-modal, where the total amplitude mostly had contributions of two or more modes, vibrating in the dominant mode. The latest also reported by Chaplin et al. (2005b), where the overall response is a combination of two or more modes.

Second, the frequency response based on Fourier analysis recovered the Strouhal number of 0.16 for the cross-flow motions and 0.32 for the in-line motions found by Huera-Huarte and Bearman (2009a). A more reliable frequency analysis was conducted using the Hilbert-Huang Transform, which showed a complex response near to the transition of modes, where a multi-modal response is present. When one mode is mainly present a narrow frequency band was found with the value close to the Fourier Transform analysis.

Third, the cross-flow motion profoundly influenced the in-line modes excited. It was observed that the successive mode excitation ($\mathcal{M}_1$, $\mathcal{M}_3$, $\mathcal{M}_5$ and so on) it was not respected. When a cross-flow mode is locked the next in-line mode is locked as well.

Fourth, the trajectories have shown coherence between in-line and cross-flow motions for most of the reduced velocities. The relative phase angle showed distinct values which impact the trajectory of the coupled motion. Some cases presented two angles varying in time, which appears on the peak of the transversal lock-in.

Finally, this work predict the maximum amplitude by the mass damping factor ($(m^* + C_a)\zeta$). The total overall amplitude of the two first lock-in were used along with the respective structural damping. The results have shown agreement with past results in

the literature.

The results presented in this paper presented different features between flexible structures with low mass ratio and rigid cylinders mounted in an elastic base. Many technique analysis were conducted in a single experiment making a unique database. These results may have a significant impact on the development of numerical codes for the prediction of VIV.

In order to conduct numerical analysis, deeper investigations about the material characterization should be conducted. Further studies increasing the tension and varying the mass would bring a better understanding of the phenomena, and the mechanics of the material with these variations should also be analyzed.

BIBLIOGRAPHY

BEARMAN, P. Circular cylinder wakes and vortex-induced vibrations. *Journal of Fluids and Structures*, v. 27, n. 5, p. 648 – 658, 2011. ISSN 0889-9746. IUTAM Symposium on Bluff Body Wakes and Vortex-Induced Vibrations (BBVIV-6). <http://www.sciencedirect.com/science/article/pii/S0889974611000600>.

BEARMAN, P. W. Vortex shedding from oscillating bluff bodies. *Annual Review of Fluid Mechanics*, v. 16, n. 1, p. 195–222, 1984. <https://doi.org/10.1146/annurev.fl.16.010184.001211>.

BEARMAN, P. W. Vortex shedding from oscillating bluff bodies. *Annual review of fluid mechanics*, Annual Reviews 4139 El Camino Way, PO Box 10139, Palo Alto, CA 94303-0139, USA, v. 16, n. 1, p. 195–222, 1984.

BLEVINS, R. D. Formulas for natural frequency and mode shape. RE Krieger, 1979.

BLEVINS, R. D. *Flow-induced vibration*. [S.l.]: New York, NY (USA); Van Nostrand Reinhold Co., Inc., 1990.

CHAPLIN, J.; BEARMAN, P.; CHENG, Y.; FONTAINE, E.; GRAHAM, J.; HERFJORD, K.; HUARTE, F. H.; ISHERWOOD, M.; LAMBRAKOS, K.; LARSEN, C.; MENEGHINI, J.; MOE, G.; PATTENDEN, R.; TRIANTAFYLLOU, M.; WILLDEN, R. Blind predictions of laboratory measurements of vortex-induced vibrations of a tension riser. *Journal of Fluids and Structures*, v. 21, n. 1, p. 25–40, nov. 2005. ISSN 0889-9746.

CHAPLIN, J.; BEARMAN, P.; HUARTE, F. H.; PATTENDEN, R. Laboratory measurements of vortex-induced vibrations of a vertical tension riser in a stepped current. *Journal of Fluids and Structures*, v. 21, n. 1, p. 3 – 24, 2005. ISSN 0889-9746. Fluid-Structure and Flow-Acoustic Interactions involving Bluff Bodies. <http://www.sciencedirect.com/science/article/pii/S0889974605001465>.

FRANZINI, G.; PESCE, C.; GONÇALVES, R.; FUJARRA, A.; MENDES, P. An experimental investigation on concomitant vortex-induced vibration and axial top-motion excitation with a long flexible cylinder in vertical configuration. *Ocean Engineering*, v. 156, p. 596 – 612, 2018. ISSN 0029-8018.

FRANZINI, G. R.; PESCE, C. P.; GONÇALVES, R. T.; FUJARRA, A. L. C.; MENDES, P. Experimental investigations on vortex-induced vibrations with a long flexible cylinder. Part I: modal-amplitude analysis with a vertical configuration. In: *Proceedings of the 11th International Conference on Flow-Induced Vibration - FIV2016*. [S.l.: s.n.], 2016.

FRANZINI, G. R.; PESCE, C. P.; GONÇALVES, R. T.; FUJARRA, A. L. C.; MENDES, P. Experimental investigations on vortex-induced vibrations with a long flexible cylinder. Part II: effect of axial motion excitation in a vertical configuration. In: *Proceedings of the 11th International Conference on Flow-Induced Vibration - FIV2016*. [S.l.: s.n.], 2016.

FRANZINI, G. R.; PESCE, C. P.; SALLES, R.; GONÇALVES, R. T.; FUJARRA, A. L. C.; MENDES, P. Experimental Analysis of a Vertical and Flexible Cylinder in Water: Response to Top Motion Excitation and Parametric Resonance. *Journal of Vibration and Acoustics*, v. 137, n. 3, p. 031010–031010–12, jun. 2015. ISSN 1048-9002. <http://dx.doi.org/10.1115/1.4029265>.

FUJARRA, A.; PESCE, C.; FLEMMING, F.; WILLIAMSON, C. Vortex-induced vibration of a flexible cantilever. *Journal of Fluids and Structures*, v. 15, n. 3, p. 651 – 658, 2001. ISSN 0889-9746. <http://www.sciencedirect.com/science/article/pii/S0889974600903682>.

GOVARDHAN, R.; WILLIAMSON, C. H. K. Resonance forever: existence of a critical mass and an infinite regime of resonance in vortex-induced vibration. *Journal of Fluid Mechanics*, Cambridge University Press, v. 473, p. 147–166, 2002.

GOVARDHAN, R. N.; WILLIAMSON, C. H. K. Defining the 'modified griffin plot' in vortex-induced vibration: revealing the effect of reynolds number using controlled damping. *Journal of Fluid Mechanics*, Cambridge University Press, v. 561, p. 147–180, 2006.

GRIFFIN, O. M.; SKOP, R. A.; RAMBERG, S. E. The resonant, vortex-excited vibrations of structures and cable systems. In: OFFSHORE TECHNOLOGY CONFERENCE. *Offshore Technology Conference*. [S.l.], 1975.

HOVER, F. S.; TECHET, A. H.; TRIANTAFYLLOU, M. S. Forces on oscillating uniform and tapered cylinders in cross flow. *Journal of Fluid Mechanics*, Cambridge University Press, v. 363, p. 97–114, 1998.

HUANG, N. E.; SHEN, Z.; LONG, S. R.; WU, M. C.; SHIH, H. H.; ZHENG, Q.; YEN, N.-C.; TUNG, C. C.; LIU, H. H. The empirical mode decomposition and the hilbert spectrum for nonlinear and non-stationary time series analysis. *Proceedings of the Royal Society of London. Series A: Mathematical, Physical and Engineering Sciences*, v. 454, n. 1971, p. 903–995, 1998. <https://royalsocietypublishing.org/doi/abs/10.1098/rspa.1998.0193>.

HUERA-HUARTE, F.; BEARMAN, P. Wake structures and vortex-induced vibrations of a long flexible cylinder-Part 1: Dynamic response. *Journal of Fluids and Structures*, v. 25, n. 6, p. 969–990, ago. 2009. ISSN 0889-9746.

HUERA-HUARTE, F.; BEARMAN, P. Wake structures and vortex-induced vibrations of a long flexible cylinder-part 2: Drag coefficients and vortex modes. *Journal of Fluids and Structures*, v. 25, n. 6, p. 991–1006, ago. 2009. ISSN 0889-9746.

HUERA-HUARTE, F. J. *Multi-mode vortex-induced vibrations of a flexible circular cylinder*. Tese (Doutorado) — University of London, 2006.

IWAN, W.; BLEVINS, R. A model for vortex induced oscillation of structures. *Journal of Applied Mechanics*, American Society of Mechanical Engineers, v. 41, n. 3, p. 581–586, 1974.

JAUVTIS, N.; WILLIAMSON, C. Vortex-induced vibration of a cylinder with two degrees of freedom. *Journal of Fluids and Structures*, v. 17, n. 7, p. 1035 – 1042, 2003. ISSN 0889-9746. <http://www.sciencedirect.com/science/article/pii/S0889974603000513>.

JAUVTIS, N.; WILLIAMSON, C. The effect of two degrees of freedom on vortex-induced vibration at low mass and damping. *Journal of Fluid Mechanics*, Cambridge University Press, v. 509, p. 23–62, 2004.

KHALAK, A.; WILLIAMSON, C. Motions, forces and mode transitions in vortex-induced vibrations at low mass-damping. *Journal of Fluids and Structures*, v. 13, n. 7, p. 813 – 851, 1999. ISSN 0889-9746. <http://www.sciencedirect.com/science/article/pii/S0889974699902360>.

LIE, H.; KAASEN, K. Modal analysis of measurements from a large-scale viv model test of a riser in linearly sheared flow. *Journal of Fluids and Structures*, v. 22, n. 4, p. 557 – 575, 2006. ISSN 0889-9746. <http://www.sciencedirect.com/science/article/pii/S0889974606000077>.

MALTA, E. B. *Investigação experimental das vibrações induzidas pela emissão de vórtices em catenárias sujeitas a perfis de correnteza variável, ortogonais ao plano de lançamento.* Tese (Doutorado) — Universidade de São Paulo, 2015.

MOROOKA, C. K.; TSUKADA, R. I. Experiments with a steel catenary riser model in a towing tank. *Applied Ocean Research*, v. 43, p. 244–255, out. 2013. ISSN 0141-1187.

NORBERG, C. Fluctuating lift on a circular cylinder: review and new measurements. *Journal of Fluids and Structures*, v. 17, n. 1, p. 57 – 96, 2003. ISSN 0889-9746. <http://www.sciencedirect.com/science/article/pii/S0889974602000993>.

OWEN, J.; BEARMAN, P.; SZEWCZYK, A. Passive control of viv with drag reduction. *Journal of Fluids and Structures*, v. 15, n. 3, p. 597 – 605, 2001. ISSN 0889-9746. <http://www.sciencedirect.com/science/article/pii/S088997460090358X>.

PEREIRA, F. R. *Investigação das vibrações induzidas pela emissão de vórtices em modelos reduzidos de riser lançados em catenária.* Tese (Doutorado) — Universidade de São Paulo, 2015.

PEREIRA, F. R.; FUJARRA, A. L. C.; PESCE, C. P.; GONÇALVES, R. T.; FRANZINI, G. R.; MENDES, P. Experimental investigations on vortex-induced vibrations with a long flexible cylinder. Part III: modal-amplitude analysis with a catenary configuration. In: *Proceedings of the 11th International Conference on Flow-Induced Vibration - FIV2016*. [S.l.: s.n.], 2016.

PEREIRA, F. R.; GONÇALVES, R. T.; PESCE, C. P.; FUJARRA, A. L. C.; FRANZINI, G. R.; MENDES, P. A Model Scale Experimental Investigation on Vortex-Self Induced Vibrations (VSIV) of Catenary Risers. In: ASME. *Proceedings of the 32nd International Conference on Ocean, Offshore and Arctic Engineering*. OMAE2013-10447, 2013. v. 7 - CFD and VIV, p. 9. <http://dx.doi.org/10.1115/OMAE2013-10447>.

PEREIRA, F. R.; GONÇALVES, R. T.; PESCE, C. P.; FUJARRA, A. L.; FRANZINI, G. R.; MENDES, P. A model scale experimental investigation on vortex-self induced vibrations (vsiv) of catenary risers. In: AMERICAN SOCIETY OF MECHANICAL ENGINEERS. *ASME 2013 32nd International Conference on Ocean, Offshore and Arctic Engineering*. [S.l.], 2013. p. V007T08A029–V007T08A029.

PIKOVSKY, A.; ROSENBLUM, M.; KURTHS, J. *Synchronization: a universal concept in nonlinear sciences*. [S.l.]: Cambridge university press, 2003.

RATEIRO, F.; GONÇALVES, R. T.; FUJARRA, A. L. C.; MENDES, P. Risers Model Tests: Scaling Methodology And Dynamic Similarity. In: . International Society of Offshore and Polar Engineers, 2012. <https://www.onepetro.org/conference-paper/ISOPE-I-12-307>.

SARPKAYA, T. A critical review of the intrinsic nature of vortex-induced vibrations. *Journal of Fluids and Structures*, v. 19, n. 4, p. 389 – 447, 2004. ISSN 0889-9746. <http://www.sciencedirect.com/science/article/pii/S0889974604000350>.

SKOP, R.; BALASUBRAMANIAN, S. A new twist on an old model for vortex-excited vibrations. *Journal of Fluids and Structures*, v. 11, n. 4, p. 395 – 412, 1997. ISSN 0889-9746. <http://www.sciencedirect.com/science/article/pii/S0889974697900852>.

SKOP, R.; GRIFFIN, O. A model for the vortex-excited resonant response of bluff cylinders. *Journal of Sound and Vibration*, v. 27, n. 2, p. 225 – 233, 1973. ISSN 0022-460X. <http://www.sciencedirect.com/science/article/pii/0022460X73900631>.

SKOP, R.; GRIFFIN, O. On a theory for the vortex-excited oscillations of flexible cylindrical structures. *Journal of Sound and Vibration*, v. 41, n. 3, p. 263 – 274, 1975. ISSN 0022-460X. <http://www.sciencedirect.com/science/article/pii/S0022460X75801738>.

SKOP, R. A.; GRIFFIN, O. M. et al. An heuristic model for determining flow-induced vibration of offshore structure. In: OFFSHORE TECHNOLOGY CONFERENCE. *Offshore Technology Conference*. [S.l.], 1973.

VANDIVER, J. Dimensionless parameters important to the prediction of vortex-induced vibration of long, flexible cylinders in ocean currents. *Journal of Fluids and Structures*, v. 7, n. 5, p. 423 – 455, 1993. ISSN 0889-9746. <http://www.sciencedirect.com/science/article/pii/S0889974683710285>.

VIEIRA, D. P. *Estudo Experimental das Vibrações Induzidas pela Emissão de Vórtices em Cilindros Flexíveis Inclinados em relação à Correnteza*. Tese (Doutorado) — Escola Politécnica da Universidade de São Paulo, 2017.

WILLIAMSON, C.; GOVARDHAN, R. Vortex-induced vibrations. *Annual Review of Fluid Mechanics*, v. 36, n. 1, p. 413–455, 2004. <https://doi.org/10.1146/annurev.fluid.36.050802.122128>.

APPENDIX A – DAMPING, FREQUENCY AND AXIAL STIFFNESS ESTIMATION

The methodology applied was composed by two main parts, the first concern to the decay tests in water and the second to the decay tests in air.

The decaying tests in water were conducted as follows. The model was placed under the water with a structure composed with a false bottom. One unidirectional load cell was attached in one end and accesses the axial force (tension force). An external stick was used to give an initial displacement at the middle of the model, then it is suddenly removed and the flexible cylinder vibrates. This process was repeated 4 consecutive times, each one is repeated after the oscillations were softened. A signal acquisition Lynx ADS 7000 system was used.

For the decay tests in air, the model was fixed on the same load cell used on the decay tests in water. The same tension was imposed to the model. The frequencies and damping were obtained using a load cell in one of the ends. Further, the experiment was repeated three times to assure the reliability of the tests. The experiments were carried for frequencies in-plane (Even vibration modes) and out-of-plane (Odd vibration modes), see Figure 14.

Firstly, Table 7 shows the frequencies found using a fast Fourier transform of the load cell register. An example of the Fourier spectrum is shown in Figure 39.

Figure 39 – Example of the Fourier Transform Spectrum for the decaying test in water.

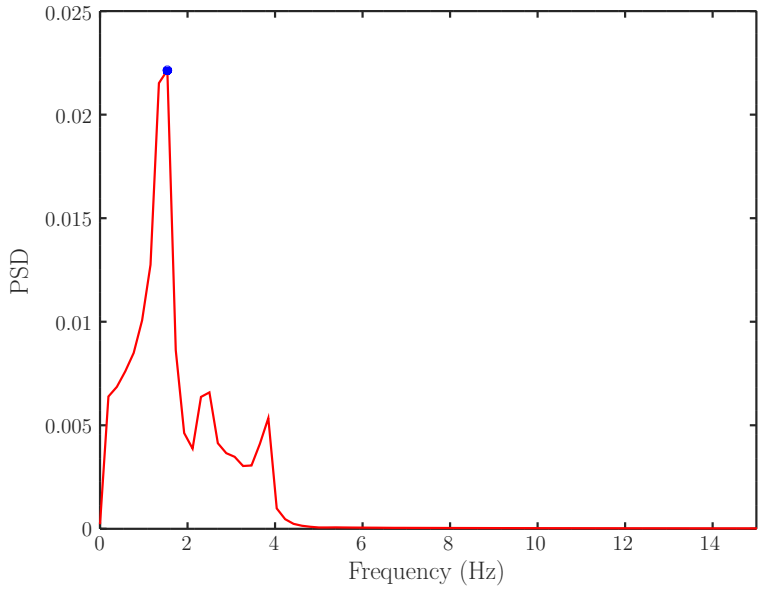

Source: The Author (2019).

Table 7 – Frequency of the vibration modes obtained through the decaying tests in water.

Mode $\mathcal{M}_i$	Test 1 (Hz)	Test 2 (Hz)	Test 3 (Hz)	Mean Value (Hz)
$\mathcal{M}_1$	1.50	1.28	1.38	1.39
$\mathcal{M}_2$	1.41	1.30	1.42	1.38
$\mathcal{M}_3$	2.46	2.56	2.56	2.53
$\mathcal{M}_4$	2.47	2.42	2.43	2.44
$\mathcal{M}_5$	3.83	3.85	3.76	3.81
$\mathcal{M}_6$	3.89	3.91	3.90	3.89

Source: The Author (2019).

Therefore, the value of the frequency of $\mathcal{M}_2$ was found $f_{n2} = 1.38Hz$. Furthermore, Figure 40 shows the fit using the equation $F = e^{-\zeta\omega_n t}$ of the load cell peaks. This resulted in a damping of $\zeta_{2t} = 9.65\%$

Moreover, the results for the decaying tests in air is shown in Table 8. It is important to remember that these values represents the modal structural damping and the frequency in air.

Furthermore, the theory of cables presented in Section 2.3 was used to find the axial stiffness. Using the Equation (2.12) for the frequency of $\mathcal{M}_2$ in air, the value of λ_2 was found. With this parameter, the value of α_2 is found using Equation (2.13). And, finally, the value of the axial stiffness was found using the relation Equation (A.1), where $L_e(m)$ is the deformed length, $L(m)$ the length, $T_0(N)$ the initial axial force and

Figure 40 – Exponential fit: water decaying test.

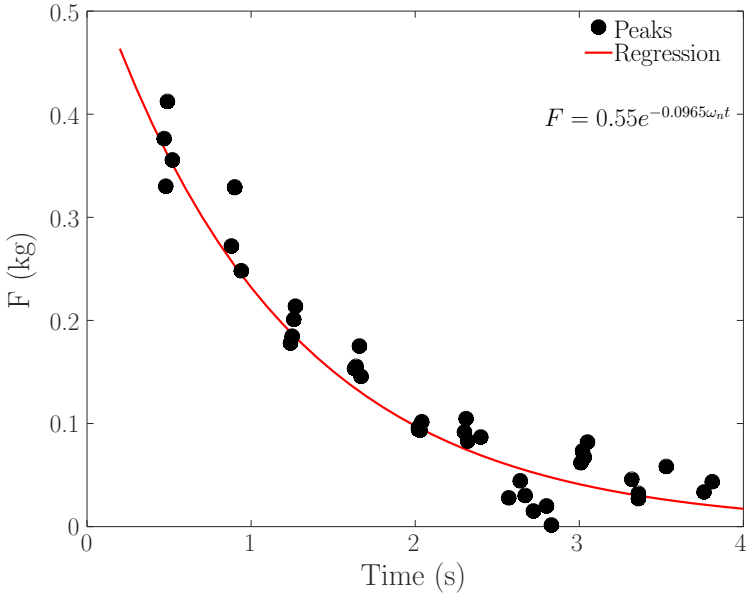

Source: The Author (2019).

Table 8 – Frequency and damping of the vibration modes obtained through the decaying tests in air.

Mode $\mathcal{M}_i$	Test 1 (Hz)	Test 2 (Hz)	Test 3 (Hz)	Mean Value (Hz)	Damping $\zeta_s(\%)$
$\mathcal{M}_1$	1.34	1.35	1.35	1.34	0.30
$\mathcal{M}_2$	1.51	1.51	1.53	1.52	2.69
$\mathcal{M}_3$	2.68	2.70	2.68	2.69	0.20
$\mathcal{M}_4$	2.64	2.65	2.63	2.64	0.25
$\mathcal{M}_5$	4.03	4.03	4.02	4.03	-
$\mathcal{M}_6$	4.03	4.04	4.03	4.03	-

Source: The Author (2019).

$d = 0.165(m)$ the sag. For more information about the cable theory, read Section 2.3 and Blevins (1979).

$$\alpha^2 = \left(\frac{8d}{L}\right)^2 \frac{EA}{T_0}\frac{L}{L_e} \tag{A.1}$$

The value found was $EA = 1.3kN$, which is within the range $1 < EA < 1.6kN$ found for a similar model reported in Franzini et al. (2015).